DENSITY WAVES AND FLUCTUATIONS IN THREE-DIMENSIONAL GRANULAR POISEUILLE FLOW

A Thesis

Submitted for the Degree of

Master of Science (Engineering)

by

Ashish Malik

Engineering Mechanics Unit
Jawaharlal Nehru Centre for Advanced Scientific Research
(A Deemed University)
Bangalore – 560 064

AUGUST 2008

To God

DECLARATION

I hereby declare that the matter embodied in the thesis entitled "**Density Waves and Fluctuations in Three-dimensional Granular Poiseuille Flow**" is the result of investigations carried out by me at the Engineering Mechanics Unit, Jawaharlal Nehru Centre for Advanced Scientific Research, Bangalore, India under the supervision of **Prof. Meheboob Alam** and that it has not been submitted elsewhere for the award of any degree or diploma.

In keeping with the general practice in reporting scientific observations, due acknowledgment has been made whenever the work described is based on the findings of other investigators.

Ashish Malik

CERTIFICATE

I hereby certify that the matter embodied in this thesis entitled "**Density Waves and Fluctuations in Three-dimensional Granular Poiseuille Flow**" has been carried out by Mr. **Ashish Malik** at the Engineering Mechanics Unit, Jawaharlal Nehru Centre for Advanced Scientific Research, Bangalore, India under my supervision and that it has not been submitted elsewhere for the award of any degree or diploma.

Prof. Meheboob Alam
(Research Supervisor)

Acknowledgments

I am very indebted to Prof. Meheboob Alam for his guidance and help throughout. I am very thankful to him for his patience, especially at times I was unsuccessful in my work. I learned how to work under pressure because of him.

I am very thankful to Max-Planck Partner Group (MPI-MM Bremen) for the financial support from 01.10.2007 upto 30.04.2008 under the debit head MPI/MA/4190. I am also thankful to DRDO for further financial support from 01.05.2008 upto 31.08.2008 under the debit head DRDO/RN/4124.

I am very fortunate to be a part of the JNC community during my stay here. I have spent very nice and unforgettable moments of my academic life here at JNC. I really had a good time as a Student Representative and also as a member of the Movie Club. I'm grateful to everybody here for their support and friendship, be it clarifying doubts in Fortran, Latex, graphics card computation or movie downloading ! I had fun and adventurous moments with Harish and Anubhab during the *treks* and will always be thankful to them.

Abstract

In the present thesis, the gravity driven granular Poiseuille flow has been probed via event-driven simulations in three dimensions between two infinite parallel plates. A monodisperse system of "rough" inelastic hard spheres interacting via hard core potential has been used. The normal coefficient of restitution (e) and the tangential coefficient of restitution (β) are the two basic governing parameters of the collision process. The influence of particle volume fraction (ϕ), particle roughness (β) and inelasticity (e) on various micro-structural features (velocity distribution functions, correlations, etc.) and macro-structural features (density waves, velocity, density and temperature profiles, etc.) has been probed in the rapid flow regime.

The Boltzmann limit ($\phi = 0.01$) of the granular Poiseuille flow has been investigated in detail. By probing the local velocity distribution functions (VDFs) for a range of e and β, it is found that the particle roughness plays an important role in the deviation of VDFs from the Gaussian distribution. The translational and rotational VDFs can differ significantly from each other depending on the values of e and β. The density correlation was found to be negligible for any values of β and e in the Boltzmann limit; however, significant "directional" correlations between translational and rotational velocities were observed for all values of β. For a moderately dense flow ($\phi = 0.1$), we observed the formation of dense *plugs* and density waves. As in the case of Boltzmann limit, the VDFs are found to be significantly affected by the particle roughness as well as by inelastic dissipation. The pair correlation function shows that the system has a liquid-like structure around the channel centerline where the particles are flowing in the form of density waves. It is found that there are strong directional correlations over the whole channel width which increases with increasing dissipation. For any value of β, the spatial velocity correlations are found to be the largest for the streamwise velocity. A limited set of results on VDFs and correlations for a very dense flow ($\phi = 0.5$) has been qualitatively compared with recent experiments in a similar setup. The

present work indicates that orientational correlations should be incorporated in the theoretical models of granular flows.

The formation of density waves has been examined for a single density ($\phi = 0.15$), and different steady state forms of density variations have been observed. The nature of such density waves has been analysed using the Fourier analysis of the coarse-grained density field. It is found that the density-waves and structure formations can be controlled by varying the system size. The density-wave appears to persist in larger computational domains, and increasing the channel dimensions simply permit additional wave numbers to be realized. At small values of the channel width W/d and the aspect-ratio L/W, the system develops a *plug flow*. The system develops an *S-shaped wavy flow* at intermediate values of W/d and further there is a formation of slugs and a combination of these structures. With decreasing dissipation, the steady wave structure no longer persists but results in the formation of slugs if L/W is large enough. The effect of three dimensionality has been studied and it is found that the availability of the third dimension significantly influences the formation of the density waves. The particle motion in the observed three-dimensional structures indicates the presence of vorticity, an important consideration for granular flows, which would enhance mixing of granular materials.

List of Figures

Contents

CHAPTER 1

INTRODUCTION

1.1 What is Granular Matter ?

Granular materials are basically a collection of large number of solid particles of same or varying sizes and shapes. They are ubiquitous in nature and present an indispensable part of the real world. We see granular particles of all sizes and shapes ranging from powders, cement, sand, soil, food grains, fertilizers, capsules and pills, gravel, to large chunks of coal and other minerals, pebble-bed nuclear reactor, etc., see Fig. 1.1. The transport of bulk solid materials is an integral part of many industrial processes; granular flows are also of importance in geophysical events such as snow avalanches, rock and land slides, and planetry rings. Hence a better understanding of the basic flow mechanisms is of critical importance to a wide variety of industrial, geophysical and scientific applications (Campbell (1990); Savage (1982); Goldhirsch (2003); Haff (1983); Jenkins & Richman (1985); Kadanoff (1999); Herrmann *et al.* (1998); Jaeger *et al.* (1996); Bagnold (1954); Choi *et al.* (2004); Ottino & Khakhar (2000); Alam & Luding (2003)).

Granular flows are characterised into two regimes depending on the particle-particle interaction: *slow flow regime* and *rapid flow regime*. Slow flows (Savage (1982)) have enduring contact between the particles with sliding and rolling motion dominating the interactions. In such cases the densities are generally high and the deformation rates are low; the momentum and energy transfers between the particles take place through frictional forces (and hence commonly known as frictional flows). On the other hand, rapid flows (Campbell (1990); Goldhirsch (2003)) have high deformation rates and are reminiscent of molecular gases. In rapid flow regime, the particles generally move around randomly interacting via instantaneous dissipative collisions with negligible interstitial fluid effects (dry granular medium). The momentum and energy transfer between the particles occur through instantaneous binary collisions. These similarities with the thermal motion of molecules have motivated in defining the "granular" temperature as the mean kinetic energy as-

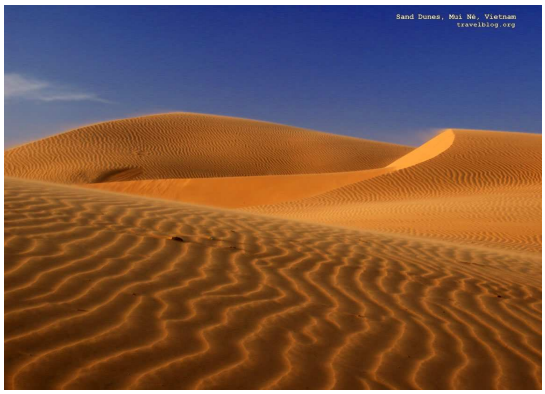

(a) Sand dunes

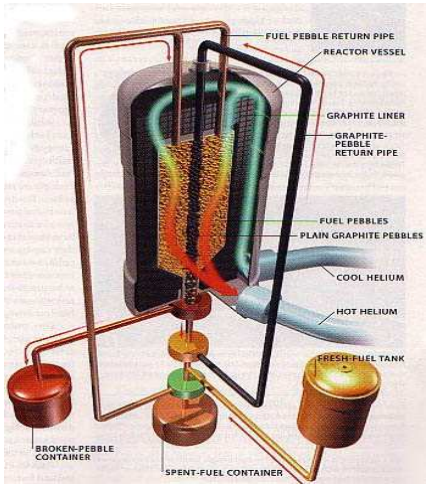

(b) Pebble-bed nuclear reactor

(c) Cement and gravels

(d) Corn pile

Figure 1.1: Different types of granular materials

sociated with the fluctuation motion (Campbell (1990); Goldhirsch (2003); Jaeger *et al.* (1996)). However this temperature is *not* the thermodynamic temperature.

In contrast to the molecular gas, granular particles are macroscopic in nature and their collisions are "inelastic". The inelastic collisions lead to dissipation of energy, and hence to sustain a steady motion the system continuously needs energy input. Thus granular flows are inherently in *out-of-equilibrium*. The energy needed to lift a particle is large compared to the energy it receives from the thermal environment, i.e., $k_B T$, where k_B is the Boltzmann constant and T is the thermodynamic temperature (Jaeger *et al.* (1996)). Consequently, they cannot spontaneously rearrange in phase space and hence they need external forces like shearing by plates, vibrating bed, gravity, etc., to stay in fluidized state. There are

difficulties in describing granular media using standard hydrodynamic equations since often there is no lack of scale separation between microscopic and macroscopic scales whereas hydrodynamic equations assume scale-separation. The scale separation assumption means the existence of well defined length and time scales, much larger than microsocopic scales and smaller than macroscopic scales, over which averaging is performed.

In the past two decades, due to the contributions from a number of experimental investigations, theoretical analyses and numerical simulations, our fundamental understanding of the governing mechanisms for the rapid flow of granular materials has been steadily increasing but still it is far from complete. The flowing granular material exhibits many complexities including heap formation, convection under vibration, formation of density waves and their efects on the flow, jamming and other rheological phenomena. Segregation (Ottino & Khakhar (2000); Alam *et al.* (2006)) occurs when particles of different sizes are mixed (especialy in pharmaceutical industry) which prevents uniform mixing, Fig. 1.2(a). Jamming is very commonly observed in feeders and hoppers leading to clogging, Fig. 1.2(b). Clogging is encountered while transporting granular materials on conveyor belts, Fig. 1.2(c).

1.2 Granular Poiseuille Flow and Present work

Experimental studies on granular flows have provided valuable information on stresses at relatively high solid concentrations and shear rates. Nevertheless, there remain several limitations that are difficult to overcome. One would like to develop instrumentation that is capable of measuring flow properties such as velocity, slip velocities at wall, density and granular temperature profiles inside the granular material without disturbing the flow field. In the context of gravity-driven granular Poiseuille flow, some experimental efforts in this direction have been made in the works of Orpe & Kudrolli (2007) and Moka & Nott (2005). There have been many experimental and simulation works on gravity-driven flow of granular materials through a hopper (Natarajan *et al.* (1995); Liss *et al.* (2002); Baran *et al.* (2006); Denniston & Li (1999); Tsai *et al.* (2001); Mohan *et al.* (2002); Vijaykumar (2007); Ferguson & Chakraborty (2006)) which is an analog of granular Poiseuille flow.

Following the approaches of molecular dynamics (MD) simulation, the computer

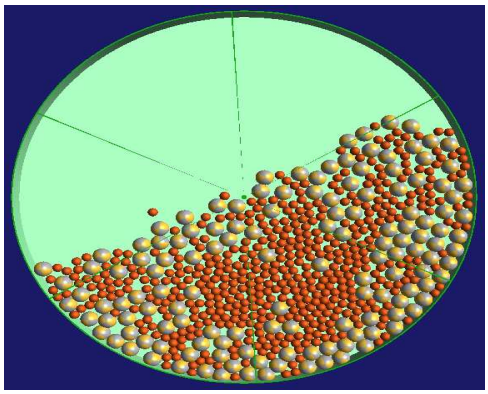

(a) Segregation

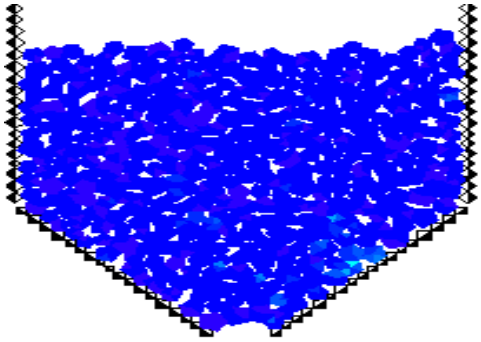

(b) Jamming and arch formation

(c) Clustering on Conveyor belt

Figure 1.2: Some undesirable phenomena occuring in granular flows

simulations of rapid granular flows have become excellent tools to provide detailed information about basic flow mechanics over the whole range of densities, which otherwise might be difficult to obtain in physical experiments (Campbell (1990); Goldhirsch (2003)).

In the present work, various micro-structural features (velocity distribution functions, correlations, etc.) and macro-structural features (density waves, velocity, density and temperature profiles, etc.) of a gravity driven granular Poiseuille flow are probed in the rapid flow regime using event-driven simulation in three-dimensions (3D). A monodisperse system of "rough" inelastic hard spheres interacting via hard core potential is considered. The collisions are assumed to be binary and instantaneous in which only momentum is conserved but the energy is a non-conserved quantity. The recent simulation work of Vijaykumar (2007) on the same topic using "smooth" particles in two-dimensions (2D) is a precursor of the present

work. For rough particles, one needs to take into account the rotational degrees of freedom (Lun (1991); Mitarai *et al.* (2002); Goldhirsch *et al.* (2005); Gayen & Alam (2006)), leading to a "micropolar" description of the continuum (Eringen (1964)). The validity of a possible micropolar description of granular media neeeds a systematic investigation. The present work is directed to gain knowledge about micropolar granular fluids.

1.3 Organisation of the thesis

Chapter 2

This chapter gives a description about different types of interaction potentials and the collision dynamics of the particle-particle as well as particle-wall interactions. Then comes the details about the event-driven algorithm used in the simulation and the code development. The details about the method of averaging and the code-validation form the last part of this chapter.

Chapter 3

This chapter discusses the results in the Boltzmann limit of the granular Poiseuille flow. All results are for simulations of a dilute system using the particle volume fraction $\phi = 0.01$ over a range of normal and tangential restitution coefficients. Discussion consists of *macro-structural* features of the gravity driven granular Poiseuille flow such as linear and angular velocity profiles, rotational and translational granular temperatures, density, etc., along with the slip velocities and gradients of the velocities and temperatures at the wall. The *micro-structural* quantities like velocity distribution functions, velocity correlations, pair correlation and orientational correlations form the second half of this chapter. In the context of granular Poiseuille flow, the present results on "orientational" correlations are entirely new, along with the evidence of micropolar effects.

Chapter 4

This chapter starts with the results for moderately dense flows having a particle volume fraction of $\phi = 0.1$. All macro- and micro-structural features of the flow are discussed for this case. After a brief discussion about the density clusters observed we move on to dense flows with $\phi = 0.5$ and the results for all the above mentioned quantities form the remaining chapter. For this dense flow, we make a qualitative comparison of our results with recent experimental results of Orpe & Kudrolli (2007).

Chapter 5

In this chapter the granular flow is moderately dense with a particle volume fraction of $\phi = 0.15$. Large scale structures and different forms of density waves are identified and a phase diagram of their steady state structures is presented in the (L/W, W/d) plane. The effect of various parameters on the formation of such density waves and the Fourier analysis of the density field to examine the time evolution of density waves are discussed. The present results on 3D density-waves are new. All previous simulations (Liss *et al.* (2002); Vijaykumar (2007)) focussed on density waves in 2D granular Poiseuille flow.

CHAPTER 2

SIMULATION METHOD

This chapter gives a detailed description of the collision model and the method of simulation used in the present work. It also gives a brief overview of various types of interaction potentials.

2.1 Interaction potentials

The most elementary microscopic model for a substance capable of existing in any of three most familiar states of matter- solid, liquid and gas - is based on *spherical particles* that interact with one another. The interactions, at the simplest level, occur between pairs of atoms and are responsible for providing two principal features of an interatomic force. The first is a resistance to compression, hence the interaction repels at a close range. The second is to bind the atoms together in the solid and liquid states and for this the atoms must attract each other over a range of seperations. Potential functions exhibiting these charactersitics can adopt a variety of forms and actually provide useful models for real substances.

The simpler, more idealized, pair potentials commonly used in simulations reflect the salient features of real interactions in an empirical way. Different types of potentials (Allen & Tildesley (1987)) are shown in Fig. 2.1 that are discussed next.

2.1.1 Lennard-Jones potential

The best known of these potentials, originally proposed for liquid argon, is the Lennard-Jones (LJ) potential, Fig. 2.1(a). For a pair of atoms i and j, located at r_i and r_j, the potential energy is given as:

$$v^{LJ}(r_{ij}) = \begin{cases} 4\epsilon\left[\left(\frac{\sigma}{r_{ij}}\right)^{12} - \left(\frac{\sigma}{r_{ij}}\right)^{6}\right] & r_{ij} < r_c \\ 0 & r_{ij} \geq r_c \end{cases} \tag{2.1}$$

where $\mathbf{r}_{ij} = \mathbf{r}_i - \mathbf{r}_j$ and $r_{ij} \equiv |\mathbf{r}_{ij}|$. The parameter ϵ governs the strength of the interaction and σ defines the length scale. The parameter r_c is termed as the cut-off distance at which the Lennard-Jones potential is often truncated to save the computational time; generally $r_c = 2.5\sigma$ is used in molecular dynamics simulations. This potential shows some typical features of interatomic interactions. There is an attractive tail at large seperations; there is a negative well, responsible for cohesion in condensed phases; finally, there is a steeply rising repulsive wall at short distances.

2.1.2 Hard-sphere potential

For the purpose of investigating general properties of liquids and for comparison with theory, highly idealized pair potentials are used for the sake of convenience in simulation. The hard-sphere potentials has the form:

$$v^{HS}(r_{ij}) = \begin{cases} \infty & r_{ij} < d \\ 0 & r_{ij} \geq d \end{cases} \tag{2.2}$$

where d is the diameter of the hard sphere. This potential has no attractive part, but does simulate the steep repulsive part of realistic potentials. This simplest potential is often used to simulate hard-sphere gas or fluid. As shown in Fig. 2.1(b) the interaction potential between hard spheres is a discontinious function of r. The repulsive force (impulse) comes into picture at the moment of the collision of spheres at the contact point. In the absence of any external force, the particles move in straight lines at a constant speed untill a collision and change their velocities immediately when a collision occurs.

The *hard-sphere potential* is used in the present simulation work where granular particles are modelled as rough inelastic hard spheres which is discussed in section 2.2.

2.1.3 Square-well potential

The square-well potential, Fig. 2.1(c), is identical to the hard-sphere potential with the addition of an attractive well of depth $-\epsilon$. Mathematically it is expressed as:

$$v^{SW}(r_{ij}) = \begin{cases} \infty & r_{ij} < d \\ -\epsilon & d < r < d_c \\ 0 & r_{ij} \geq d_c \end{cases} \tag{2.3}$$

The square-well potential is often thought of as a coarse-grained treatment of the Lennard-Jones potential because it also takes into account both excluded volume interaction and attractive interactions. Similar to the hard-sphere potential, potentials such as this can be used in event-based, collision dynamics methods (Rapaport 1995).

2.1.4 Soft-sphere potential

The soft-sphere potential, Fig. 2.1(d), is represented as:

$$v^{SS}(r_{ij}) = \epsilon\Big(\frac{d}{r_{ij}}\Big)^{\nu} \tag{2.4}$$

where ν is a repulsion parameter, often chosen to be an integer. The soft-sphere potential becomes progressively *harder* as ν is increased. Soft-sphere potentials do not contain any attractive part.

2.2 Collision Model of Rough Particles

For the characterization of a system with many particles we specify only *two-particle interactions*, assuming many-body interactions to result from the sum of two-particle forces. First we assume only two particles collide at a given time and neglect other particles and external forces. The collision at a given time is not necessarily of interest and may be assumed to be instantaneous. These assumptions require the specification of a collision matrix that connects the velocities before and after the collision, and are used for event-driven (ED) simulation method.

We consider a monodisperse system of rough, inelastic hard spheres of size d,

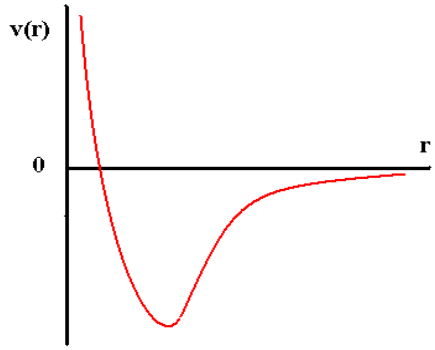

(a) Lennard-Jones potential

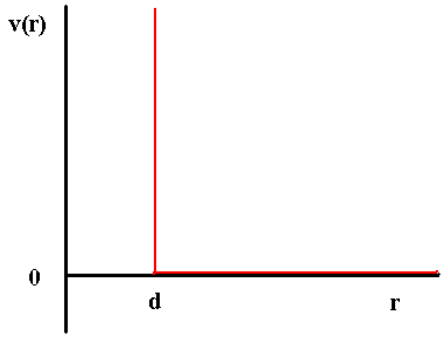

(b) Hard-sphere potential

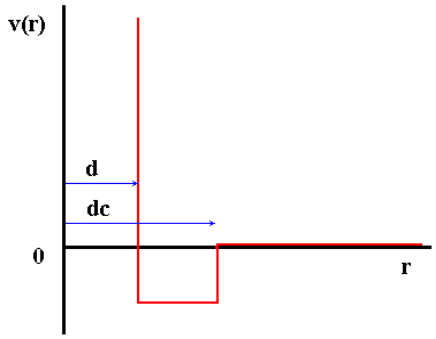

(c) Square-well potential

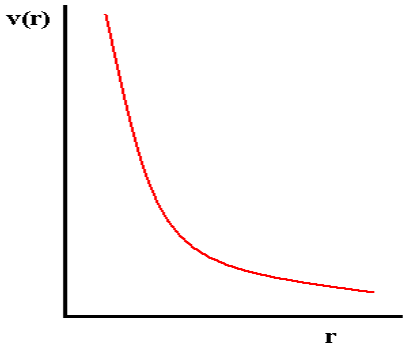

(d) Soft-sphere potential ($\nu = 1$)

Figure 2.1: Idealized pair potentials

mass m, and the moment of inertia I, interacting via hard-sphere potential. The *pre-collisional* translational and angular velocities of particle i are denoted by $\mathbf{c}_i$ and ω_i respectively, the corresponding *post-collisional* velocities are denoted by the primed symbols,$\mathbf{c}_i'$ and ω_i'. Let $\mathbf{k}_{ij} = \mathbf{z}_j - \mathbf{z}_i = \mathbf{k}$ be the unit vector directed from the center of the i-th particle to that of j-th particle. The total pre-collisional relative velocity at contact, $\mathbf{g_{ij}}$, between particle i and j is given by

$$\mathbf{g}_{ij} = \mathbf{c}_{ij} - \frac{1}{2} d\mathbf{k} \times (\omega_i + \omega_j), \tag{2.5}$$

where $\mathbf{c}_{ij} = \mathbf{c}_i - \mathbf{c}_j$ is the translational velocity of particle i relative to j,

2.2.1 Particle-particle collision

The collisions between granular particles are inherently "inelastic", hence a fraction of kinetic energy is lost in the form of heat. Thus there is only momentum conservation in this process and the velocity of the center of mass of the particles is not modified. For the simplest model of rough, inelastic spheres, two material

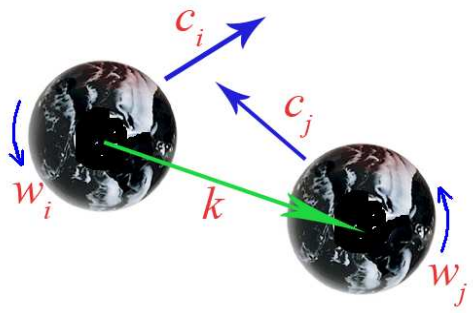

Figure 2.2: Particle-particle collision

parameters are needed to characterize the collision process: the normal coefficient of restitution, e, and the tangential coefficient of restitution, β. The former is an indicator of the inelasticity of a particle and the latter an indicator of its surface roughness. The pre- and post-collisional velocities of the colliding particles are related via the following expressions (Lun & Savage (1987); Lun (1991); Luding *et al.* (1998)):

$$\mathbf{k}\cdot\mathbf{g}'_{ij} = -e(\mathbf{k}\cdot\mathbf{g}_{ij}), \tag{2.6}$$

$$\mathbf{k}\times\mathbf{g}'_{ij} = -\beta(\mathbf{k}\times\mathbf{g}_{ij}) \tag{2.7}$$

In general, $0 \leq e \leq 1$ and $-1 \leq \beta \leq 1$. The case of $\beta = -1$ indicates collision between perfectly smooth particles, with increasing value of β being an indicator of the increasing degrees of particle surface friction. $\beta = 0$ represent the case for which the particle surface friction and inelasticity are sufficient to eliminate the post-collisional tangential relative velocities. For $0 < \beta \leq 1$, the *spin-reversal* occurs after a collision, and the case of $\beta = 1$ corresponds to the collision between perfectly rough particles so that there is complete reversal of spin. The onset of spin-reversal occurs at $\beta = 0$.

From the conservation laws of linear and angular momentum, the pre- and post-collisional velocities are related as

$$m\left(\mathbf{c}_i - \mathbf{c}_i'\right) = m\left(\mathbf{c}_j' - \mathbf{c}_j\right) = \mathbf{J}, \tag{2.8}$$

$$I\left(\omega_i' - \omega_i\right) = I\left(\omega_j' - \omega_j\right) = -\frac{1}{2}d\left(\mathbf{k}\times\mathbf{J}\right), \tag{2.9}$$

with $i \neq j$ and the collisional impulse is given by

$$\mathbf{J} = m\eta_2\mathbf{g}_{ij} + m\left(\eta_1 - \eta_2\right)\mathbf{k}\left(\mathbf{k}\cdot\mathbf{g}_{ij}\right) \tag{2.10}$$

with

$$\eta_1 = \frac{1}{2}(1+e),\ \ \eta_2 = \frac{1}{2}(1+\beta)K/(1+K),\ \ K = 4I/(md^2) \tag{2.11}$$

Here K is the nondimensional moment of inertia of a particle: $K = 2/5$ for solid spheres, $2/3$ for a thin-shell sphere (i.e. the mass is uniformly distributed over its surface), and 0 when the mass is concentrated at the center of the sphere (i.e. for point particles).

2.2.2 Wall-particle collision

The collision of a particle with a wall is assumed like a collision with a rough surface of infinite mass. The second particle j being wall in this case, there is no j subscript in the variables in the following expressions. As the walls are rough, particle's tangential as well as rotational velocity change after the collision. We use e_w and β_w to denote normal and tangential restitution coefficients, respectively, for particle-wall interactions. The collision rule for this model is

$$\mathbf{n_y}\cdot\mathbf{g}_i^{w\prime} = -e_w(\mathbf{n_y}\cdot\mathbf{g}_i^{w}) \tag{2.12}$$

$$\mathbf{n_y}\times\mathbf{g}_i^{w\prime} = -\beta_w(\mathbf{n_y}\times\mathbf{g}_i^{w}) \tag{2.13}$$

Here the unit vector can easily be found from Fig. 2.3 as $\mathbf{n_y}$ and $-\mathbf{n_y}$ when the particle interaction is with the upper and lower walls, respectively; $\mathbf{g_i^w}$ and $\mathbf{g_i'^w}$ are, respectively, the pre-collisional and post-collisional relative velocity at wall-particle

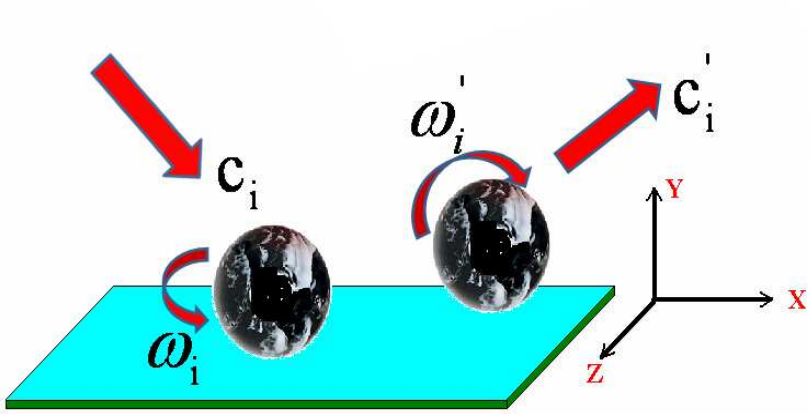

Figure 2.3: Particle-wall collision for ith particle

contact. Similarly, we can obtain an expression for wall-particle impulse:

$$m\left(\mathbf{c}_i - \mathbf{c}_i'\right) = \mathbf{J_w},\;\; I\left(\omega_i' - \omega_i\right) = -\frac{1}{2}\sigma\left(\mathbf{n}_y \times \mathbf{J_w}\right), \tag{2.14}$$

and

$$\mathbf{J_w} = 2m\eta_2^w \mathbf{g}_i^w + 2m\left(\eta_1^w - \eta_2^w\right)\mathbf{k}\left(\mathbf{k}\cdot\mathbf{g}_i^w\right), \tag{2.15}$$

where $\mathbf{J_w}$ is the impulse for wall-particle collision and

$$\eta_1^w = \frac{1}{2}(1+e_w),\;\; \eta_2^w = \frac{1}{2}(1+\beta_w)K/(1+K). \tag{2.16}$$

2.3 Simulation algorithm

A naive serial algorithm (Allen & Tildesley (1987)) advances the state of all particles from one collision to another. The state of all N particles are examined and updated at times $t_0 \leq t_1 \leq t_2 \leq ...$, where t_0 is the initialization time and t_{i+1} is the nearest next collision time seen at time t_i. This naive scheme is inefficient and expensive for large N due to following reasons:
(a) The same collision is repeatedly scheduled an order of N times until it occurs.
(b) In a typical cycle, most particles are not participating in collisions; still, they are examined by the algorithm.
(c) It is an expensive method for determining the nearest collision for a chosen particle. A straight-forward method is to compare the chosen particle with (N-1)

other particles.

The present simulation of hard spheres is based on billiards particle algorithm, an Event-Driven algorithm, of Lubachevsky (1991) and Rapaport (1995). The computational work involves initialization, book-keeping and diagnostic parts. Here an improvement from the above mentioned "naive serial algorithm" is achieved by dividing simulation domain into cells of $O(N)$ as shown in Fig. 2.4. Only the particles

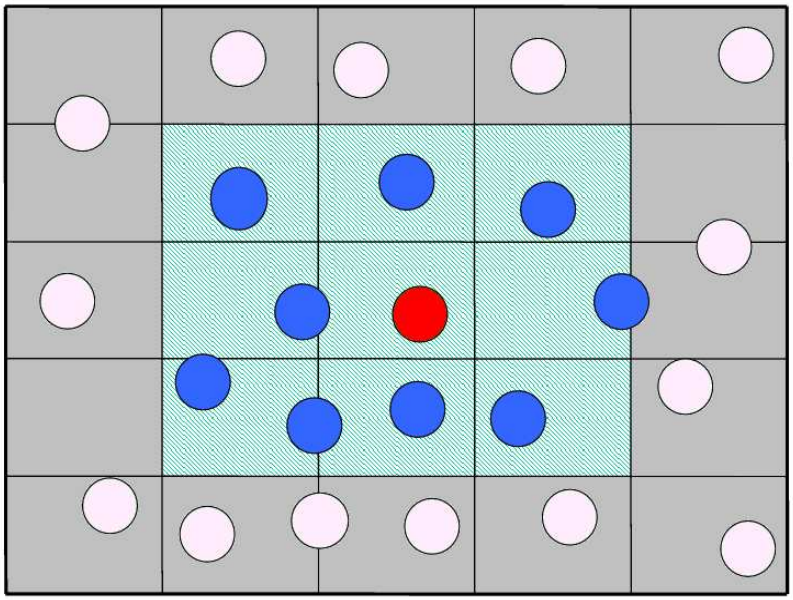

Figure 2.4: Division of simulation domain into smaller cells

in the neighboring cells need to be checked to determine the immediate collision which reduces the work from $O(N)$ to $O(1)$ per one collision scheduled. Further improvement is to postpone examining and updating the state of a particle until its collision. Suppose at time t an event involving a particular particle A is processed, only the state of A is examined and explicitly modified. The states of most other particles at t are not examined by the algorithm. In the present algorithm at any instant two copies of the global state vectors, the old and the new, are maintained so that the new vector is computed on the basis of the old one and, in turn, becomes the old one during the next cycle. The attraction of this algorithm is that it utilizes a simple and easy to handle double-buffering data structure, while avoiding costly actions (a) and (b). Problem (c) is handled in the algorithm using the standard technique of cell division. In most cases the algorithm examines and processes only

the events whose processing is unavoidable, e.g., particle collisions and boundary crossings. The processing of cell crossing naturally becomes additional operations in this method and their processing constitute the method's overhead. Theoretically, the cost reduces to $O(1)$ when using this method. Sometimes, like the naive algorithm, it also processes events whose examining is not necessary. However, the fraction of such overhead events is less than 15% in most experiments, and does not grow with N, while the speed-up due to the simplicity of data handling is substantial (Lubachevsky (1991)).

The necessary details of the simulation domain and the algorithm used are provided below.

2.3.1 Initialisation

The domain used for the present simulation work, Fig. 2.5, consists of a channel of length L_x along periodic x-direction and width L_z across periodic z-direction bounded by two physical walls L_y distance apart across y-direction. The walls are kept fixed. In the beginning of simulation, the particles are placed uniformly in a control volume of a specific dimension as shown. The particles are given random translational and rotational velocities as per the Gaussian distribution. The average initial velocity is set to zero for both the cases. The basic algorithm for event-driven simulation is given in Lubachevsky (1991).

2.3.2 Periodic Boundary Conditions

Periodic boundary conditions are intended to mimic very large systems i.e., the investigated system is thought to be much larger than the simulated number of particles. The particles are contained within a primary simulated volume; when a particle crosses the boundary of the simulation box, it re-enters from the opposite boundary as shown in Fig. 2.6. Thus, periodic boundary conditions allow the simulation to proceed as if the primary volume was surrounded by identical copies of itself. In the present case of granular Poiseuille flow, we impose periodic boundary conditions along x- and z-directions, see Fig. 2.5.

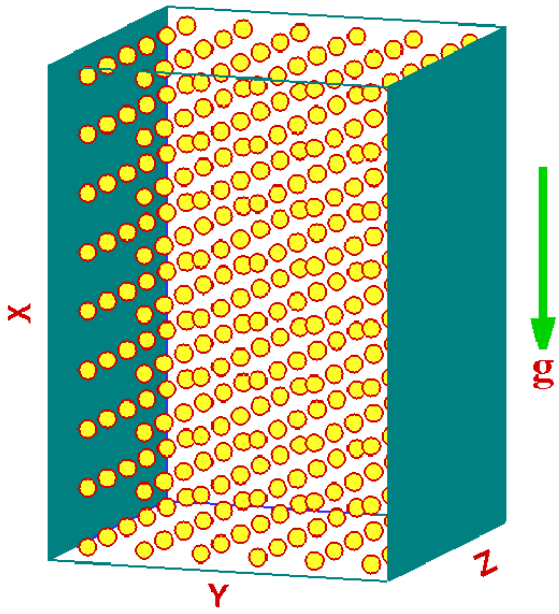

Figure 2.5: Initial arrangement of particles in a 3D box with physical walls

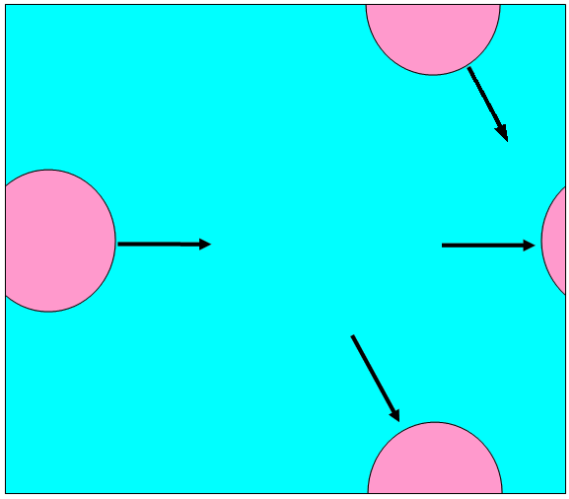

Figure 2.6: Periodic boundary condition.

2.3.3 Predict Event

Predicting future events after a collision or cell crossing is carried out by this subroutine *predictevent*.

Cellcrossing Event

In *predictevent*, besides calculating cell-crossing time for a particle we have to take into account the time taken by the particle to collide with physical walls in both directions of y-axis. The first part of the subroutine looks at possible cell-boundary crossings in all directions and picks the earliest one. In Fig. 2.7 we are showing a snapshot at a particular time with seven particles in x-y plane (z plane is not shown for clarity). The space is divided into nine cells. Next we calculate the time for cell-crossing and keep track of only minimum time required for this event for all particles. That time is defined as Q_{ik} for the ith particle.

$$Q_{ik} \stackrel{\text{def}}{=} cellcrossingtime\left(state\left[i, old[i]\right], time\left[i, old[i]\right], k\right) \tag{2.17}$$

where $1 \leq i \leq N$ and $1 \leq k \leq Ndim$. Here $Ndim$ is taken as 3 for 3D simulation i.e. k can take value 1, 2 and 3 according to cellcrossing in the x,y and z directions, respectively. After that $Q \stackrel{\text{def}}{=} min\left[Q_{ik}\right] = Q_{ik^*}$, and k^* is an index which provides this minimum (i.e. Q)
The minimum time is stored in Q. If the time taken for wall-collisions is minimum, then $signal \leftarrow 1$ and we update its *partnr* array as:

$$partnr\left[i, new[i]\right] \leftarrow N + Ndim + signal$$

On the other hand, if the time taken for the cellcrossing event is minimum, then $signal \leftarrow 0$ and we update *partnr* array as:

$$partnr\left[i, new[i]\right] \leftarrow N + Ndim + k$$

Collision Event

The important part of the algorithm examines every particle in cells that must be scanned for all possible collisions and determines whether a collision is possible or not. The interesting dynamics of hard-sphere system is embodied in collision rules; between collisions nothing happens and the particles move in straight lines (if there is no body force) or in parabolic paths (if there is gravity). Consider two identical particles i and j separated by a distance $\mathbf{r_{ij}} = \mathbf{r_i} - \mathbf{r_j}$ and having a relative velocity

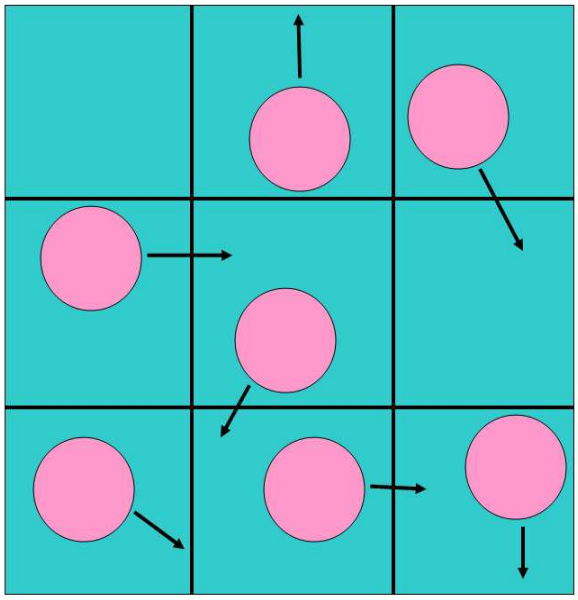

Figure 2.7: Particles undergoing cellcrossing event

$\mathbf{c_{ij}} = \mathbf{c_i} - \mathbf{c_j}$. These particles will collide when their separation becomes equal to their diameter d; if this happens it will occur at some time τ in the future, where τ is the smaller positive solution of

$$|\mathbf{r_{ij}} + \mathbf{c_{ij}}\tau| = d, \tag{2.18}$$

which is a quadratic equation in τ:

$$\tau^2 c_{ij}^2 + 2b_{ij}\tau + r_{ij}^2 - d^2 = 0. \tag{2.19}$$

If $b_{ij} = r_{ij} \cdot c_{ij} > 0$, then the particles are going away from each other and they will not collide. If $b_{ij} > 0$, it may still be true that $b_{ij}^2 - c_{ij}^2 \left(r_{ij}^2 - \sigma^2\right) < 0$, for which eqn.2.19 has complex roots and again no collision occurs. For other cases (assuming that the spheres are not overlapping), Fig. 2.8, two positive roots arise, the smaller of which corresponds to impact

$$\tau = \frac{-b_{ij} - \left[b_{ij}^2 - c_{ij}^2 \left(r_{ij}^2 - d^2\right)\right]^{1/2}}{c_{ij}^2}. \tag{2.20}$$

We store this value $[\tau + timenow]$ to P_{ij} which is defined as:

$$P_{ij} \stackrel{\text{def}}{=} collisiontime\left(state\left[i, old[i]\right], time\left[i, old[i]\right], state\left[j, old[j]\right], time\left[j, old[j]\right]\right) \tag{2.21}$$

where $1 \leq i, j \leq N$. Now $P \stackrel{\text{def}}{=} min\left[P_{ij}\right] = P_{ijj}$ and jj is that particular interacting particle which supplies this minimum i.e.P.
After getting P and Q, we have to compare their values to predict the final future event for the ith particle.
Case1 :
$Q < P$; ith particle is scheduled for cellcrossing event. It is indicated by $partnr\left[i, new[i]\right]$ array.

$$partner\left[i, new[i]\right] \leftarrow N + k^{*}$$

Case2 :
$Q \geq P$; ith particle is scheduled for collision event with jjth particle. It is indicated by

$$\begin{aligned} partner\left[i, new[i]\right] &\leftarrow jj, \\ partner\left[jj, new[jj]\right] &\leftarrow i, \end{aligned}$$

Advance Event

This function takes care of the particles when there is neither cellcrossing nor collision. Given a $state\left(i, old(i)\right)$ of a particle i at $time\left(i, old(i)\right)$ and a value $time\left(i, new(i)\right) \geq time\left(i, old(i)\right)$, returns $state\left(i, new(i)\right)$ this particle would have at $time\left(i, new(i)\right)$ ignoring possible interactions with other particles or obstacles on the interval $\left[time\left(i, old(i)\right), time\left(i, new(i)\right)\right]$:

$$state\left(i, new(i)\right) \leftarrow advance\left(state\left(i, old(i)\right), time\left(i, old(i)\right), time\left(i, new(i)\right)\right) \tag{2.22}$$

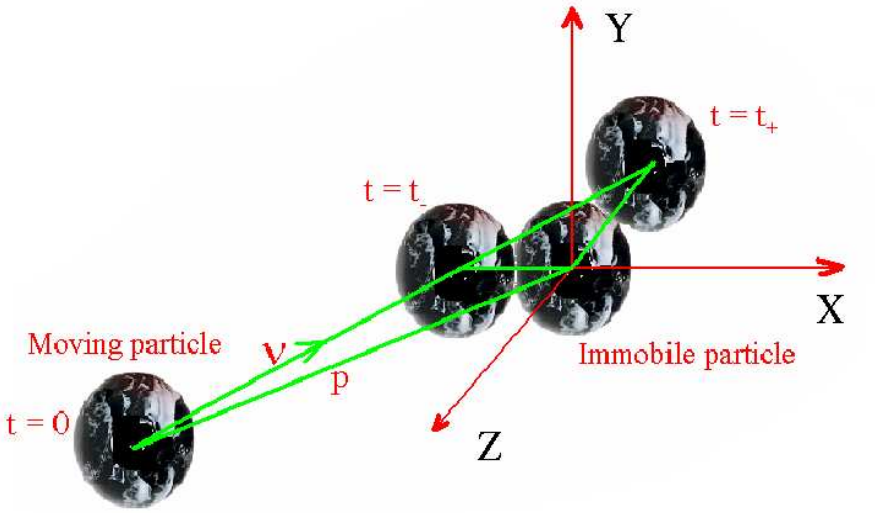

Figure 2.8: Geometrical meaning of two solutions of $|\vec{r_{ij}} + \vec{c_{ij}}\tau| = d$

In the absence of any external force (gravity, magnetic field, etc.), eqn.2.22 is of the form

$$\begin{aligned} position\,(i, new(i)) &\leftarrow position\,(i, old(i)) + \\ &\quad (time\,(i, new(i)) - time\,(i, old(i)))\, velocity\,(i, old(i))\,, \\ velocity\,(i, new(i)) &\leftarrow velocity\,(i, old(i)) \end{aligned}$$

which simply means the particles moves with $velocity\,(i, old(i))$ along a straight line starting from $position\,(i, old(i))$ at $time\,(i, old(i))$ as can be seen in Fig. 2.9.

Here the two arrays $new[1 : N]$ and $old[1 : N]$ with elements equal 1 or 2 are maintained. The value $new[i]$ is the pointer to the new event for component i and the value $old[i]$ is the pointer to the old event for component i. When $new[i]$ is updated, $old[i]$ is also updated immediately, so that relation $new[i] + old[i] = 3$ remains invariant (Lubachevsky 1991).

2.3.4 Delayed Update

When scheduling an interaction (event), the algorithm performs *advance* and *jump* (which involves predicting the *new_state* after the interaction from the given *state*) operations. If the event is later preempted, these computations are wasted and

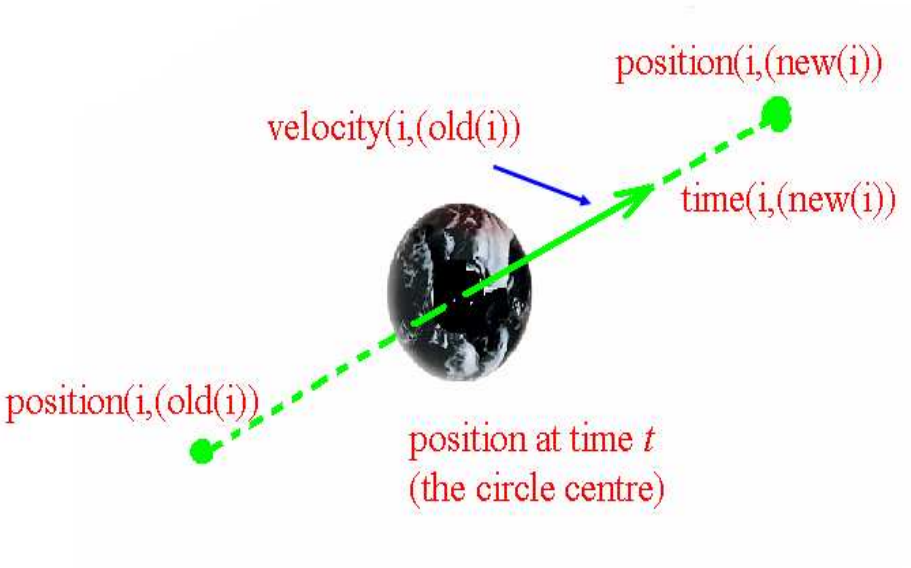

Figure 2.9: The particle i at time *timenow*. Its state is required to be updated in *cellcrossing* or *pre-collisional* event

hence results in inefficiency in the algorithm.

To remove this inefficiency, the applications of *advance* and *jump* should be delayed until the latest possible moment when the scheduled event is being processed. This saves considerable amount of computational time. Thus, if at time t an event involving a particle i is processed, only the state of that particle i is examined and explicitly modified. The states of most other particles need not be known at t and are not examined by the algorithm.

2.4 Method of Averaging

In the present granular flow simlulation (see Fig. 2.5), the energy enters into the system by the acceleration of particles due to gravity. Simultaneously, the energy is lost due to inelastic collisions (particle-particle and particle-wall collisions). When these two processes *i.e.*, the energy gain and the energy dissipation, balance each other, the system attains a non-equillibrium steady state. The system kinetic energy is monitored to get an idea of the steady state.

The statistical measurements of various quantities are performed only when the system has reached a steady state condition. After the steady state, the microscopic properties of the flow like local mean velocity(U), local mean rotational velocity(ω),

translational granular temperature(T), rotational granular temperature(θ) and system density(ϕ) remains invariant in time, but have spatial variations along the y-direction in fully developed granular Poiseuille flow.

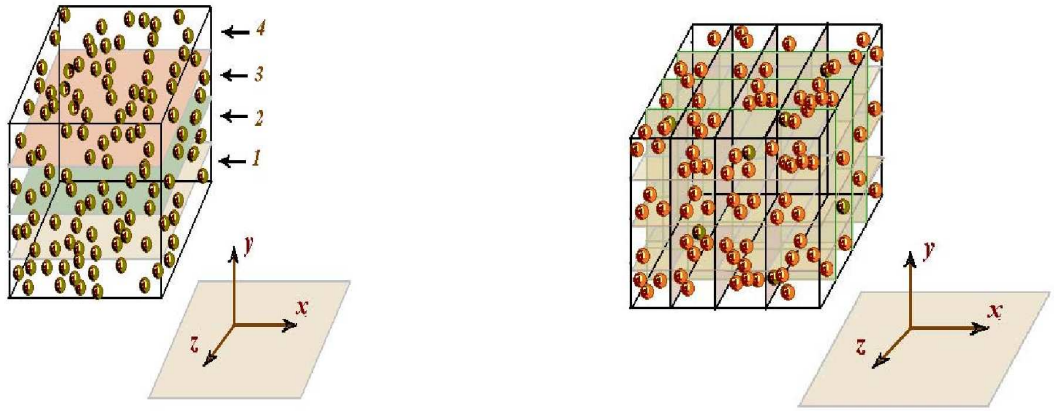

(a) Binwise averaging (b) Cellwise averaging

Figure 2.10: Schematic diagram of methods of averaging (Gayen (2007))

All the statistical quantities are calculated by two averaging methods depending on the degree of density inhomogeneity in the system. The first is *binwise averaging* and the other is *cellwise averaging*. When there is inhomogeneity across only one direction (generally across the channel width), the simulation domain is divided into a number of *bins* across the width, as shown in Fig. 2.10(a).The data in each bin is averaged seperately over a large number of collisions, depending on the control parameters and quantities to be measured. When the system size is increased (large number of particles), the density inhomogeneity is observed over the whole system. Thus, in such cases, the simulation domain is divided into a number of cells, *i.e.* both the height as well as the width are divided into bins (resulting in *cells* in y-z plane) as shown in Fig. 2.10(b). The data is averaged over each *cell* for calculating the fluctuating velocities and other quantities.

2.5 Code Validation

For the present simulation work, the shear-flow code developed by Bishakhdatta Gayen (2007) in fortran77 forms the basic structure. It was then modified consid-

erably by removing the *shear force* and incorporating the "rigid boundary walls" across the width of the channel. It was fully converted into fortran90 from fortran77 by which a significant gain in running speed by a factor of 2 was obtained. This gain in running time is a considerable achievement since it enables us to simulate a large number of particle (of the order 10^5) which otherwise would have taken a long time.

For the validation of the code used in this work, the results are compared with those using a serial code based on the algorithm given in Allen & Tildesley (1987). The results in Fig. 2.11 are based on simulation of $N = 1000$ particles for a volume fraction of $\phi = 0.01$ in a cubic domain. The coefficients of restitution are $e = 0.8$, $\beta = 0.99$, $e_w = 1.0$ and $\beta_w = 1.0$. Each of the plot shown in Fig. 2.11 is based on the corresponding non-dimensional quantity. These plots show that the results from our code and those from the code based on Allen & Tildsley's algorithm are matching within acceptable limits.

Fig. 2.11(a) shows the streamwise linear velocity profile (U_x) across the channel width. There is considerable slip at the wall. The velocity gradient is also higher near the wall in comparison to the center of the channel.

Fig. 2.11(b) shows the rotational velocity (ω_z) across the channel width. The rotational velocity is negative in lower portion of the channel and positive in the upper portion because of the roughness of the stationary walls and hence the particles can be considered to be rolling on the stationary wall in the streamwise direction.

Fig. 2.11(c) shows the density profile across the channel width. The density is higher at the center of the channel, but nearly uniform across the channel width indicating the absence of any cluster formation.

Fig. 2.11(d) shows the translational granular temperature across the channel width. The large temperature near the wall is due to large velocity gradients present there. Due to these large velocity gradients, the impact velocity of the particles is large which results in higher random velocity of the particles and hence there is enhancement of granular temperatures near the walls.

Fig. 2.11(e) shows the rotational granular temperature across the channel width. Here also we see the same variation as we have seen for the tranlational granular temperature because of the already mentioned reasons in the above paragraph.

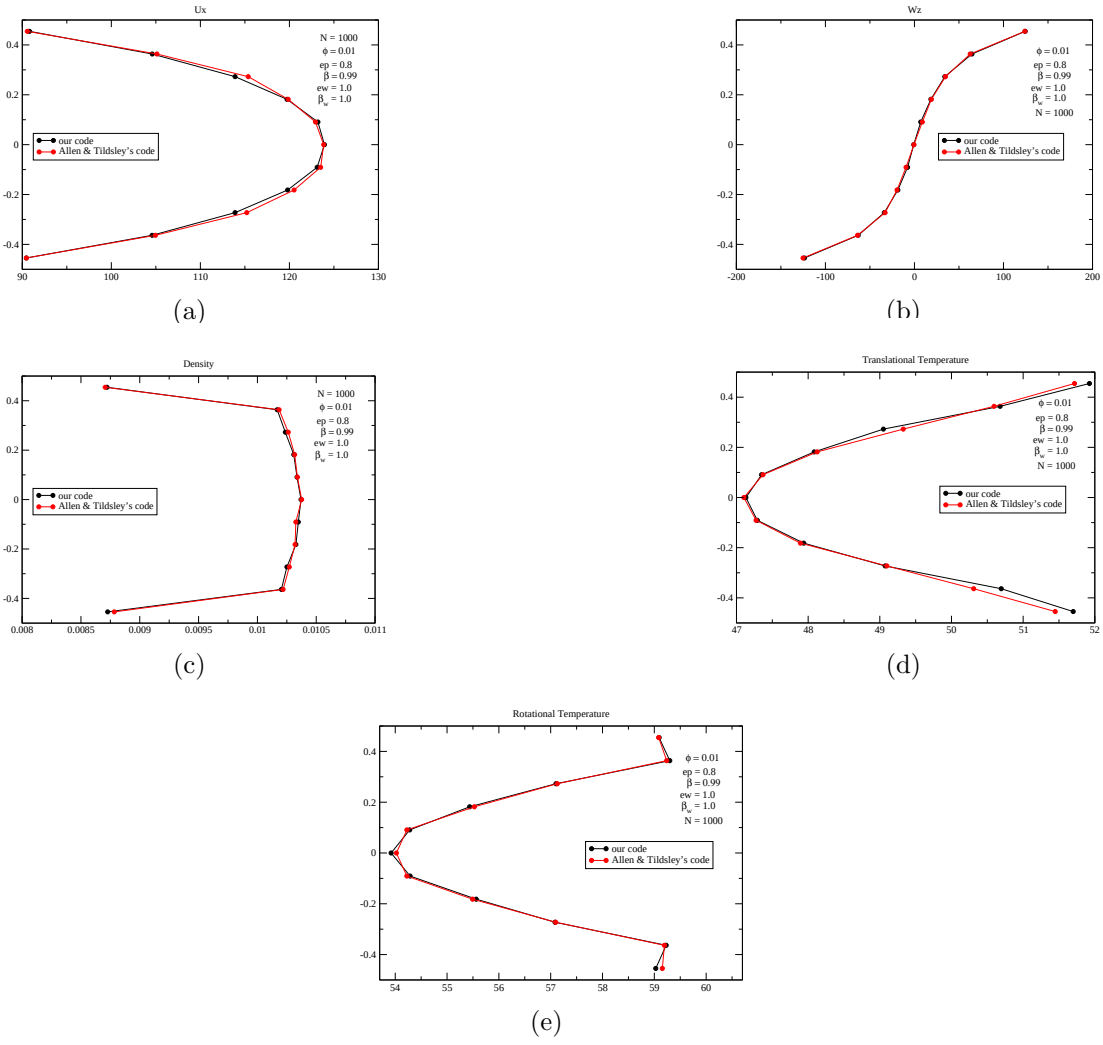

Figure 2.11: Validation of the code used in present work: (a) linear velocity profile, (b) angular velocity profile, (c) density profile, (d) translational temperature and (e) rotational temperature

CHAPTER 3

BOLTZMANN LIMIT OF GRANULAR POISEUILLE FLOW

Unlike the molecular fluid for which the Maxwell-Boltzmann distribution plays the role of the 'equilibrium' velocity distribution function, the granular fluid does not posses any 'equilibrium' state due to the microscopic dissipation due to inelastic particle collisions. However, there are 'non-equilibrium' (driven) steady states for various canonical granular flow configurations for which the Gaussian distribution is the leading order velocity distribution in appropriate limits. A systematic study of distribution functions is, therefore, of interest from the viewpoint of developing constitutive models for granular flows as well as to pinpoint the range of validity of any adopted theory. Investigating the correlations in the fluctuations of the particle motion can yield insight into caging and diffusion of particles. Having a measure of the correlations is important in developing a hydrodynamic description for granular materials and interpretation of variables used to characterize their properties.

This chapter discusses the results for the granular Poiseuille flow at a very low density, also known as Boltzmann limit. In the low density limit, the granular fluid behaves like a gas. The simulation results in the Boltzmann limit can be used to validate kinetic theory models of a granular gas (Goldhirsch (2003)).

All the results presented in this chapter are for a volume fraction $\phi = 0.01$, with the number of particles being N = 2744; the normal and tangential coefficients of restitution for wall collisions are e_w=1.0 and β_w=1.0, respectively. Note that $\beta_w = 1$ corresponds to a rough wall. The simulation is done in a cubic domain with W/d = 50 = L/d = H/d, see Fig. 3.1. These parameters are kept constant throught the simulation for the present set of results.

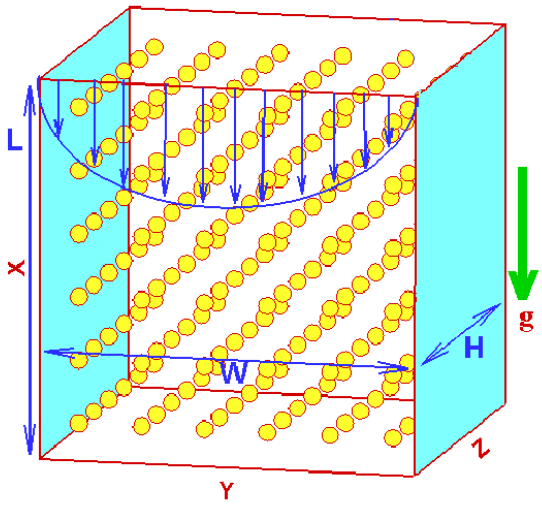

Figure 3.1: Cubical domain used in the simulation.

3.1 Mean Field Quantities

This section gives a brief description about the profiles of various mean field quantities such as translational granular temperature (T), rotational granular temperature (θ), mean translational velocity (U_x), mean rotational velocity (ω_z) and volume fraction (ϕ). All these mean field quantities vary across the wall-normal direction (y), see Fig. 3.1. The domain is divided vertically into 25 bins for all cases unless otherwise stated. Bin=1 is touching the $left$ wall, bin=13 is located at the middle of the domain and bin=25 touching the $right$ wall. In order to avoid the effects of density inhomogeneities across the domain, all fluctuating velocities are calculated by *cellwise* averaging and the above mentioned macroscopic quantities are calculated using *binwise* averaging method. For further details please refer to the section "Methods of averaging" in Chapter-2.

After implementing the averaging methods, the macroscopic quantities are cal-

culated as follows:

$$\begin{aligned}
\phi(y) = \langle \phi_{\mathbf{k}} \rangle &= \left\langle \frac{\pi}{6} \frac{N_k d^3}{V_k} \right\rangle \\
U_x(y) = \langle \mathbf{c}^{\mathbf{k}} \rangle &= \left\langle \frac{1}{N_k} \sum_j c_j \right\rangle \\
\omega_z(y) = \langle \omega^{\mathbf{k}} \rangle &= \left\langle \frac{1}{N_k} \sum_j \omega_j \right\rangle \\
T(y) = \frac{1}{3} \langle \mathbf{C} \cdot \mathbf{C} \rangle &= \left\langle \frac{1}{3N_k} \sum_j (c_j - \langle c_j \rangle)(c_j - \langle c_j \rangle) \right\rangle \\
\theta(y) = \frac{I}{3m} \langle \mathbf{\Omega} \cdot \mathbf{\Omega} \rangle &= \left\langle \frac{I}{3mN_k} \sum_j (\omega_j - \langle \omega_j \rangle)(\omega_j - \langle \omega_j \rangle) \right\rangle
\end{aligned}$$

where d is the diameter and m is the mass of a particle, taken as unity, ϕ_k is the volume fraction, N_k is the number of particles and V_k is the volume of the kth cell; the angular bracket denotes a time average. Here $\mathbf{c}$ is the instantaneous and $\mathbf{C} = \mathbf{c} - < \mathbf{c} >$ is the fluctuating translational velocity of a particle; ω and $\mathbf{\Omega} = \omega - \langle \omega \rangle$ are instantaneous and fluctuating rotational velocities, respectively; $\langle \mathbf{c}^{\mathbf{k}} \rangle$ and $\langle \omega^{\mathbf{k}} \rangle$ denote the mean translational and roational velocity of kth cell, respectively. T and θ are the translational and rotational granular temperatures, respectively; I is the moment of inertia of a particle.

The above mentioned mean field quantities are non-dimensionalized by the following scaling:

$$\begin{aligned}
u_x^* &= \frac{u_x}{\sqrt{gd}} \\
\omega_z^* &= \frac{\omega_z}{\sqrt{g/d}} \\
T^* &= \frac{T}{dg} \\
\theta^* &= \frac{\theta}{gd}
\end{aligned}$$

where g is the acceleration due to gravity, u is the linear and ω is angular velocity of the particles. In the following, we ascertain the effects of particle "roughness"

(β, tangential restitution coefficient for particle-particle collision) and "inelasticty" (e, normal restitution coefficient) on all mean-field quantities.

Smooth particles ($\beta \rightarrow -1$)

For nearly smooth particles with β=-0.99, Figs. 3.2 (a)-(c) show typical snapshots for e=0.8 in the (x,y), (x,z) and (y,z)-planes, respectively. The corresponding time-evolution of the translational granular temperature is shown in Fig. 3.2(d). The snapshots in Figs. 3.2 (a)-(c) correspond to a steady-state marked by an arrow in Fig. 3.2(d). It is seen from Figs. 3.2 (a)-(c) that there is no dissipation-induced density inhomogeneity in the system even at $e = 0.8$. The density field across the y-direction is shown in Fig. 3.3(a). When the dissipation is very less, e=0.99, the density profile is nearly uniform across the width of the channel. However, as the dissipation is increased we see that the particles shift towards the center and hence the volume fraction is higher at the center, specifically for e=0.8, even though there is no visible *clustering* or *structure formation*. In a region of increased density, the rate of collisions is higher than the neighbouring less-dense domains. Since the collisions are inelastic, the granular temperature decreases, see Fig. 3.3(d), and consequently the pressure in the dense regime decays faster than the neighbouring regions. This leads to the migration of particles and thereby further increase of the density until this self-amplifying process is stopped by diffusion or other mechanisms.

The mean linear velocity (U_x) profile in Fig. 3.3(b) shows that as the dissipation is increased to e=0.8 the velocity gradient across the channel width increases because of shifting of particles towards the center. The slip velocity at the walls also increases with dissipation as evident from Fig. 3.3(b). The rotational velocity (ω_z) is positive in the upper half of the channel and negative in the lower half as expected and it has an almost linear profile in the elastic limit e=0.99. The variation of the rotational granular temperature (θ) in Fig. 3.3(e) is found to be opposite to that of translational granular temperature. This could be a consequence of rough walls ($\beta_w = 1$).

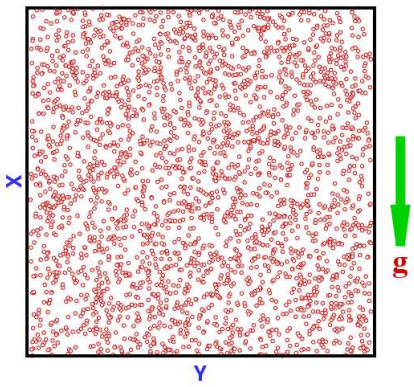

(a) Particle positions- xy-plane

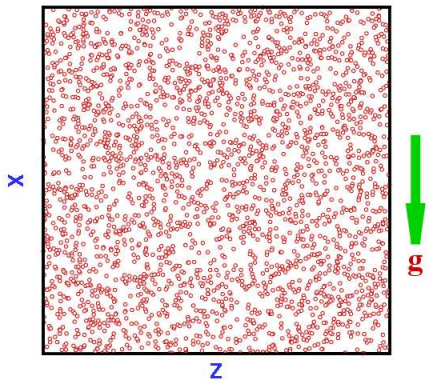

(b) Particle positions- xz-plane

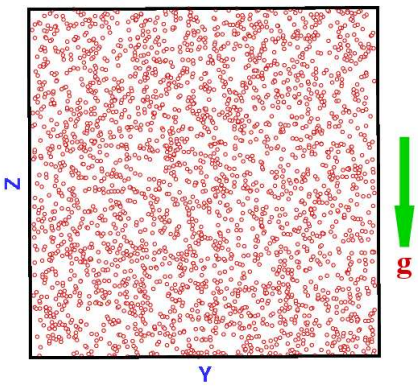

(c) Particle positions- yz-plane

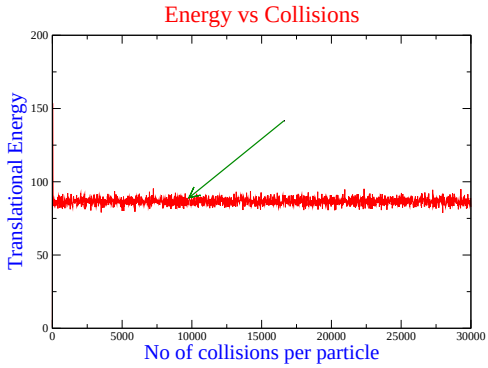

(d) Time trace of average kinetic energy

Figure 3.2: Nearly smooth particles (β=-0.99, e=0.8). N=2744, L/W=1.0, W/d=50, H/d=50, ϕ=0.01, e_w=1.0, β_w=1.0.

Rough particles ($\beta = 0$)

For β=0 case, i.e. particles with a rough surface for which the post-collisional tangential velocity is zero, Figs. 3.4 (a)-(c) show typical snapshots for e=0.8. As expected, there is no dissipation-induced structure formation in the system.

Since for β=0, there is additional rotational energy dissipation compared to the smooth case of β=-0.99, the volume fraction is much higher in the center region even for nearly elastic particles, see Fig. 3.5(a). This further results in higher velocity gradients for U_x, Fig. 3.5(b), and consequently lower granular temperatures in the center, Fig. 3.5(d) and Fig. 3.5(e). There is also higher slip velocity at the walls and

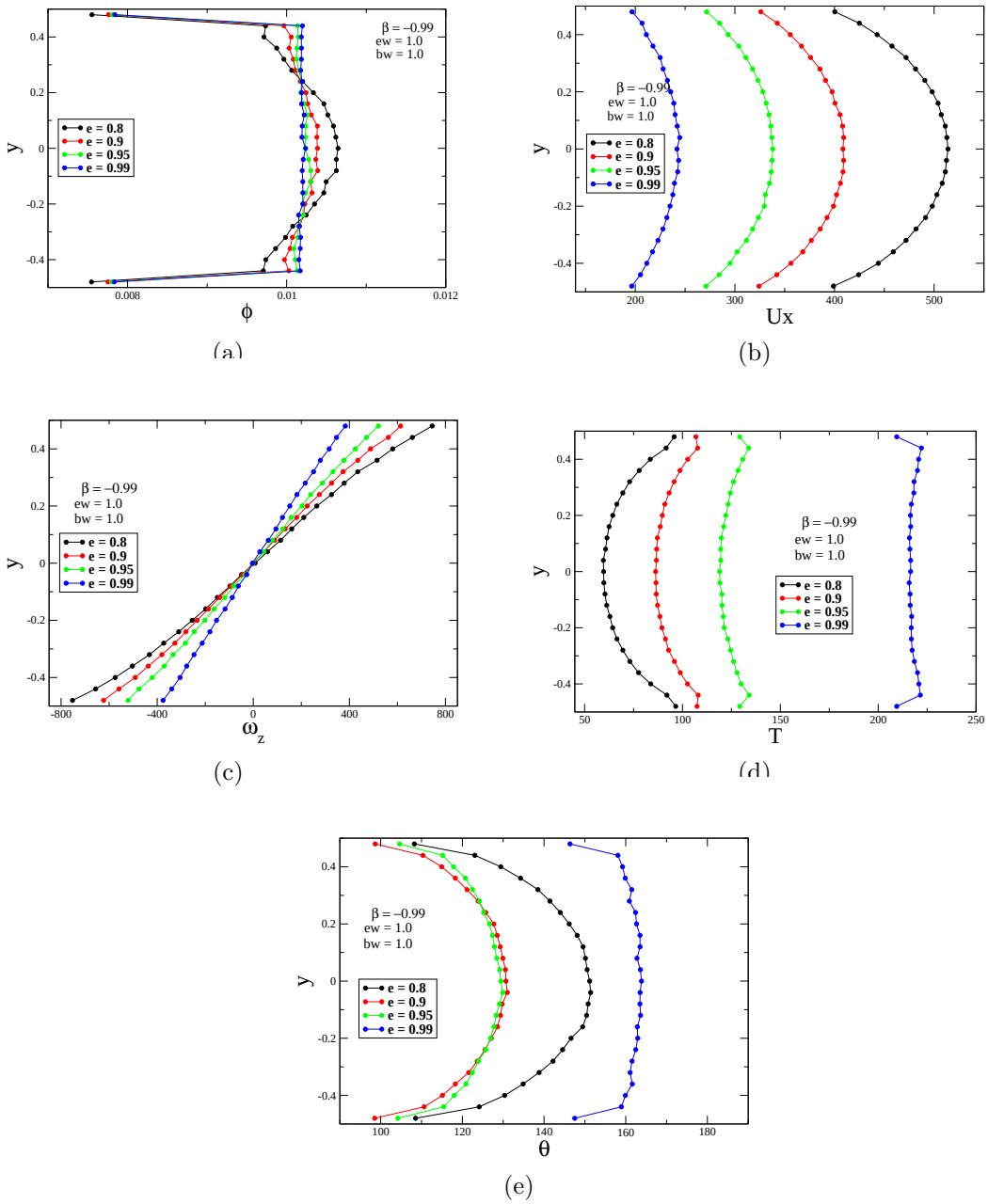

Figure 3.3: Nearly smooth particles (β=-0.99). Other parameters as in Fig. 3.2 (a) volume fraction, (b) mean linear velocity (U_x), (c) mean rotational velocity (ω_z), (d) translational granular temperature (T) and (e) rotational granular temperature (θ).

that too increases with dissipation. The rotaional velocity (ω_z) profiles in Fig. 3.5(c) for any e deviate from linear such that the rotational velocity gradients are much

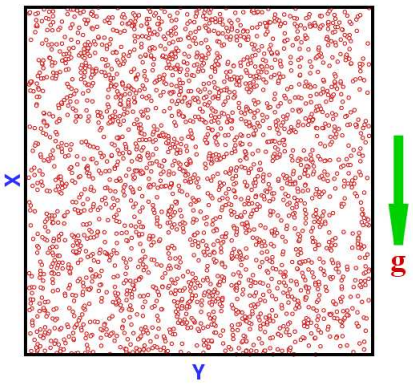

(a) Particle positions- xy-plane

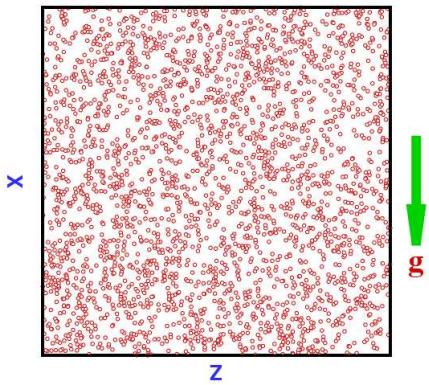

(b) Particle positions- xz-plane

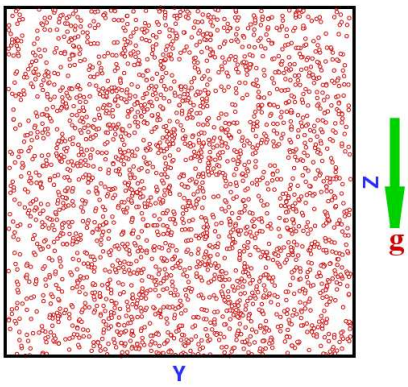

(c) Particle positions- yz-plane

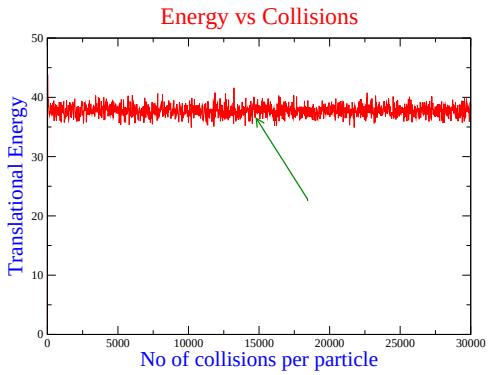

(d) Time trace of average kinetic energy

Figure 3.4: Rough particles (β=0, e=0.8). Other parameters as in Fig. 3.2

higher near the wall in comparison to that for smooth particles in Fig. 3.3(c).

Perfectly rough particles ($\beta \rightarrow 1$)

For almost perfectly rough particles with $\beta = 0.99$, Figs. 3.6 (a)-(c) show typical snapshots for e=0.8 at a time marked in Fig. 3.6(d). Again, we see there is no dissipation-induced inhomogeneity in the system across any plane.

From Fig. 3.7, it is observed that the system behaves almost like the case for β=-0.99. In the present situation the particles reverse their spin after collisions and hence there is a considerable loss in rotational kinetic energy, due to which the

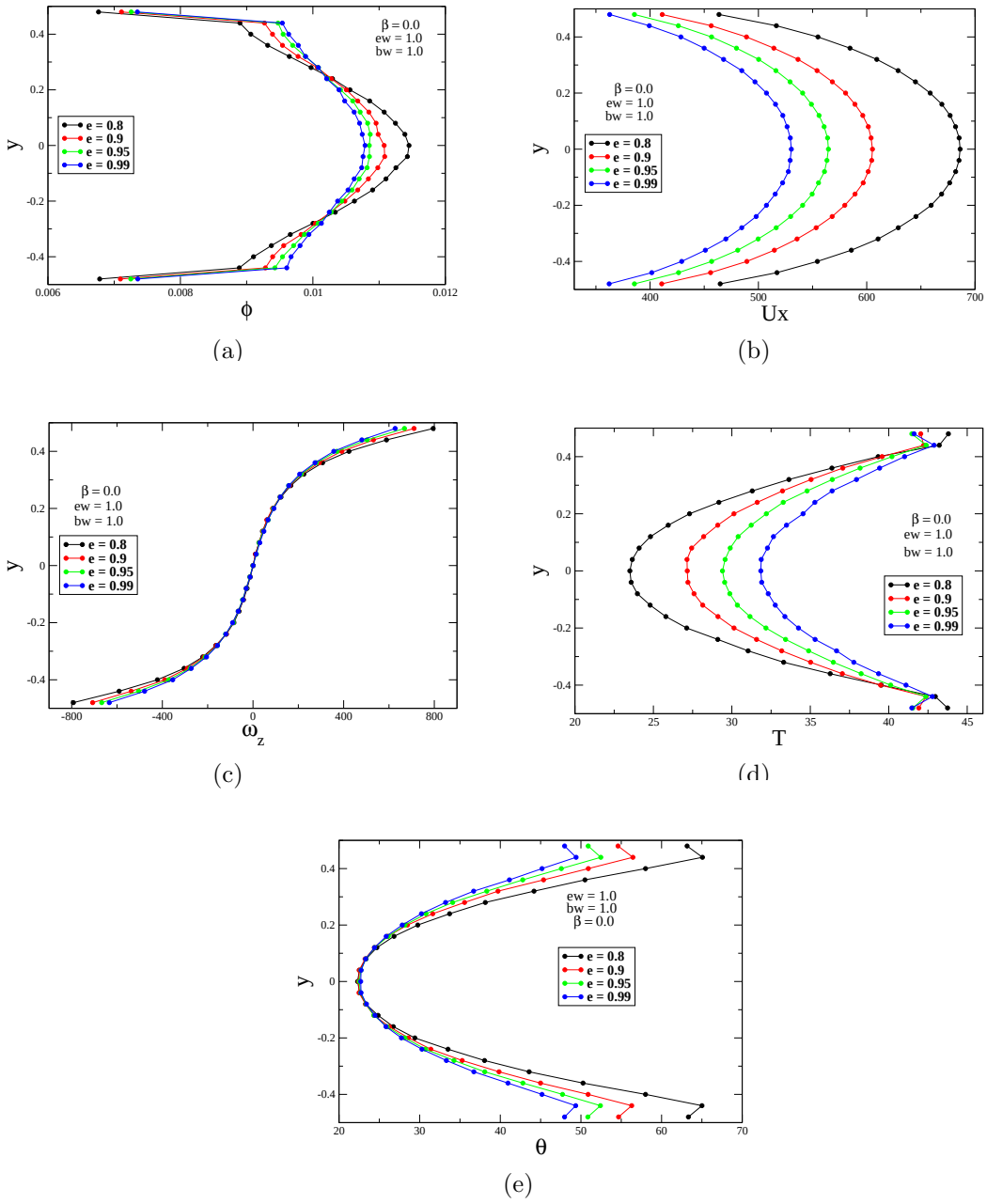

Figure 3.5: Rough particles (β=0). Other parameters as in Fig. 3.2. (a) volume fraction, (b) mean linear velocity (U_x), (c) mean rotational velocity (ω_z), (d) translational granular temperature (T) and (e) rotational granular temperature (θ).

rotational velocities are less in magnitude, Fig. 3.7(c), in comparison to β=-0.99. We have translational as well as rotational temeperature minima at the center of the channel, see Fig. 3.7(d) and Fig. 3.7(e).

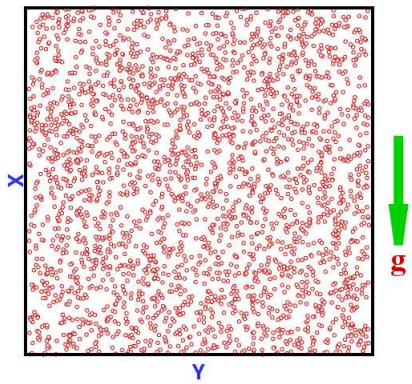

(a) Particle positions- xy-plane

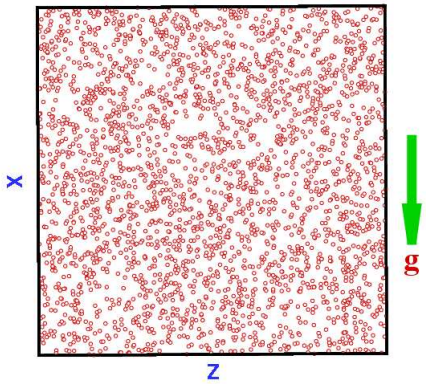

(b) Particle positions- xz-plane

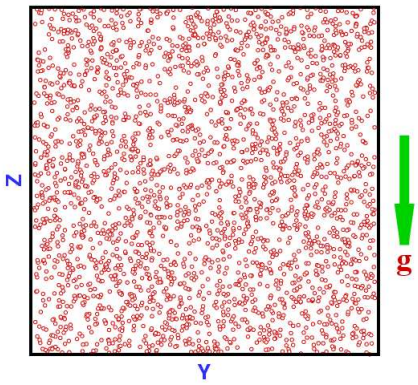

(c) Particle positions- yz-plane

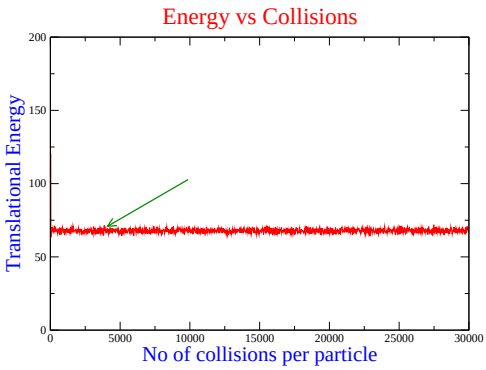

(d) Time trace of average kinetic energy

Figure 3.6: Perfectly rough particles (β=0.99). Other parameters as in Fig. 3.2

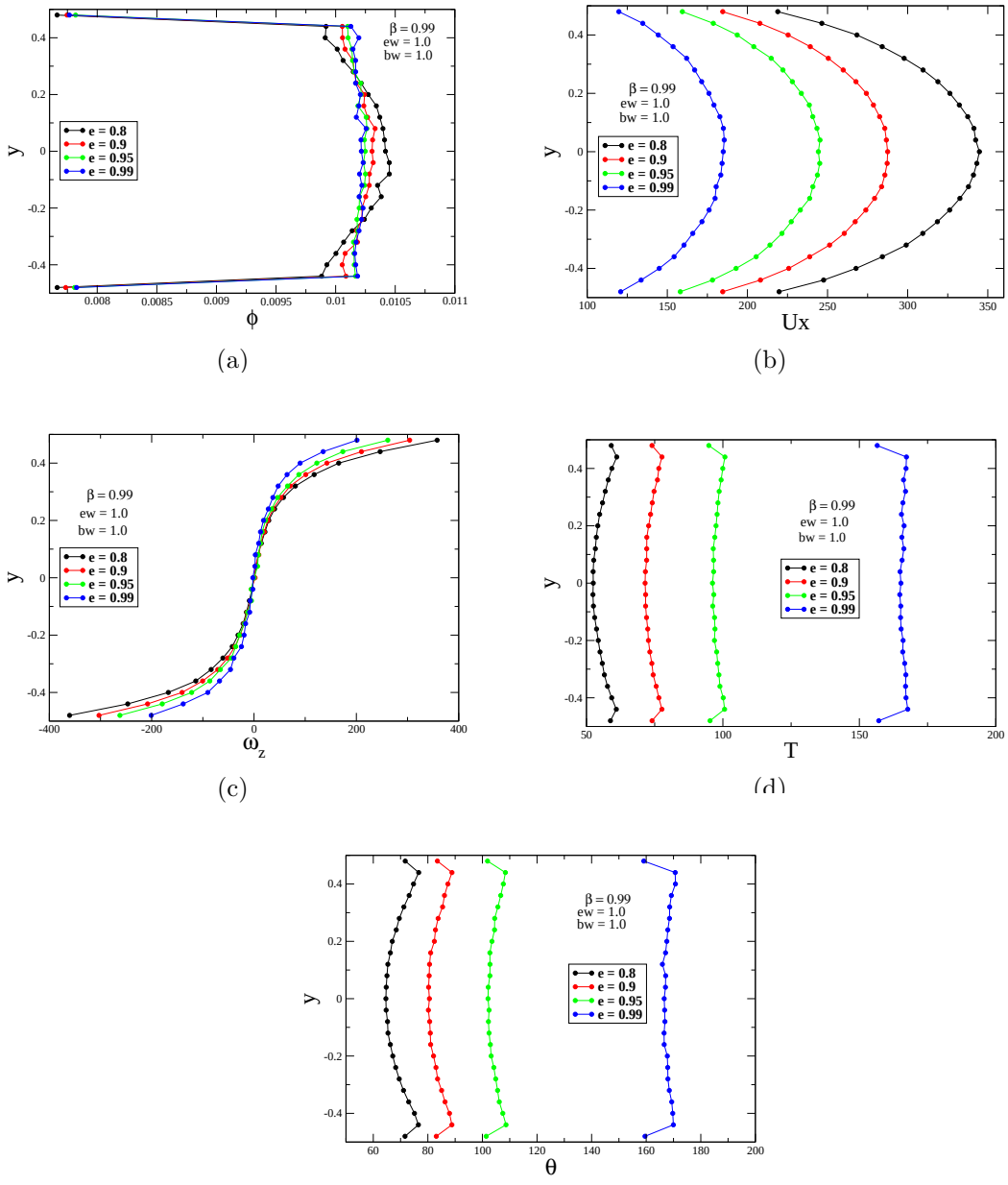

Figure 3.7: Perfectly rough particles (β=0.99). Other parameters as in Fig. 3.2 (a) volume fraction, (b) mean linear velocity (U_x), (c) mean rotational velocity (ω_z), (d) translational granular temperature (T) and (e) rotational granular temperature (θ).

3.1.1 Slip velocities and gradients

In continuum mechanics, the no-slip condition at the fluid-solid interface is imposed. But it has been confirmed by numerous experimental and numerical works that fluid flows indeed exhibit a finite slip. The magnitude of slip depends on various factors like the length scales of the flow, surface roughness, hydrophobicity, nature of fluid, etc.

Gas flows show significant slip when the Knudsen number is large, for which the continuum assumption breaks down. Knudsen number is defined as the ratio of the mean free path of the gas molecules to the characteristic length of the flow, i.e. $Kn{=}\lambda/L$, where the mean free path λ is computed by averaging the distance ($l = \sqrt{\delta x^2 + \delta y^2 + \delta z^2}$) covered by the particles during succesive collisions and L is the length of the simulation domain.

We have seen considerable amount of slip at the walls in the translational as well as rotational velocity profiles discussed in previous sections. Here the results on slip velocity for the gravity driven granular Poiseuille flow are discussed in some more detail. In the present work all the quantities at the walls are average values of two bins adjacent to the left and right walls. The Knudsen number is calculated as $Kn = \lambda/W$ where W is the width of the channel. It is found that the slip velocity depends on various control parameters like coefficients of restitution e and β, volume fraction ϕ, wall roughness, etc.

First we study the effect of different control parameters on Knudsen number. Fig. 3.8 shows that Kn increases with dissipation, as e decreases from 0.99 to 0.8. This can be explained from the similarity with gas molecules. At a higher energy state, i.e. $e \sim 1$, the agitation of particles is more and hence the collision frequency increases. This leads to a smaller mean-free path and hence smaller Kn. The probabilty distribution of mean-free path (l) is shown in Fig. 3.9 for β=0.99, β=0.0 and β=-0.99. For all cases, the tails of $P(l)$ appear to follow an exponential as in a molecular gas.

The effect of e and β on the slip velocity is presented in Fig. 3.10 (a,b). The normal coefficient of restitution e has significant effects on the slip velocity, as was observed from velocity profiles in Fig. 3.7(b), Fig. 3.5(b) and Fig. 3.3(b). The slip for translational and rotational velocities increases with increasing dissipation. The slip is larger for the smooth limit β=-0.99 than the spin reversal case β=0.99, but the slip is largest for β=0.

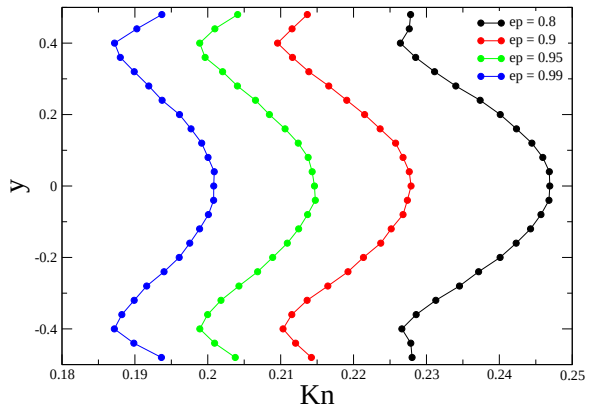

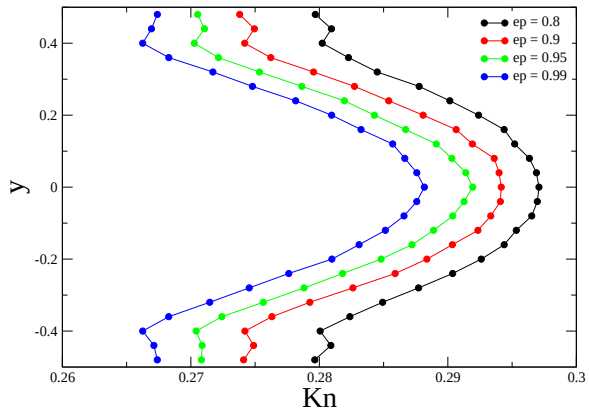

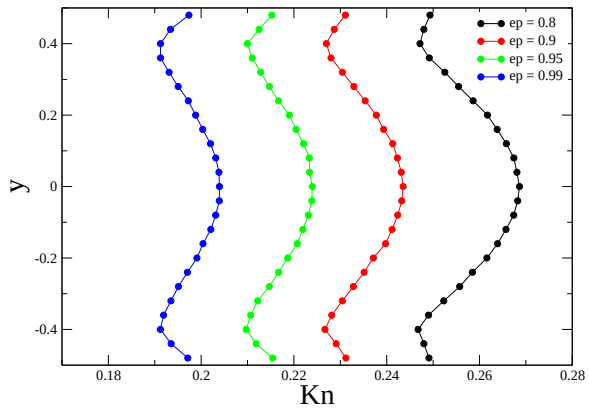

(c)

Figure 3.8: Effect of e on Kn for (a) β=0.99, (b) β=0 and (c) β=-0.99. Other parameters as in Fig. 3.2

In addition to the velocity slip, the gases also exhibit *temperature jump*. The temperature jump is defined as the difference between the temperature of the

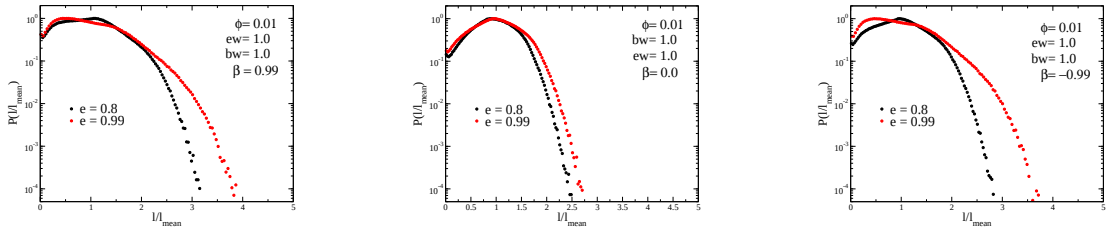

(a) (b) (c)

Figure 3.9: Effect of e on mean free path distribution for (a) β=0.99, (b) β=0 and (c) β=-0.99. Other parameters as in Fig. 3.2

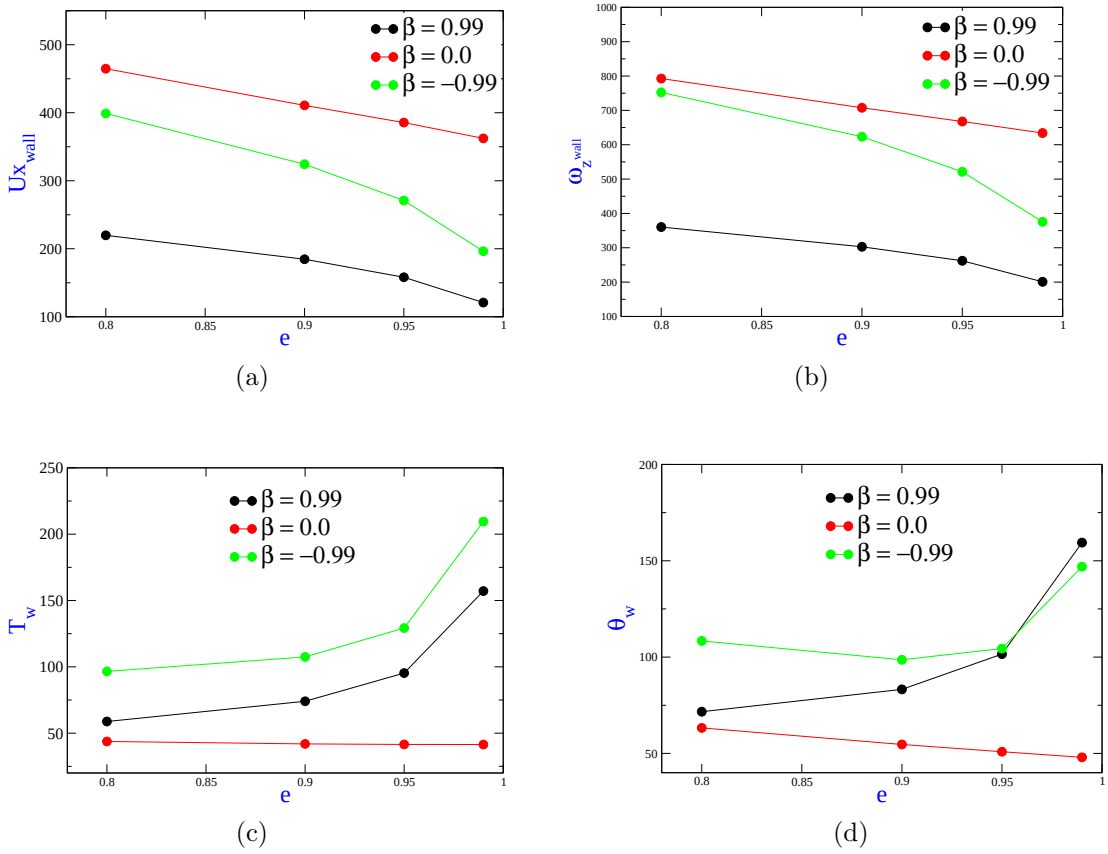

(a) (b) (c) (d)

Figure 3.10: Effect of e on slip velocities and temperature jump: (a) translational slip velocity, (b) rotational slip velocity, (c) translational temperature at wall and (c) rotational temperature at wall. Other parameters as in Fig. 3.2

fluid near the wall (T_w) and the temperature of the wall (T_s). The translational granular temperature near the wall (T_w) decreases with increasing dissipation, see Fig. 3.10(c), since the particles loose energy in the inelastic collisions and that leads

to cooling. However, for the case of rough particles, β=0, there is negligible effect of e on T_w which has smaller temperature jumps because the dissipation of energy at the walls due to wall-particle collisions is large. The rotational temperature near the wall (θ_w) also has a similar dependence on e like the rotational velocity, shown in Fig. 3.10(d). However, for rough particles, there is an increase in θ_w with increasing dissipation.

Fig. 3.11(a) presents the effect of dissipation on translational velocity gradient near the walls whose magnitude increases with dissipation (e) for all β. Similarly, the rotational velocity gradient also increases with dissipation as shown in Fig. 3.11(b). The gradient in translational temperature near wall decreases with increasing dissipation for both $\beta = 0$ and $\beta = 0.99$, however, for $\beta = -0.99$, it behaves non-monotonically with e. A similar variation is observed for the gradient of rotational temperature in Fig. 3.10(d).

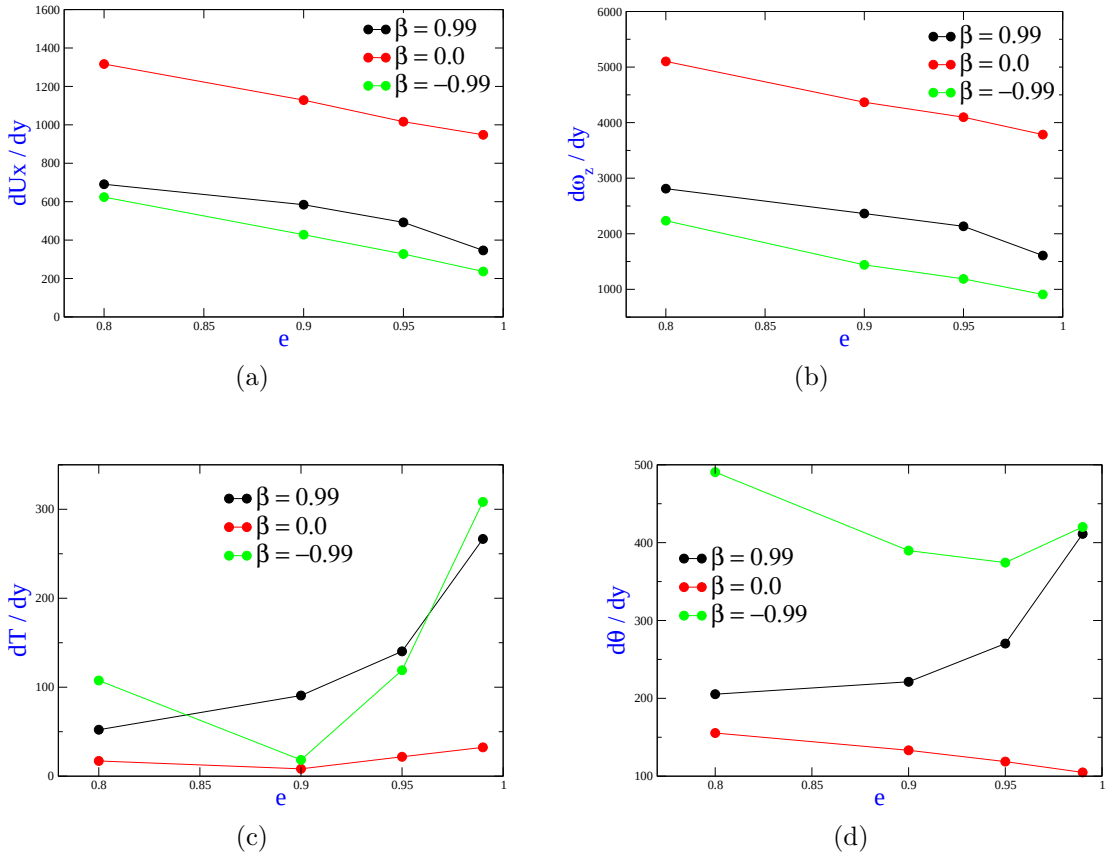

Figure 3.11: Effect of e on velocity and temperature gradients: (a) translational velocity gradient at wall, (b) rotational velocity gradient at wall, (c) translational temperature gradient at wall and (c) rotational temperature gradient at wall. Other parameters as in Fig. 3.2

3.2 Velocity Distribution Function (VDF)

This section presents results for velocity distribution functions (VDF) for translational and rotational fluctuation velocities in the dilute limit ($\phi = 0.01$) and the effect of various control parameters on them. The fluctuating velocities are calculated based on cell-wise averaging as explained in Chapter-2. The simulation domain is divided across y-direction into 25 bins for all cases unless otherwise stated: bin=1 is touching the $left$ wall, bin=13 is located at the middle of the domain and bin=25 touching the $right$ wall. An increase in the number of bins did not affect the results significantly and hence 25 bins are used throughout this work. It should be noted that bins across x-direction were also used to check the effect of possible inhomogeneities, but there were negligible variation across the bins in x-direction and hence the bins in x-direction are avoided. Note that the horizontal axis of the velocity distribution functions is scaled by σ, the standard deviation of the given quantity and the vertical axis is scaled such that $P(0) = 1$.

Smooth particles ($\beta \rightarrow -1$)

Here we present the VDFs for smooth particles $\beta = -0.99$. Fig. 3.12 shows the probability distribution function of all the velocity components for e=0.8. The black dashed line in each panel represents the Gaussian distribution. It is observed that $P(C_x)$ is asymmetric, Fig. 3.12(a). It deviates from the Guassian distribution towards negative side. Similarly there is significant dissipation induced asymmetry in the $P(\Omega_z)$ distribution. However, $P(C_y)$, $P(C_z)$, $P(\Omega_x)$ and $P(\Omega_y)$ distributions are symmetric but there are noticeable deviations at tail region from the Gaussian.

We have seen that there is negligible difference in the local (binwise) distribution functions of different bins. Hence to see the effect of dissipation, for sake of clarity, we present the results only for the middle bin (bin=13). Fig. 3.13 presents the effect of dissiaption, e, on the probability distribution functions. Fig. 3.13(a) shows that as the dissipation is increased, the $P(C_x)$ distribution tail deviates away from the Gaussian towards negative side; $P(C_y)$ also exhibits deviations in the tail region with increase of dissipation but maintaining the symmetry. However $P(C_z)$, $P(\Omega_x)$ and $P(\Omega_y)$ has little effect of dissipation. On the other hand, $P(\Omega_z)$ shows deviation from Gaussian in its tails as well as in the low velocity region and as $e \rightarrow 1$, $P(\Omega_z)$

approaches a Gaussian. The rough wall ($\beta_w = 1$) is possibly playing a significant role for non-Gaussian VDFs for smooth ($\beta \rightarrow -1$) and elastic ($e \rightarrow 1$) particles.

Rough particles ($\beta = 0$)

Here we present results on the velocity distribution functions for rough particles. We can see that the dissipation due to surface roughness, β=0, introduces interesting asymmetric features in the $P(C_x)$ distribution, Fig. 3.14(a). The $P(C_x)$ distribution deviates considerably from Gaussian distribution towards negative side. This deviation is present in all bins. The $P(C_y)$, $P(C_z)$, $P(\Omega_x)$ and $P(\Omega_y)$ distributions remain symmetric but there is larger deviation at the tail regions, in comparison to smooth surface condition. However, there is asymmetry in the low velocity region of $P(\Omega_z)$ for the bin-4 and bin-21 (in shear layer) along with large deviation in the tail region. While the tails of $P(\Omega_z)$ are super-Gaussian for $\beta = -0.99$ in all bins (Fig. 3.12(f)), they are super-Gaussian in the bulk region and sub-Gaussian near the walls for $\beta = 0$.

Fig. 3.15 presents the effects of dissipation on the velocity distribution functions for $\beta = 0$ for the middle bin ($bin = 13$). As before, $P(C_x)$, remains asymmetric for all e, Fig. 3.15(a). As expected, $P(C_y)$, $P(C_z)$, $P(\Omega_x)$ and $P(\Omega_y)$ distributions remain symmetric but tend towards Gaussian with increase in elasticty; however, there is still large deviation in the tail region. $P(\Omega_z)$ shows much higher deviation from Gaussian in the tails as well as in the low velocity region.

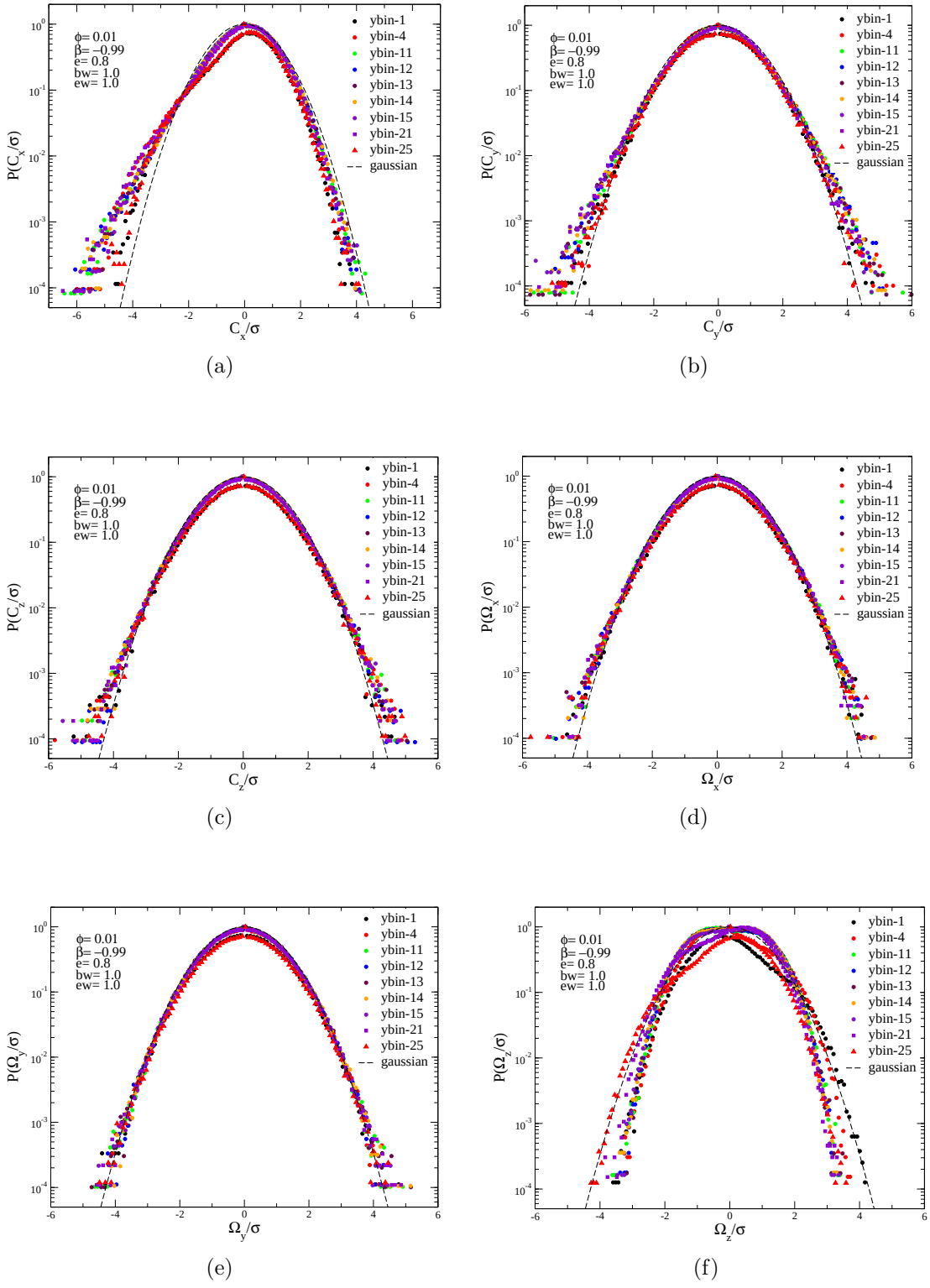

Figure 3.12: Binwise variation in velocity distribution function for nearly smooth particles (β=-0.99, e_p=0.8). Other parameters as in Fig. 3.2. (a) C_x, (b) C_y, (c) C_z, (d) Ω_x, (e) Ω_y and (f) Ω_z.

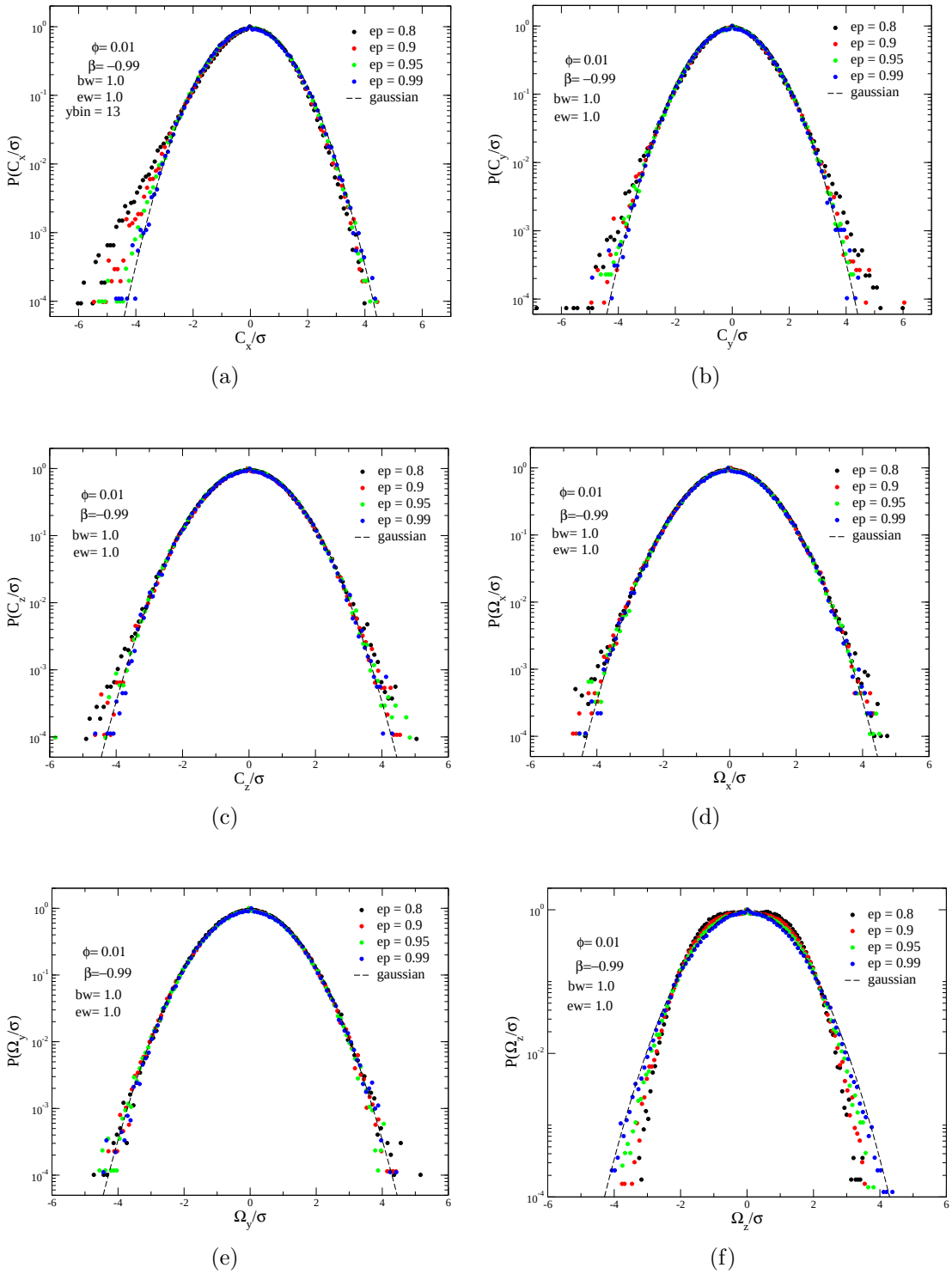

Figure 3.13: Effect of dissipation on velocity distribution functions for nearly smooth particles (β=-0.99) in bin = 13. Other parameters as in Fig. 3.2. (a) C_x, (b) C_y, (c) C_z, (d) Ω_x, (e) Ω_y and (f) Ω_z.

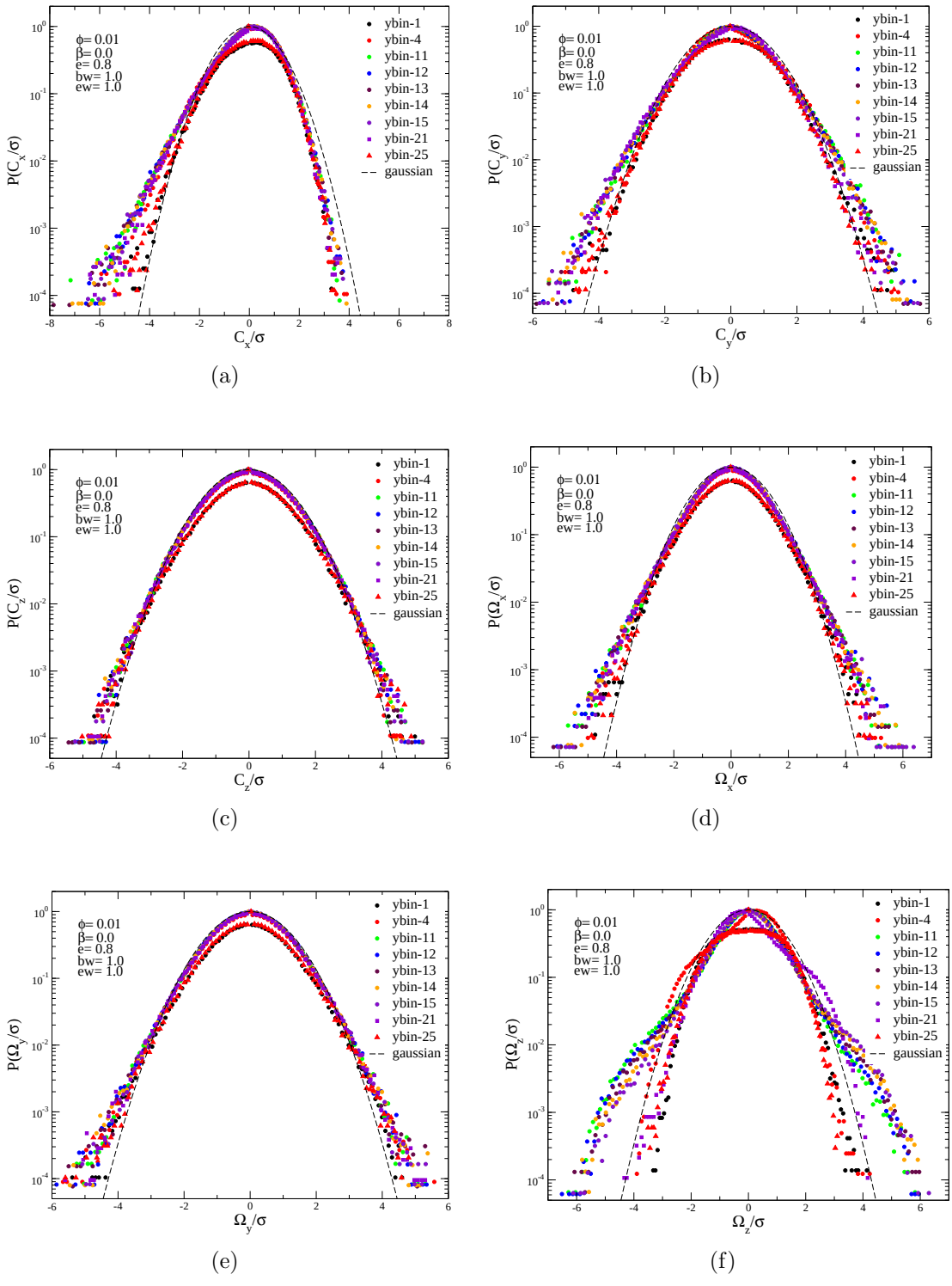

Figure 3.14: Binwise variation in velocity distribution function for rough particles (β=0, e=0.8). Other parameters as in Fig. 3.2. (a) C_x, (b) C_y, (c) C_z, (d) Ω_x, (e) Ω_y and (f) Ω_z.

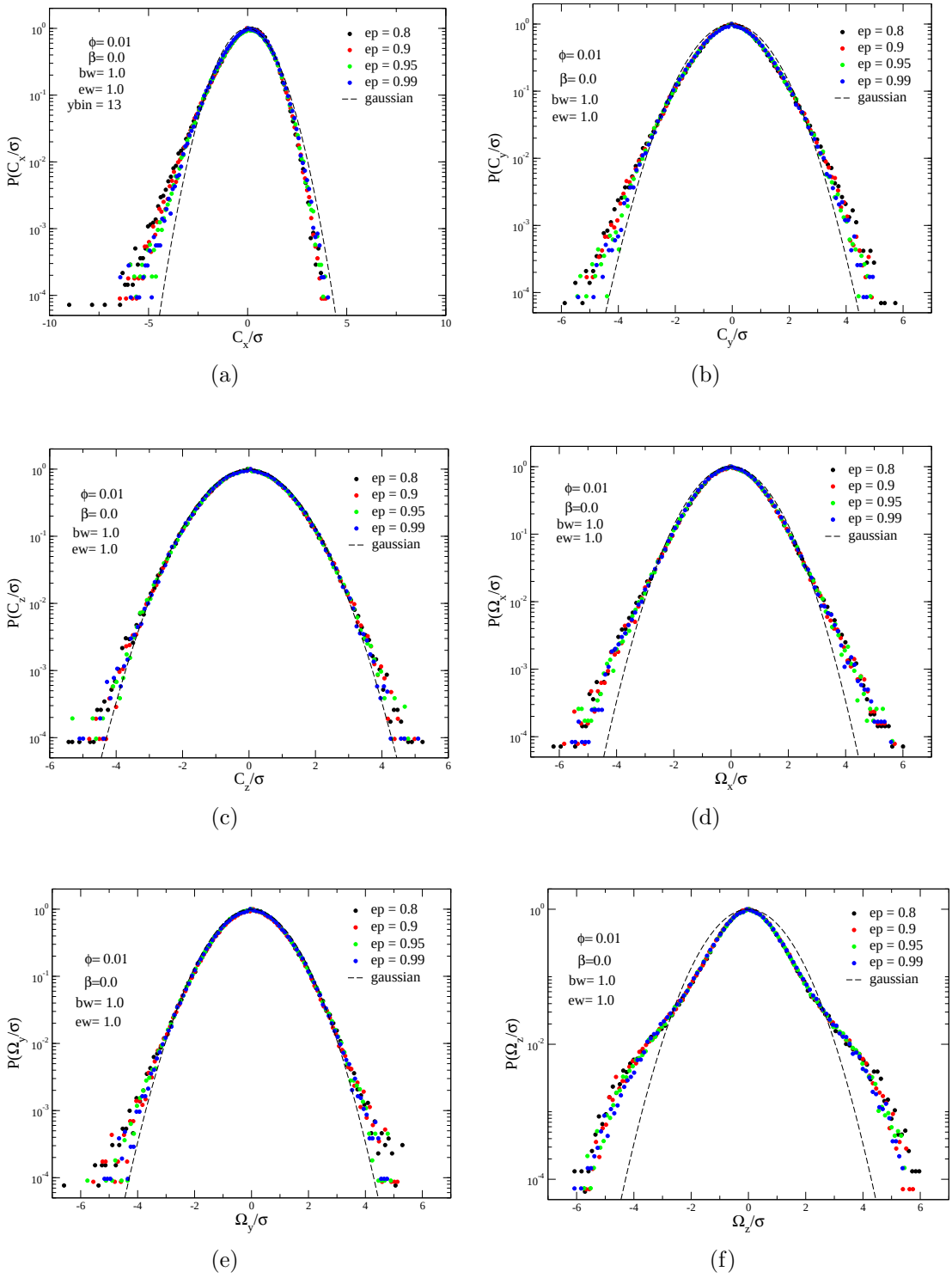

Figure 3.15: Effect of dissipation on velocity distribution functions for rough particles (β=0) in $bin = 13$. Other parameters as in Fig. 3.2. (a) C_x, (b) C_y, (c) C_z, (d) Ω_x, (e) Ω_y and (f) Ω_z.

Perfectly rough particles ($\beta \rightarrow 1$)

The local velocity distribution functions for $\beta = 0.99$ are shown in Fig. 3.16 for $e = 0.8$. Compared to two previous cases ($\beta = -0.99$ and $\beta = 0$) in Fig. 3.12 and Fig. 3.14, the degree of assymetry in $P(C_x)$ is relatively small. The effects of dissipation on all VDFs for $bin = 13$ is shown in Fig. 3.17. It is observed that all distribution functions approach Gaussian in the elastic limit ($e = 1$). This is an expected result for perfectly rough ($\beta \rightarrow 1$), elastic ($e \rightarrow 1$) particles with rough walls ($\beta_w \rightarrow 1$).

In contrast to our results for smooth particles ($\beta = -0.99$) with rough walls ($\beta_w = 1$) in Fig. 3.13, the present case of perfectly rough particles ($\beta = 0.99$) with rough walls ($\beta_w = 1$) leads to Gaussian VDFs for elastic particles ($e \rightarrow 1$). It is interesting to recall from Fig. 3.8 that the Knudsen number for all cases is larger than 0.1 ($Kn > 0.1$) that corresponds to the regime of transitional-flow (Karniadakis & Besok 2002). In the transitional flow regime of the granular Poiseuille flow that it appears that the Gaussian distribution could serve as a leading-order VDF.

Summary

From the above results we can conlude that the surface roughness of the particles has a major role to play in the deviation of velocity distribution functions from the Gaussian distribution in the dilute limit of granular Poiseuille flow. The deviation from Gaussian is pronounced at $\beta \sim 0$ for any value of normal restitution coefficient (even for e=0.99). This deviation starts decreasing if we move towards $\beta = \pm 1$.

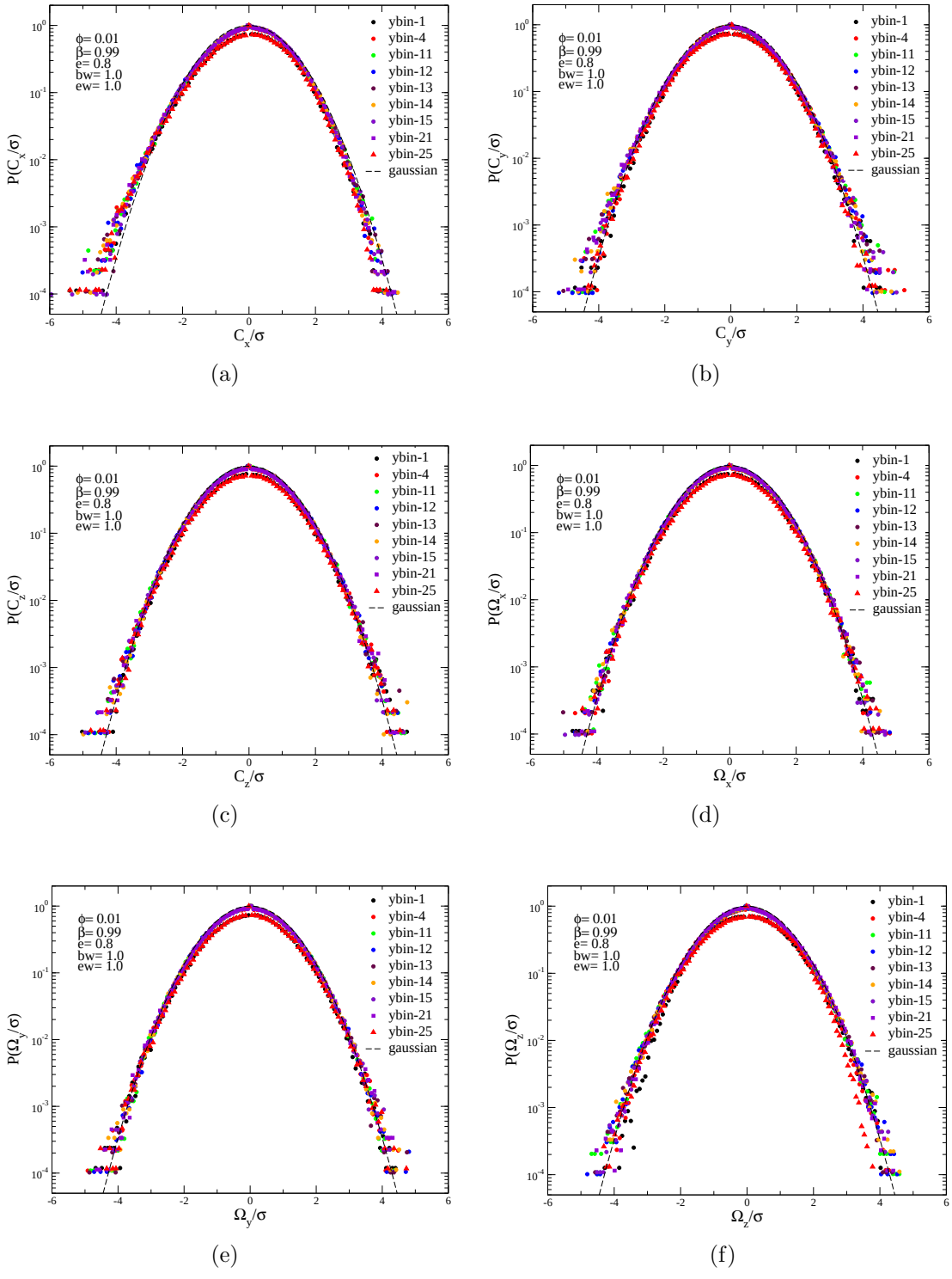

Figure 3.16: Binwise variation in velocity distribution function for perfectly rough particles (β=0.99, e=0.8). Other parameters as in Fig. 3.2. (a) C_x, (b) C_y, (c) C_z, (d) Ω_x, (e) Ω_y and (f) Ω_z.

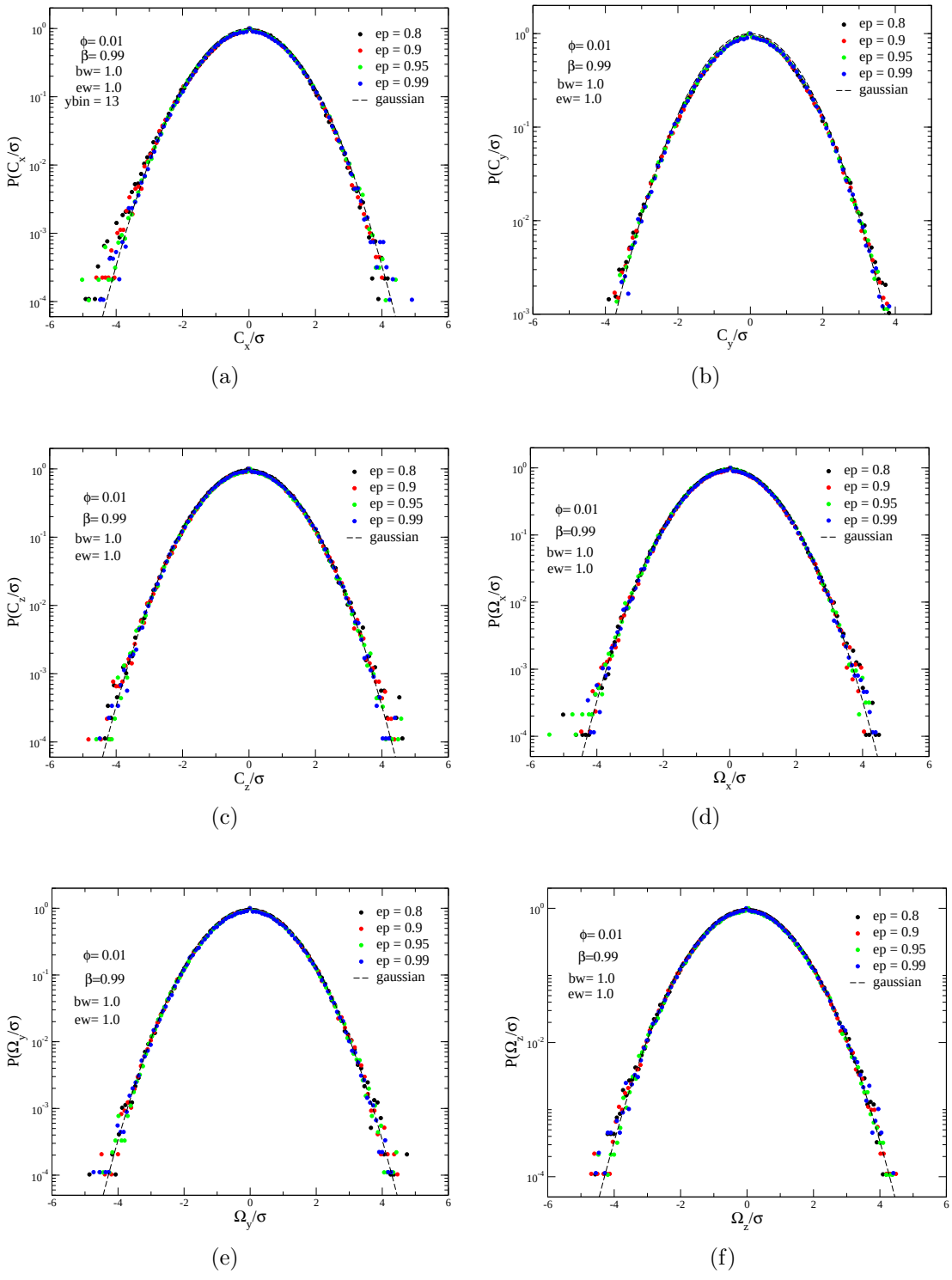

Figure 3.17: Effect of dissipation on velocity distribution functions for perfectly rough particles (β=0.99) in $bin = 13$. Other parameters as in Fig. 3.2. (a) C_x, (b) C_y, (c) C_z, (d) Ω_x, (e) Ω_y and (f) Ω_z.

3.3 Pair Correlation Function

The pair correlation function (g(r)) is defined as the probability of finding a particle at a distance r from a test particle. Thus $g(r)$ provides a measure of local spatial ordering of the particles. Since the mean field quantities vary along the y-direction, the pair-correlation would also vary with y. Hence $g(r) \equiv g(r, y_j)$ where y_j is the location of the j^{th} bin and the disrance "r" spans along (x,z)-plane over which we have periodec boundary conditions. The expression for binwise $g(r)$ is calculated from:

$$g(r) \equiv g(r, y_j) = \frac{2V_j}{N_j^2} \langle \sum_{i=1}^{N_j} \sum_{j>1}^{N_j} \delta(r - r_{ij}) \rangle,$$

where V_j is the volume of the j^{th} bin, N_j is the number of particles in the $j-th$ bin and the angular brackets indicates average over time.

We have calculated the binwise $g(r)$ by taking 25 bins across the width of the channel. Due to symmetry across the channel centerline, we present results for bin=1 (near the wall), bin=4 (in shear region) and bin=13 (middle of the channel). Fig. 3.18(a) shows the result for smooth particles, $\beta = -0.99$. It is observed that there is no significant difference in $g(r)$ for different bins. To know the effect of e on $g(r)$, we present results for bin=13 in Fig. 3.18(b). We can see from Fig. 3.18(b) that there is negligible density correlation for any value of e, i.e., it behaves like a gas.

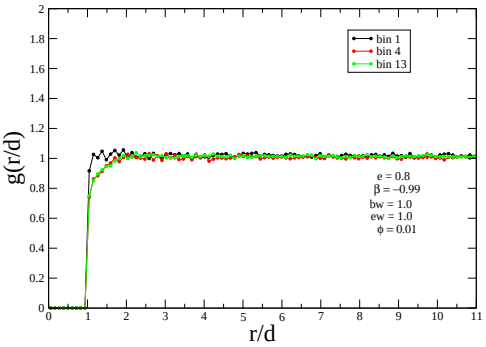

(a) Pair correlation function for different bins for e=0.8

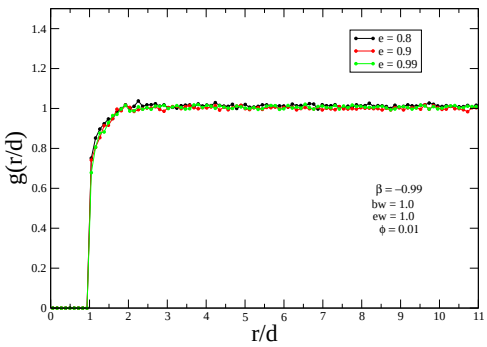

(b) Effect of e on pair correlation function for bin=13

Figure 3.18: Nearly smooth particles (β=-0.99). Other parameters as in Fig. 3.2

If we increase the particle surface roughness, $\beta = 0$, we still see no significant density correlation in any bin, Fig. 3.19(a). The inelastic ($e < 1$) dissipation has negligible effect on $g(r)$ even for $\beta = 0$.

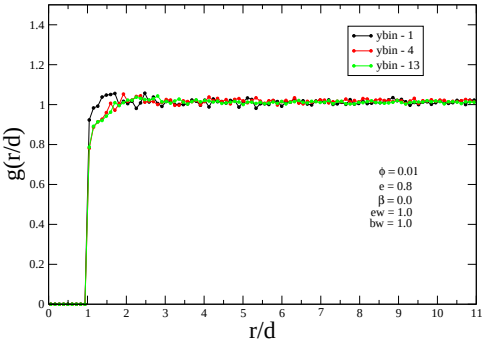

(a) Pair correlation function for different bins for e=0.8

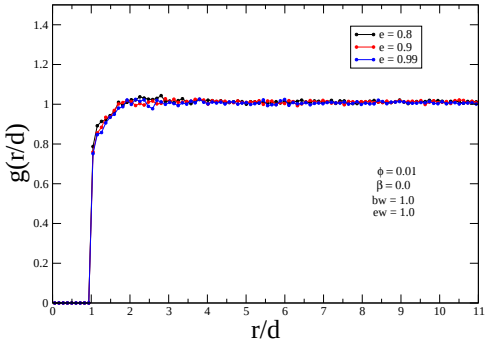

(b) Effect of e on pair correlation function for bin=13

Figure 3.19: Rough particles (β=0). Other parameters as in Fig. 3.2

Similarly, for perfectly rough particles, $\beta = 0.99$, no significant density correlation is visible in Fig. 3.20. We can thus conclude that in the dilute limit, the granular flow is behaving almost like a gas, without any density correlation irrespective of the value of particle roughness and dissipation level.

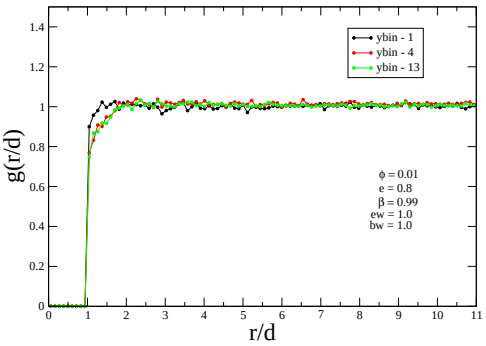

(a) Pair correlation function for different bins for e=0.8

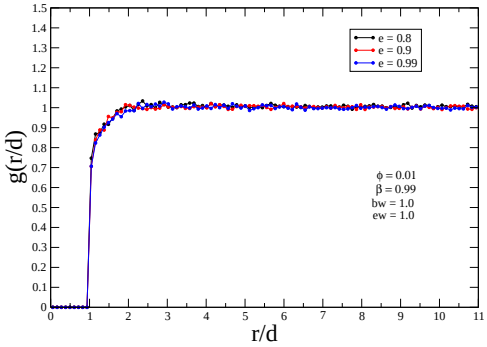

(b) Effect of e on pair correlation function for bin=13

Figure 3.20: Perfectly rough particles (β=0.99). Other parameters as in Fig. 3.2

3.4 Orientational Correlation Function

The translational and rotational fluctuating velocities are not "directionally" correlated in a molecular gas, but recently such an "orientational" correlation has been found in a freely cooling gas (Brilliantov *et al.* (2007)) as well as in granular shear flows (Gayen & Alam (2008)). The orientational correlation between translational and rotational velocities is quantified in terms of the mean square of the cosine of angle Ψ, between $\mathbf{C} = \mathbf{c} - <\mathbf{c}>$ and $\mathbf{\Omega} = \omega - <\omega>$:

$$\begin{aligned} \Lambda(y_j, t) &= \frac{1}{N_j}\sum_{i=1}^{N_j}\frac{(\mathbf{C_i}\cdot\mathbf{\Omega_i})^2}{(C_i^2\Omega_i^2)} = \frac{1}{N_j}\sum_{i=1}^{N_j} cos^2\Psi_i, \\ \Lambda(y) &= \langle\Lambda(y_j, t)\rangle, \end{aligned}$$

where y_j is the location of the j^{th} bin.

We present here the effect of dissipation and roughness on orientational correlation function (OCF) averaged over the simulation run for time $t = 70000$ collisions per particle. The *brown* vertical straight line in each panel of Fig. 3.21 corresponds to $<\Lambda> = 1/3$ which holds for a molecular gas (Brilliantov *et al.* (2007)).

Fig. 3.21(a) shows the binwise variation of average OCF, $\Lambda(y) =< \Lambda(y_j, t) >$, for different values of normal restitution coefficient (e) for smooth particles ($\beta = -0.99$). As expected, $\Lambda(y) > 1/3$ for every value of e, showing the presence of orientational correlation. With increase of e, $\Lambda(y)$ shifts towards the molecular gas limit of 1/3. The inset shows the variation of $\Lambda(0)$ (the value of Λ at the center of the channel) and the variation of mean Λ, averaged over all the bins, with dissipation e. The mean of $\Lambda(y)$ varies non-monotonically with dissipation but remains above 1/3 limit. It is also observed that $\Lambda(y)$ is lower in the middle region of the domain as compared to wall regions, i.e., the particles near the walls are more orientationally correlated to each other. The strong correlation in the smooth limit for inelastic particles is due to the one-way energy transfer from translational to rotational mode (Gayen & Alam (2008)). Since the particles are nearly smooth ($\beta = -0.99$), the translational velocities are the only way to transfer momentum during collision process.

Fig. 3.21(b) shows the variation of $\Lambda(y)$ for the case of rough particles ($\beta = 0$). For this case, because of additional rotational dissipation we see that $\Lambda < 1/3$ for all values of e. The value of $\Lambda(y)$ near the wall is much smaller than that in the

bulk, indicating molecular-gas like behaviour in the middle of the channel. The inset shows that both $\Lambda(0)$ and the mean of $\Lambda(y)$ approach 1/3 monotonically with decrease in inelasticity.

The results for almost perfectly rough particles ($\beta = 0.99$) are shown in Fig. 3.21(c). For this case, $\Lambda(y)$ for any value of e is less than 1/3. Since in this situation the rotational dissipation is negligible as compared to $\beta = 0$, the profiles are nearer to 1/3. Increasing elasticity also pushes $\Lambda(y)$ towards 1/3. The variation in the inset also indicates the increase of orientational correlation in the system with increase of inelasticity.

To summarize, we find significant orientational correlations for all three values of β in the Boltzmann limit of granular Poiseuille flow. Such orientational correlations are always neglected in the kinetic theory of rough granular gases (Goldhirsch *et al.* (2005); Brilliantov *et al.* (2007)). The present work indicates that orientational correlations should be incorporated in theoretical models of granular flows.

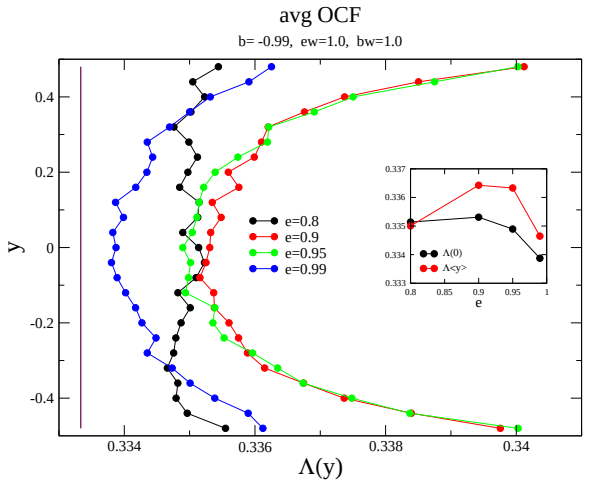

(a)

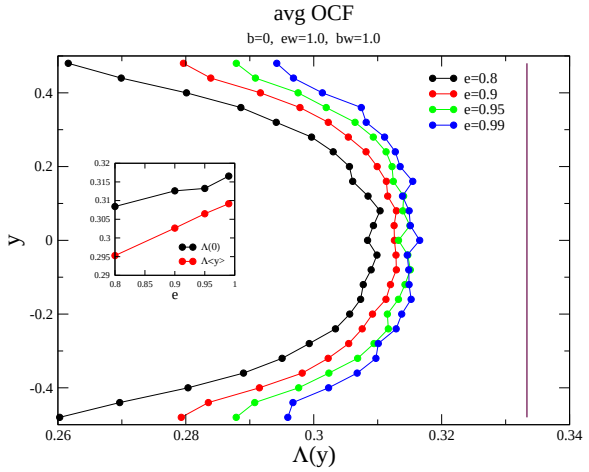

(b)

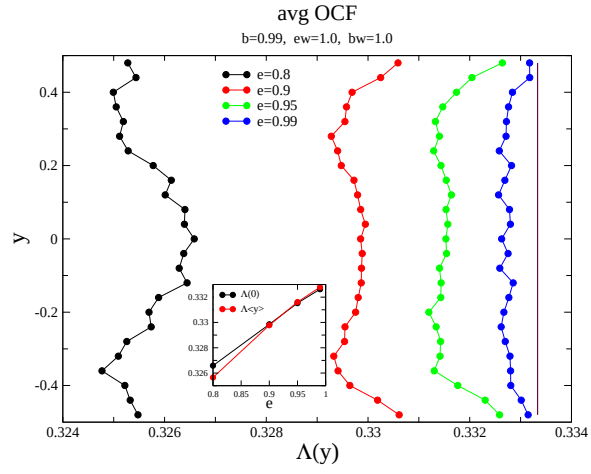

(c)

Figure 3.21: Effects of dissipation and roughness on orientational correlation. (a) Smooth particles $\beta = -0.99$, (b) rough particles $\beta = 0$ and (c) perfectly rough particles $\beta = 0.99$. Other parameters as in Fig. 3.2

CHAPTER 4

DENSE FLOWS

In this chapter the effects of density (particle volume fraction) on the mean field quantities, velocity distribution functions and various correlations is presented. The variation of system density has great impact in terms of not only the changes in the dynamics of flow, but also on various system properties, like local density distribution, orientational correlation, VDF, pair correlation and velocity correlation function.

The study begins with a moderately dense flow ($\phi = 0.1$) and then moving on to more dense flows at a relatively higher density ($\phi = 0.5$). In such cases with large number of particles, the dissipation gives rise to the formation of clusters which significantly affects system properties.

4.1 Moderately Dense Flows

In this section we discuss results on the moderately dense flow by fixing the sytem density at $\phi = 0.1$. The number of particles used in this simulation work is kept fixed to $N = 24400$ with equal domain dimensions in all the three directions such that L/d=50, W/d=50, H/d=50. The wall properties are fixed by specifying the restitution coefficients for wall-particle collisions, i.e. $e_w = 1$ and $\beta_w = 1$. Note that the value of $\beta_w = 1$ correspond to a rough wall.

Mean field quantities

This section presents the effect of roughness and dissipation on the mean field quantities like mean volume fraction (ϕ), mean linear velocity (U_x), mean rotational velocity (ω_z), translational granular temperature (T) and rotational granular temperature (θ). The macroscopic quantities are presented here using *binwise* averaging method and are non-dimensionalized as mentioned in Chapter-2.

Smooth particles ($\beta \to -1$)

First we present results for nearly smooth particles, $\beta = -0.99$. Typical snapshots in different planes for $e = 0.7$ are shown in Fig. 4.1(a) and Fig. 4.1(b). The dissipation in the system resulted in the formation of local clusters in the form of density waves, clearly visible in the snapshot, in the xy-plane. There is small density variation in xz- and yz-planes too. Looking at the energy vs time plot in Fig. 4.1(c), we see that the system is in steady state and these waves do not change their structure with time. A detailed study of such density waves is considered in chapter 5.

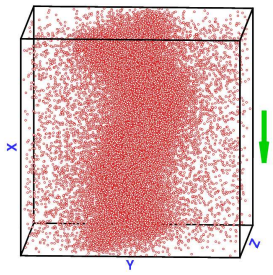

(a) Particle positions (xy-plane)

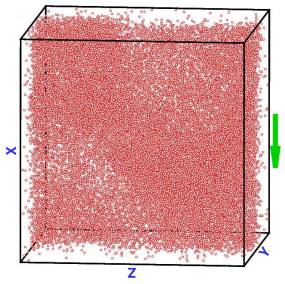

(b) Particle positions (xz-plane)

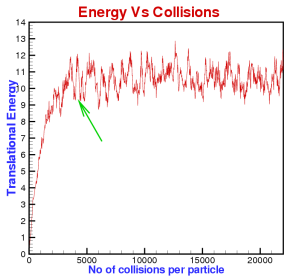

(c) Time trace of average kinetic energy

Figure 4.1: Nearly smooth particles ($\beta = -0.99$) with $e = 0.7$. N=24400, L/d=50, W/d=50, H/d=50, ϕ=0.1, e_w=1.0, β_w=1.0

There is significant variation of mean local density across the channel width with increasing dissipation, verifying the dense plug as shown in Fig. 4.2(a) since as the dissipation is increased the particles shift towards the center. The translational velocity profile (U_x) in Fig. 4.2(b) differs from the parabolic profile with significant slip at walls. The translational temperature across the channel width shows a minima at the channel centreline, Fig. 4.2(d). However, the rotational temperature profile has a non-monotonic profile as visible in Fig. 4.2(e) which approaches a more uniform profile with decrease in dissipation. The shape of each profile indicates the presence of a plug even with very less dissipation at $e = 0.99$, which just intensifies as the dissipation is increased.

Fig. 4.2(f) shows the effects of e on the Knudsen number ($Kn = \lambda/W$) where λ is the mean free path and W is the channel width. We see that the profile for $e = 0.99$ corresponds to lower values of Kn. Since at higher energy states ($e \sim 1$), the

agitation of particles is more the collision frequency increase resulting in smaller λ. For higher dissipation there is a minima at the channel centreline, contrary to what we observed in dilute flows ($\phi = 0.01$), and this minimum decreases with increase in dissipation. This can be explained as since we have dense cluster formation around the channel-center, which further intensifies with increasing dissipation, the particles are very closer to each other and hence the collision frequency is much higher at the center and λ is much smaller in the cluster region resulting in the minima at the center.

From the profiles of U_x and ω_z in Fig. 4.2(b) and Fig. 4.2(c), it is seen that the normal restitution coefficient has significant effect on the slip velocity at the walls as observed earlier for ϕ=0.01, and it increases with dissipation. The gradients in linear and rotational velocity at the wall too increase with dissipation (not shown here). There is temperature jump at the walls just like molecular gases, that too increases with dissipation. Since at higher dissipations, we have more particles shifting towards the centreline (plug formation), the few particles near the walls have higher fluctuating velocities , resulting in fewer collisions with the wall and consequently less loss of energy.

Rough particles ($\beta = 0$)

Here we consider rough particles with $\beta = 0$ for which the post-collisional tangential velocity vanishes. Typical snapshots in different planes for $e = 0.7$ are shown in Fig. 4.3(a) and Fig. 4.3(b). The dissipation induced density plug in the system is clearly visible in the xy-plane. From the energy vs time plot in Fig. 4.3(c), we can see that the system is in steady state and the plug in Fig. 4.3(a) persists with time.

Since there is additional dissipation of rotational energy because of $\beta = 0$, we have a dense plug even for nearly elastic collisions, i.e. the dissipation due to surface roughness is more pronounced in comparison to inelasticty, as can be seen in Fig. 4.4(a). The translational velocity profile, Fig. 4.4(b), has higher gradients in the *shear* region since the plug is more intense. Fig. 4.4(c) shows that the plug is dense enough to resist particle rotations and hence the particles have small rotational velocity in the plug region. The translational temperature across the channel width shows a minima at the channel centreline, Fig. 4.4(d) for all e. The rotational temperature profile, Fig. 4.4(e), has a minimum over the entire plug

region.

The Knudsen number profile in Fig. 4.4(f) shows the effects of e. There is a minima at the centreline except for $e = 0.99$. Kn in the plug region decreases with increasing dissipation and for e=0.7 it is extremely low in the plug region since the particles are too close to each other and hence λ is very small.

From the profiles of U_x and ω_z, we can see the effect of e on the slip velocity at the wall. The slip velocity as well as the gradients at the walls increase with dissipation. The temperature jump at the walls also exists which increases with dissipation.

Perfectly rough particles ($\beta \to 1$)

Now we study the effects of surface roughness that is large enough to reverse the spin of the particles. For this, we fix the value of particle roughness to $\beta = 0.99$ that corresponds to almost perfectly rough particles. The snapshots in Fig. 4.5(a) and Fig. 4.5(b) in the xy- and xz-planes for $e = 0.7$ show the presence of dissipation induced denisty wave of S-shape. From the energy vs time plot in Fig. 4.5(c), we can see that the system is in steady state.

For nearly elastic collisions ($e = 0.99$) the plug is more diffused (compared to $\beta = 0$) over the width of the channel as can be seen in Fig. 4.6(a). The translational velocity profile in Fig. 4.6(b) shows that the velocity magnitude for all e is decreased compared to the case of $\beta = 0$. Fig. 4.6(c) shows that the effect of plug on particle rotations is felt over the entire width of the channel and hence the particles have negligible rotational velocity over the entire width. The rotational temperature profiles in Fig. 4.6(e) show similar behaviour like that of translational temperature.

The Knudsen number profile in Fig. 4.6(f) shows that for $e = 0.99$, the Knudsen number is maximum at the channel centreline. For all other values of e, we see a minima at the centreline, and this minima increases with increasing dissipation.

4.1.1 Velocity Distribution Function

Here we study the effects of particle roughness and dissipation on velocity distribution functions (VDF) for the granular Poiseuile flow in the moderately dense limit ($\phi = 0.1$). We start the discussion from the smooth limit $\beta = -0.99$ and

move towards perfectly rough particles $\beta = 0.99$. The channel width is 50 particle diameters and divided into 25 bins. Since the flow is symmetric around the channel centerline and the asymmetries in VDF (if any) are observed to be opposite to each other on both sides of the centerline, the results are shown here only for three bins, $bin = 1$ near the wall, $bin = 4$ in the shear region and $bin = 13$ in the dense plug region.

Smooth particles ($\beta \to -1$)

Fig. 4.7 show results for nearly smooth particles ($\beta = -0.99$) for four values of e. Considering the streamwise translational velocity C_x, we see that there is asymmetric deviation from the Gaussian towards negative side near the wall ($bin = 1$) as well as in the shear region ($bin = 4$). However, the particles deviate significantly in the *plug* region ($bin = 13$), see Fig. 4.7(a). The VDF of spanwise translational velocity C_y , shown in Fig. 4.7(b), is almost Gaussian near the wall and in shear region (with negligible asymmetry) but the middle region ($bin = 13$), though symmetric, has significant deviation from a Gaussian distribution. Similar symmetric deviations are observed for C_z in Fig. 4.7(c) and Ω_y in Fig. 4.7(e).

However, the probability distribution function of Ω_x shows considerable deviations from a Gaussian near the low velocity region as well. The VDF for Ω_z shows interesting deviation in Fig. 4.7(f) especially near the low velocity region which increases with dissipation (e). The double-peak deviations near the low-velocity region in the shear region ($bin = 4$) are also observed. It is observed that the deviations in all these cases are strongly affected by dissipation (e) and increase with increasing dissipation.

From the main panels of Fig. 4.7 (a)-(c), we observe that the VDFs of C_x, C_y and C_z at the channel centreline ($bin = 13$) approach a Gaussian distribution in the limit of elastic collisions ($e \to 1$). In contrast, however, the VDFs of Ω_x, Ω_y and Ω_z deviate from a Gaussian even in the elastic limit ($e \to 1$). The latter observation could be a consequence of "rough" walls ($\beta_w = 1$).

Rough particles ($\beta = 0$)

Here we present results for rough particles ($\beta = 0$). Fig. 4.8(a) shows the VDF for streamwise translational velocity C_x which is asymmetric in the shear region ($bin = 4$) as well as in *plug* region ($bin = 13$) and near the wall ($bin = 1$).

The asymmetry is absent for C_y (except in $bin = 4$) but the deviation from a Gaussian is present in significant amount in the *plug* region, see Fig. 4.8(b). Similar observations can be made for C_z, see Fig. 4.8(c). An interesting observation about the VDFs for all velocities near the wall ($bin = 1$) is that though the VDF is symmetric and Gaussian near the tail region, there is deviation in the low-velocity region which increases with decrease in elasticity.

The VDFs of Ω_x and Ω_y are symmetric in all bins, see Fig. 4.8(d) and Fig. 4.8(e). The VDF of Ω_z is asymmetric in $bin = 1$ and $bin = 4$. Near the wall, the tail of $P(\Omega_z)$ follows a super-Gaussian whereas in the shear region there is interesting negative asymmetry. In the *plug* region, there is large deviation with highly stretched tails. It is observed that increasing dissipation due to surface roughness with $\beta = 0$ has resulted in increased deviations from the Gaussian distribution.

Perfectly rough particles ($\beta \to 1$)

The results for perfectly rough particles with $\beta = 0.99$ are presented in Fig. 4.9. The results for $P(C_x)$, $P(C_y)$ and $P(C_z)$ are similar to those for smooth particles ($\beta = -0.99$) in Fig. 4.7. However, the VDFs of rotational velocities differ significantly from those for $\beta = -0.99$. In particular, the VDFs of Ω_x, Ω_y and Ω_z approach Gaussian distribution in the limit of elastic collisions ($e \to 1$).

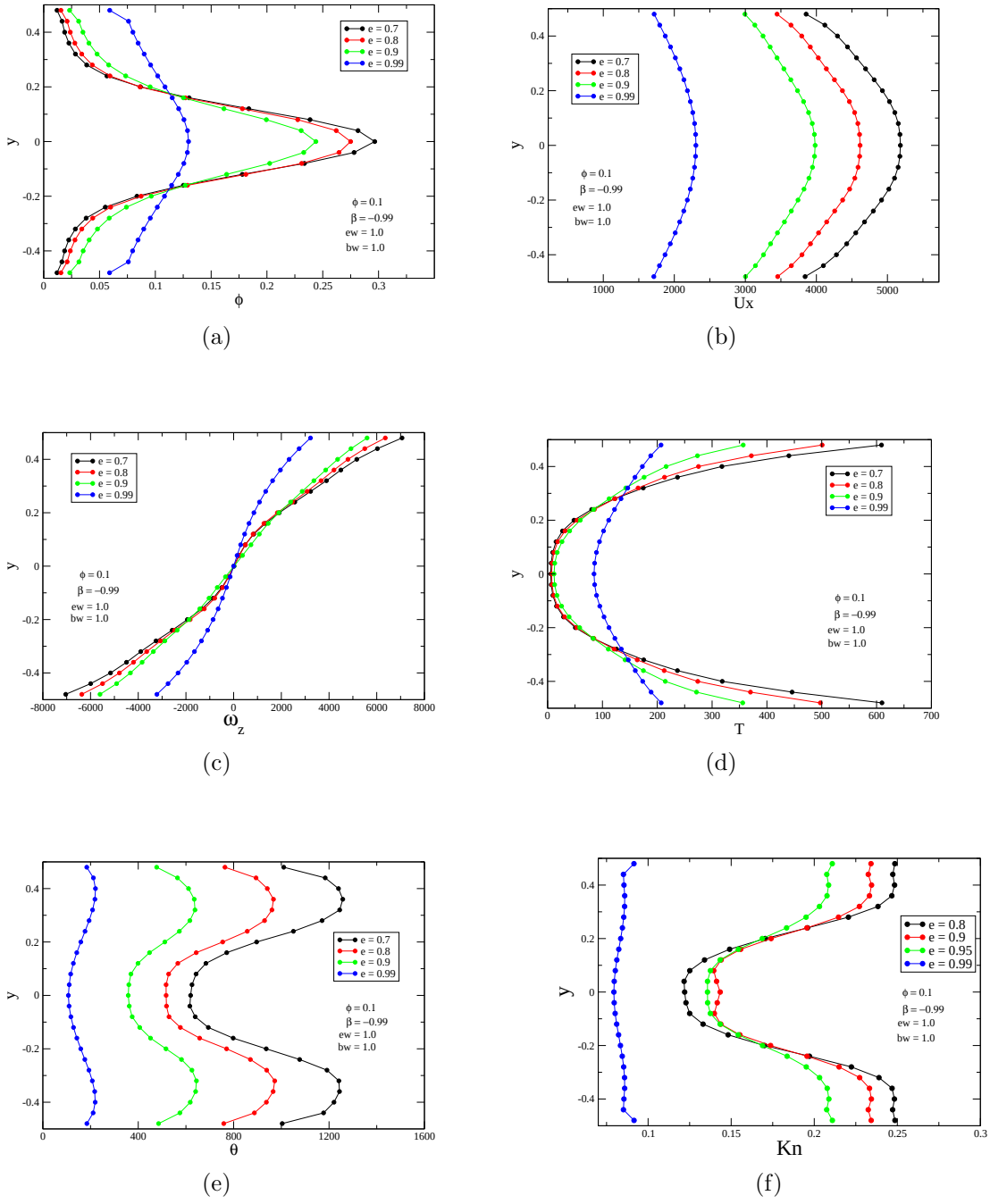

Figure 4.2: Effect of dissipation on mean field quantities for nearly smooth particles ($\beta = -0.99$). (a) Mean Volume fraction, (b) Mean translational velocity (U_x), (c)Mean rotational velocity (ω_z), (d) Translational granular temperature (T), (e)Rotational granular temperature (θ) and (f) Effect of e on Knudsen number. Other parameters as in Fig. 4.1

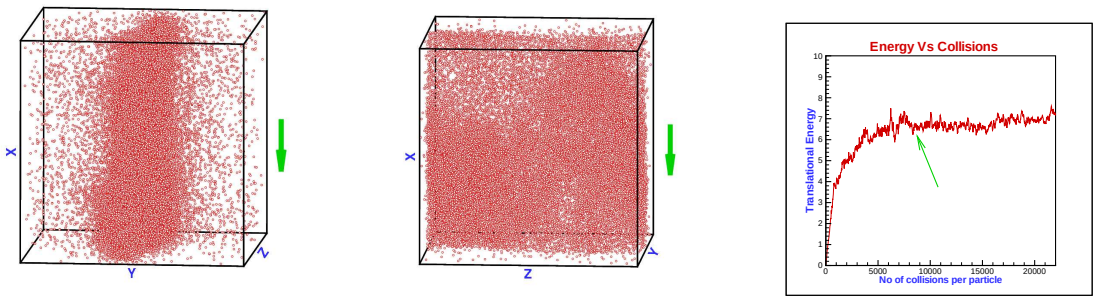

(a) Particle positions (xy-plane)

(b) Particle positions (xz-plane)

(c) Time trace of average kinetic energy

Figure 4.3: Rough particles ($\beta = 0$). Other parameters as in Fig. 4.1

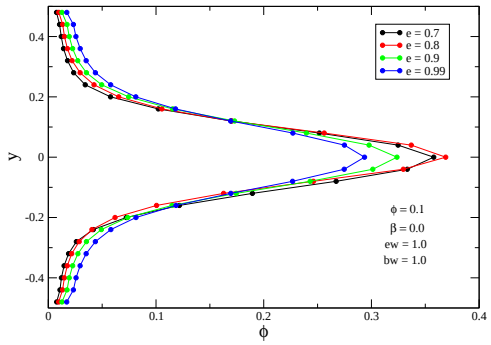

(a) Mean Volume fraction

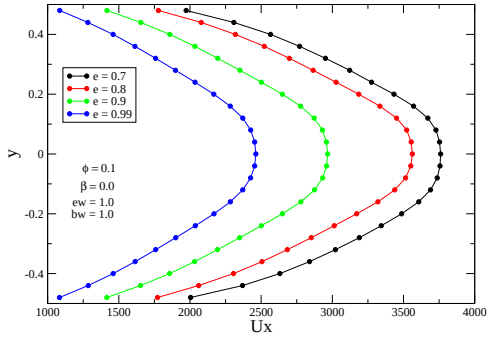

(b) Mean linear velocity (U_x)

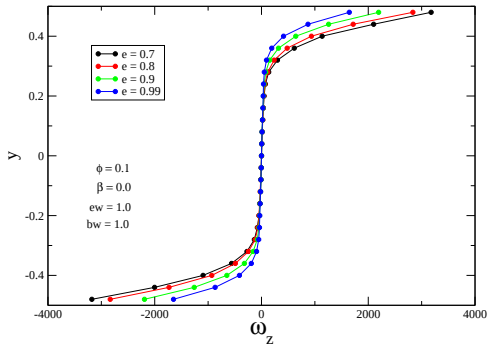

(c) Mean rotational velocity (W_z)

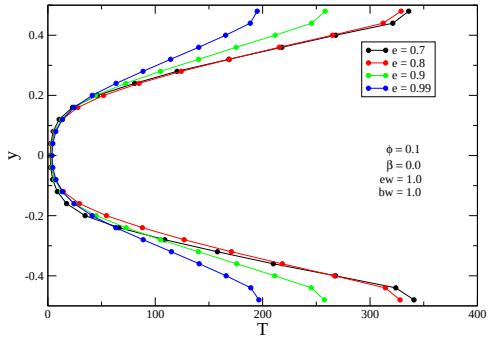

(d) Translational granular temperature (T)

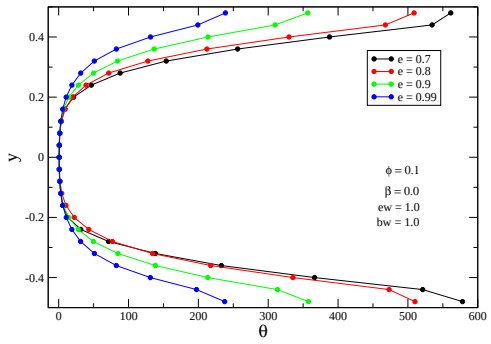

(e) Rotational granular temperature (θ)

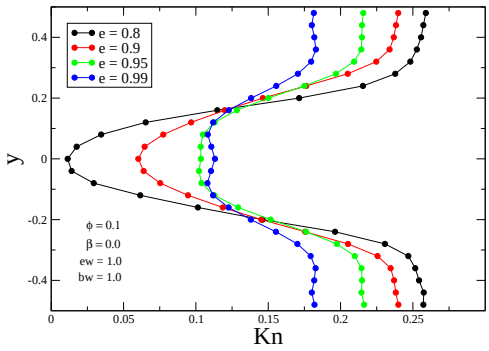

(f) Effect of e on Knudsen number

Figure 4.4: Effect of dissipation on mean field quantities for rough particles ($\beta = 0$). Other parameters as in Fig. 4.1

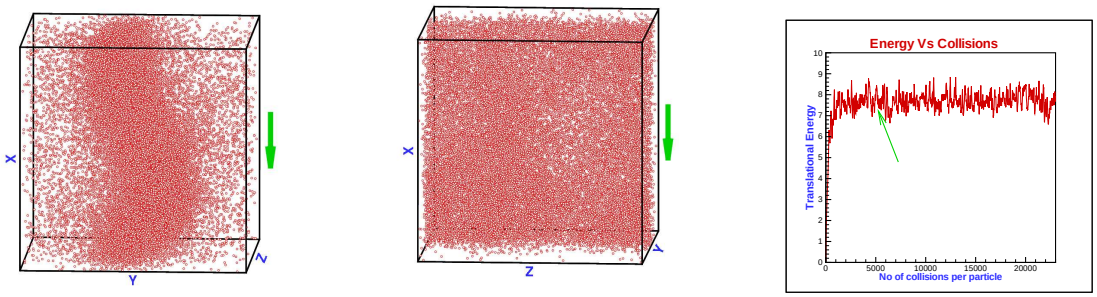

(a) Particle positions (xy-plane)

(b) Particle positions (xz-plane)

(c) Time trace of average kinetic energy

Figure 4.5: Perfectly rough particles ($\beta = 0.99$). Other parameters as in Fig. 4.1

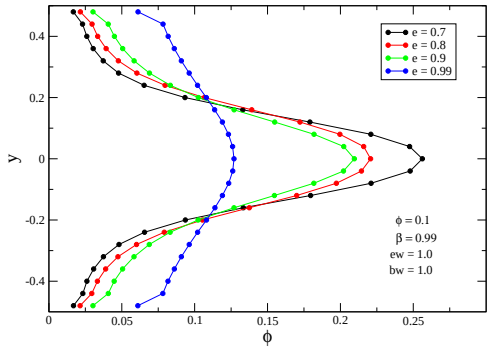

(a) Mean Volume fraction

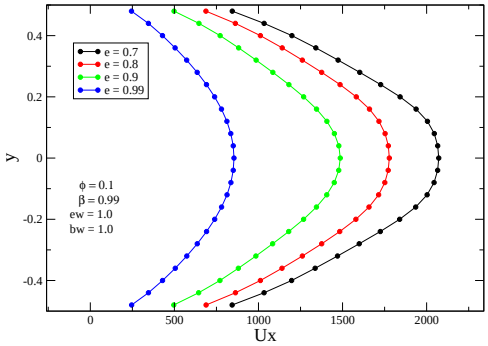

(b) Mean linear velocity (U_x)

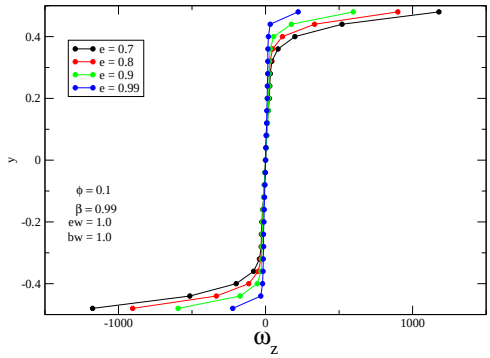

(c) Mean rotational velocity (W_z)

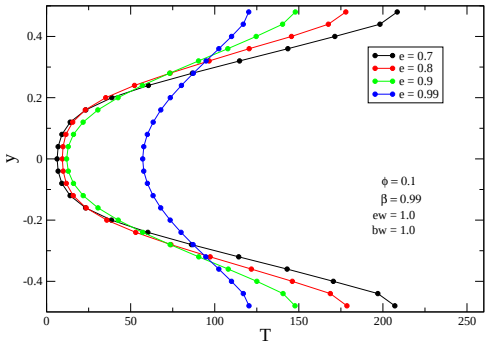

(d) Translational granular temperature (T)

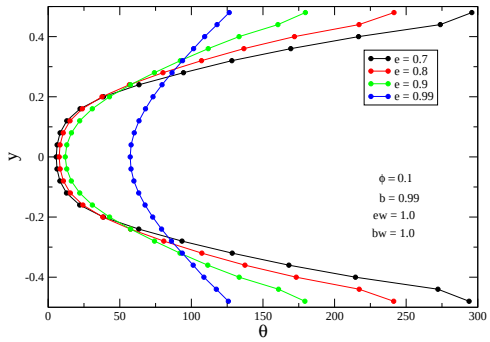

(e) Rotational granular temperature (θ)

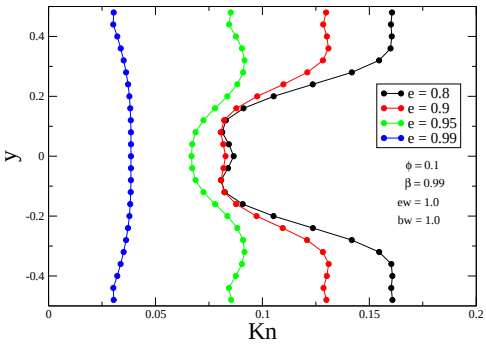

(f) Effect of e on Knudsen number

Figure 4.6: Effect of dissipation on mean field quantities for perfectly rough particles ($\beta = 0.99$). Other parameters as in Fig. 4.1

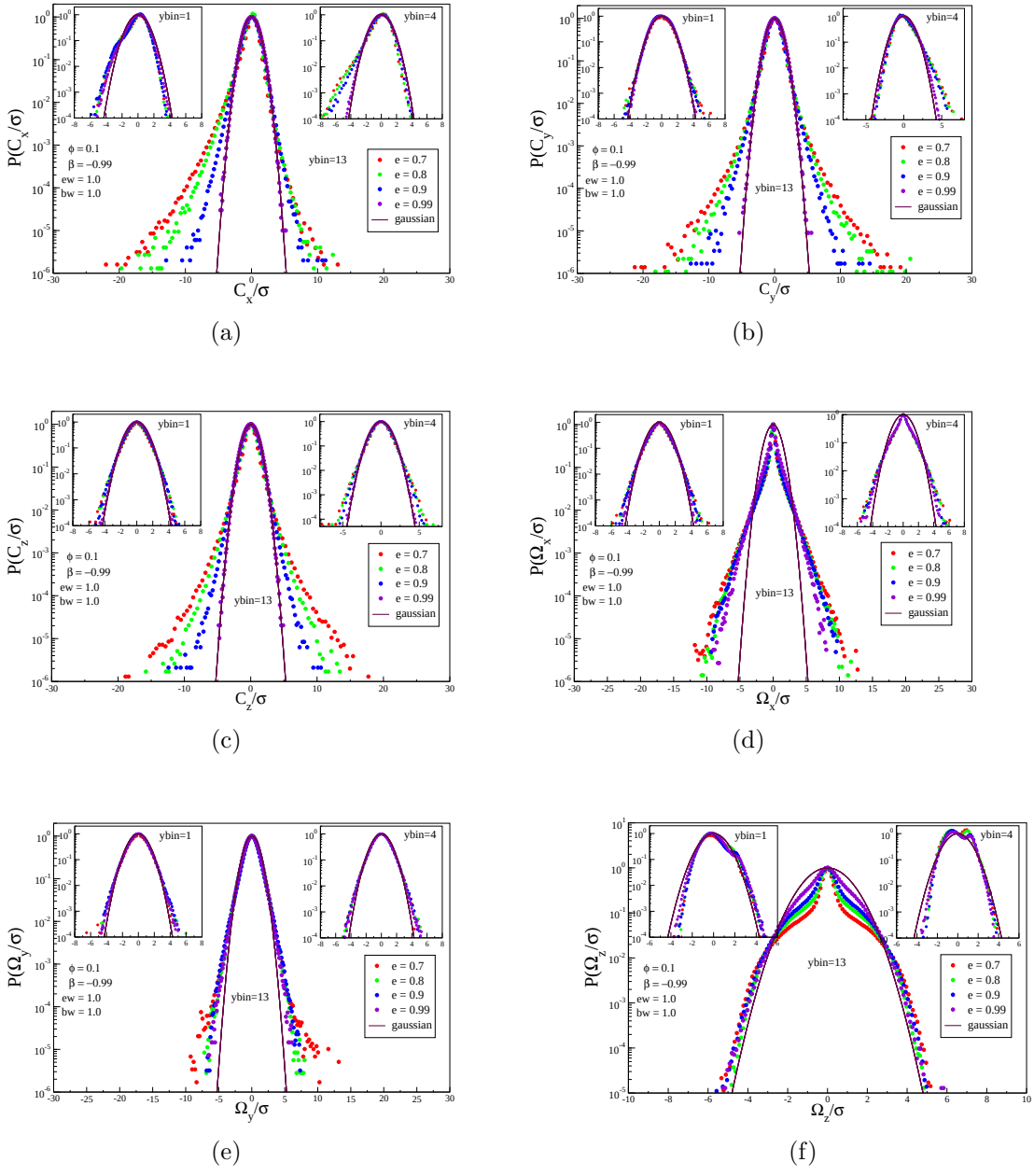

Figure 4.7: Effect of dissipation on velocity distribution functions for nearly smooth particles ($\beta = -0.99$). Other parameters as in Fig. 4.1. (a) C_x, (b) C_y, (c) C_z, (d) Ω_x, (e) Ω_y and (f) Ω_z

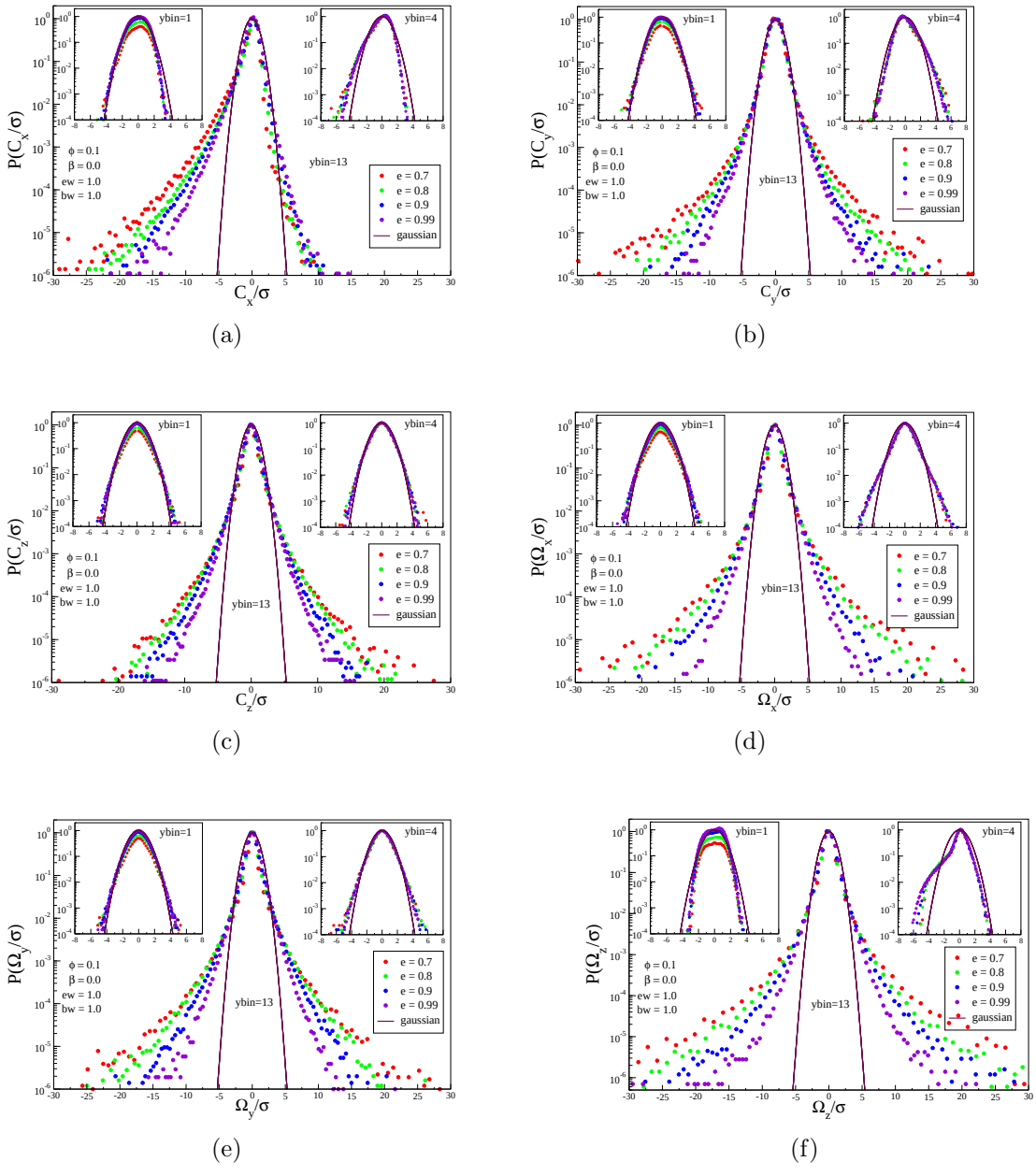

Figure 4.8: Effect of dissipation on velocity distribution functions for rough particles ($\beta = 0$). Other parameters as in Fig. 4.1. (a) C_x, (b) C_y, (c) C_z, (d) Ω_x, (e) Ω_y and (f) Ω_z

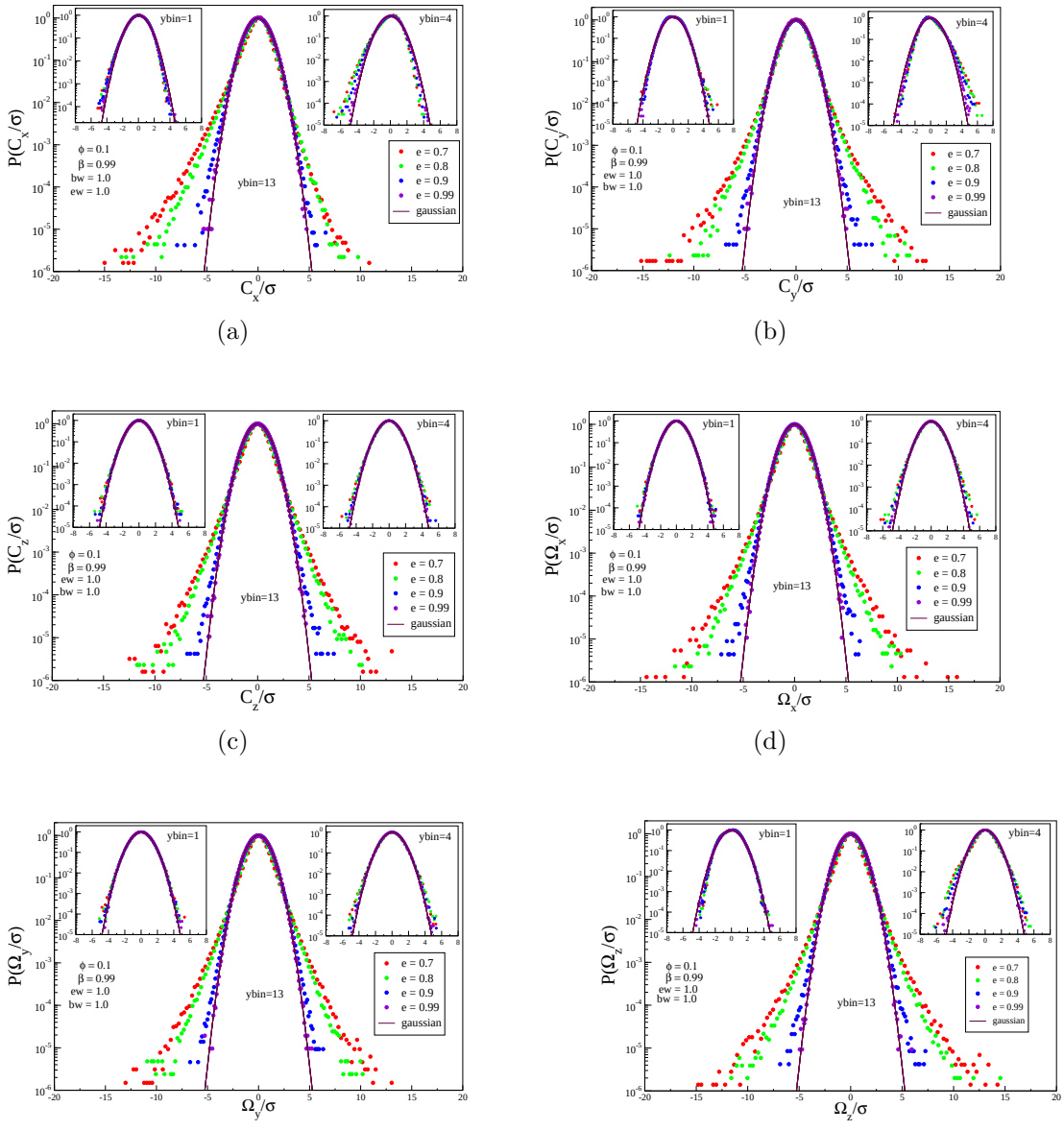

Figure 4.9: Effect of dissipation on velocity distribution functions for perfectly rough particles ($\beta = 0.99$). Other parameters as in Fig. 4.1. (a) C_x, (b) C_y, (c) C_z, (d) Ω_x, (e) Ω_y and (f) Ω_z

4.1.2 Pair Correlation Function

We have seen the presence of density inhomogeneities in the form of density waves and clusters in our simulations for $\phi = 0.1$. Hence we expect a significant amount of probability of finding a neighbour at a distance r from a test particle. Fig. 4.10 presents the pair correlation function ($g(r)$) observed in this moderately dense granular flow for the *plug* region ($bin = 13$); other bins are having very less number of particles and hence negligible pair correlation there.

Figure 4.10: Effect of dissipation on pair correlation function. Other parameters as in Fig. 4.1.

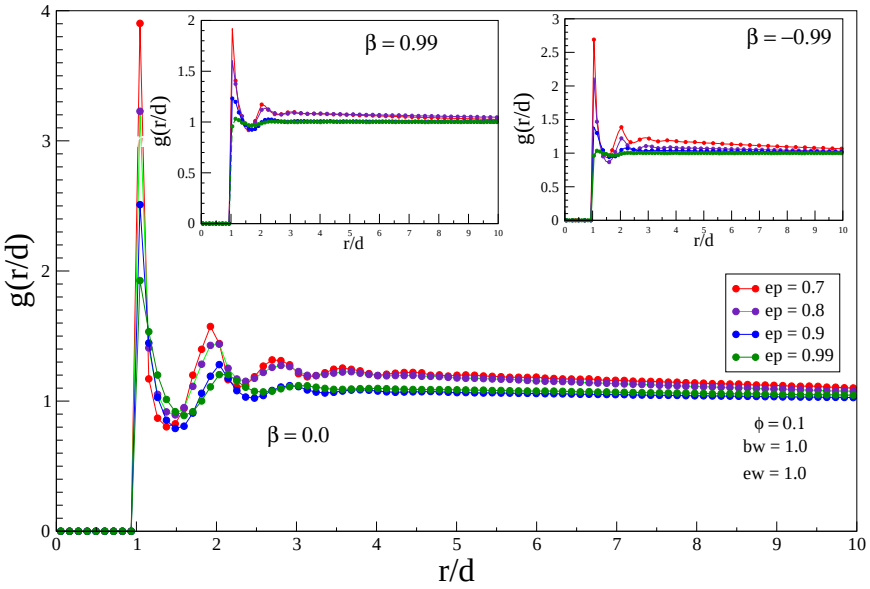

The main panel in Fig. 4.10 shows the pair correlation function (PCF) for rough particles ($\beta = 0$). It has a liquid-like structure since the particles are flowing in a density-wave like structure. There are peaks at r/d=2 and 3, indicating that the particles are closely arranged locally. However, there are no peaks at higher r/d, indicating the absence of long range ordering in the system. The left inset in Fig. 4.10 shows the PCF for $\beta = 0.99$ and the right inset for the smooth limit $\beta = -0.99$. In either case, there is no long range order for $e \to 1$, but the local ordering appears (peak at r/d=2) with increasing dissipation.

4.1.3 Orientational Correlation Function

Here we discusse the effects of dissipation and roughness on the orientational correlation function (OCF). The results presented in Fig. 4.11 are binwise OCF averaged over the simulation run for time $t = 70000$ collisions per particle. The *brown* vertical straight line in each panel indicates the molecular gas limit of $\langle\Lambda\rangle = 1/3$.

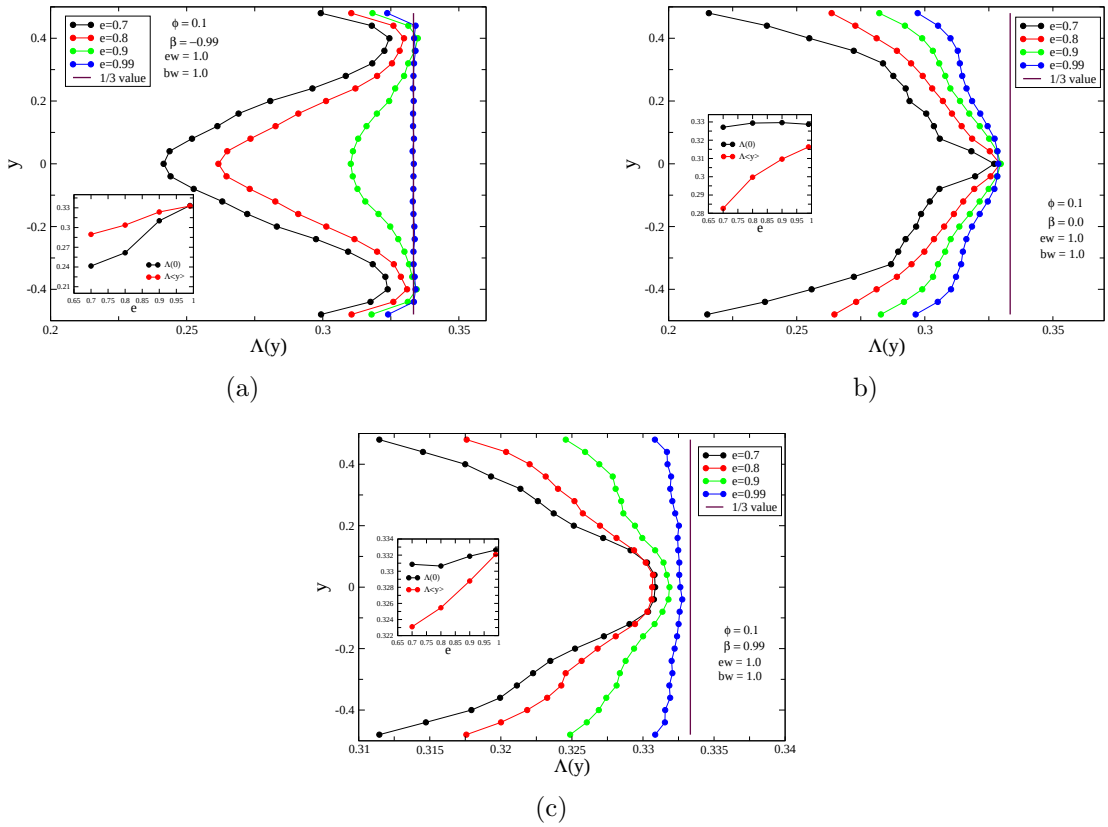

Figure 4.11: Effect of dissipation on average orientational correlation functions: (a)$\beta_p = -0.99$, (b)$\beta_p = 0.0$ and (c)$\beta_p = 0.99$. Other parameters as in Fig. 4.1

Fig. 4.11(a) shows the average OCF for smooth particles, $\beta = -0.99$. We see that there is strong correlation in the *plug* region which increases with dissipation. For $e = 0.99$ we see negligible correlation and the system behaves like a molecular gas ($\Lambda = 1/3$). The inset shows the variation of $\Lambda(0)$ and the mean of Λ with dissipation which decreases with dissipation. For rough particles, Fig. 4.11(b), is it is observed that there is negligible orientational correlation in the *plug* region.

As we have seen from the rotational velocity profiles that, since the particles are very closely packed in the form of cluster, there was negligible rotational velocities (Fig. 4.4(c)), we see negligible orientational correlation between translational and rotational velocities. On the other hand the particles near the wall and in the shear region are strongly correlated in direction. Fig. 4.11(c) shows the results for perfectly rough particles, $\beta = 0.99$. Here also we see weak orientational correlation in the middle dense region (which increases with dissipation) but significant correlation in the shear region and near the wall.

4.1.4 Velocity Correlation Function

In this section we focus on the effects of dissipation and roughness on spatial velocity correlation functions (VCF). Since the present work is in three dimensions, we have six linear velocity correlations and six rotational velocity correlations. The velocity correlations are calculated from:

$$C_{\alpha\beta}(r) = \frac{\left\langle \sum_{i=1}^{N} \sum_{j \geq i}^{N} c_\alpha^i c_\beta^j \delta(r - r_{ij}) \right\rangle}{\left\langle \sum_{i=j}^{N} c_\alpha^i c_\beta^j \right\rangle}, \tag{4.1}$$

where the subscripts α & β denote the coordinate directions whereas the superscripts i & j denote the particles; the angular brackets denote the averaging over time. In the following we present results only for translational velocity correlations.

First we present results for smooth particles, $\beta = -0.99$. Since for nearly elastic system ($e = 0.99$) the correlations are close to zero, we show results for binwise velocity correlations for $e = 0.7$, see Fig. 4.12. The streamwise translational velocity correlation C_{xx} is shown in Fig. 4.12(a). We see that due to the presence of *plug* in the middle region ($bin = 13$), there is strong correlation; on the other hand, because of very few particles near the wall and in shear region the correlations are nearly zero. Similar observation can be made for C_{yy} and C_{zz}. It is observed that the middle region has strong correlation for all cases. The cross-velocity correlations (C_{xy}, C_{xz} and C_{yz}) show significant correlation, again, in the dense *plug* region (not shown).

Fig. 4.13 shows the velocity correlations for the perfectly rough particles, $\beta =$

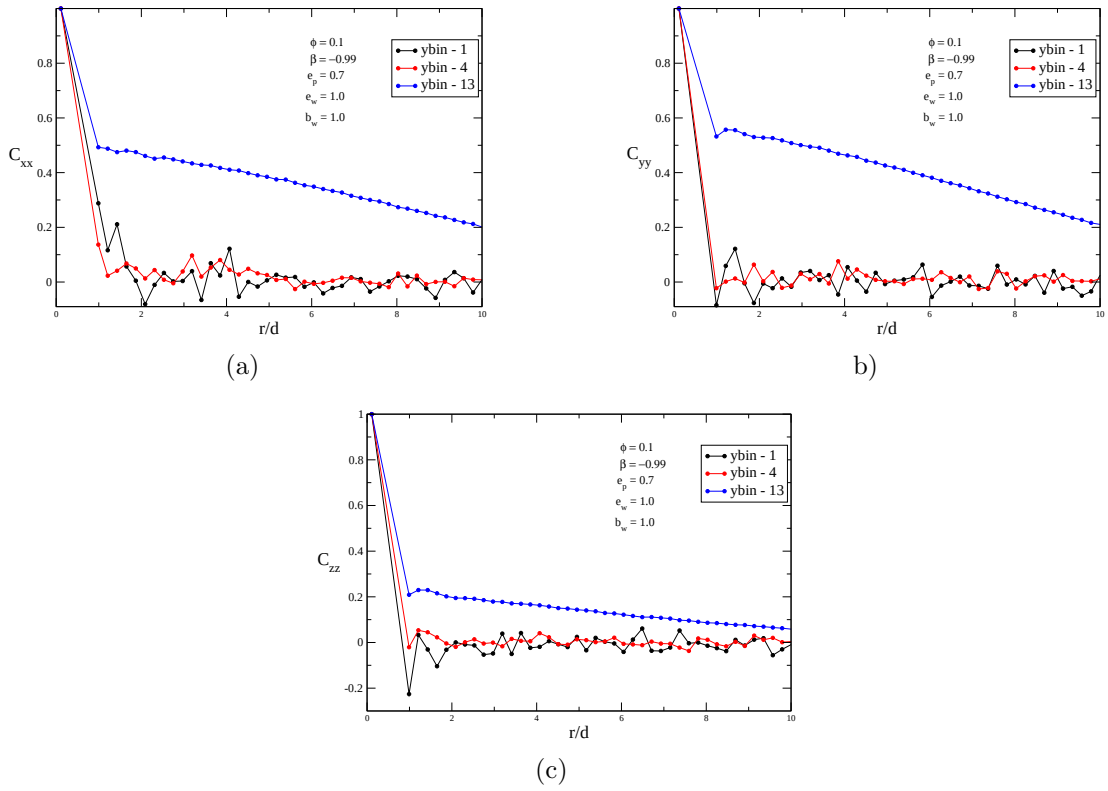

Figure 4.12: Velocity correlation functions for smooth particles ($\beta = -0.99$) with $e = 0.7$. (a)C_{xx}, (b)C_{yy} and (c)C_{zz}. Other parameters as in Fig. 4.1.

0.99. Here also, as expected, we see strong correltions along the channel centerline. However, the correlations are weak comparing to the smooth limit case.

As we have seen that there is significant amount of spatial velocity correlations in the dense region along the centerline, we will focus on this region for further study. Fig. 4.14 shows the overall summary of the effects of dissipation on velocity correlations. Fig. 4.14(a) shows that in the smooth limit, $\beta = -0.99$, the increase in inelasticity increases the correlation. The main panel shows correlation for C_{xx}, the left inset for C_{yy} and the right inset for C_{zz}. For all cases we see that the correlation is close to zero in the elastic limit ($e \to 1$).

The results for rough ($\beta = 0$) and perfectly rough particles are shown in Fig. 4.14(b) and Fig. 4.14(c), respectively. For any value of particle roughness, the spatial velocity correlations are largest for the streamwise velocity, and inelasticity enhances their magnitudes. For a given dissipation (fixed e), the magnitude of C_{xx} is the largest for rough particles ($\beta = 0$).

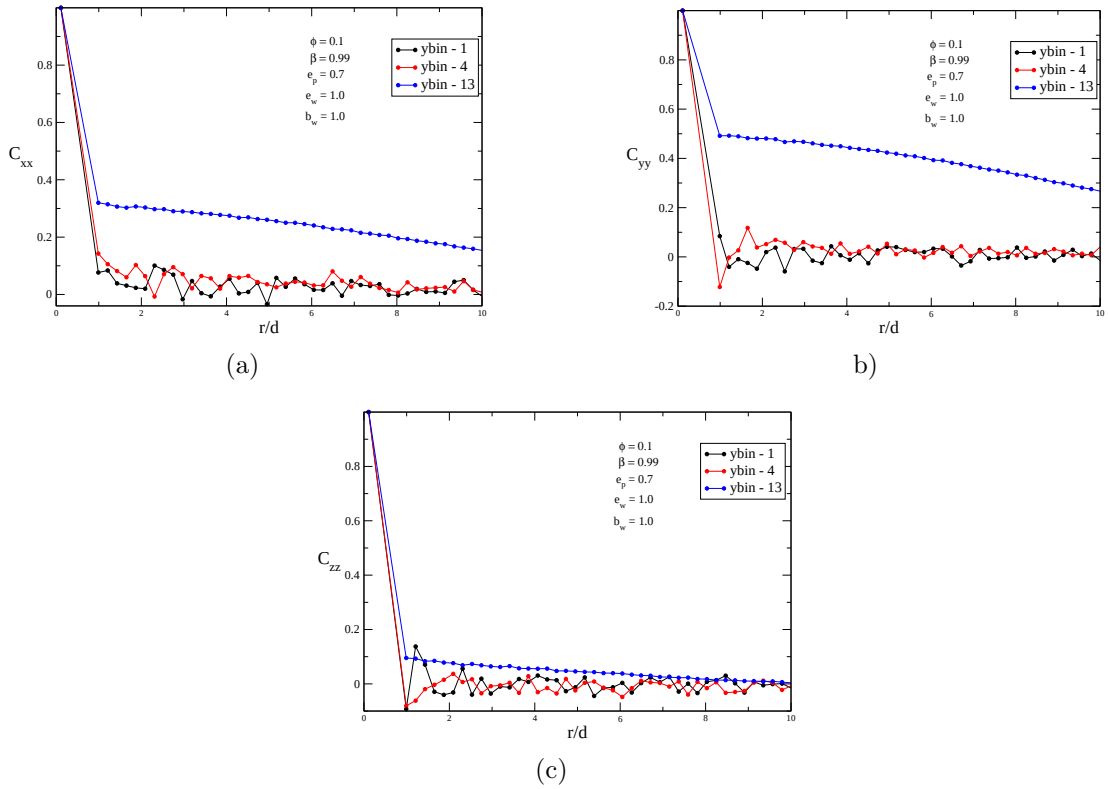

Figure 4.13: Velocity correlation functions for perfectly rough particles ($\beta = 0.99$) with $e = 0.7$. (a)C_{xx}, (b)C_{yy} and (c)C_{zz}. Other parameters as in Fig. 4.1.

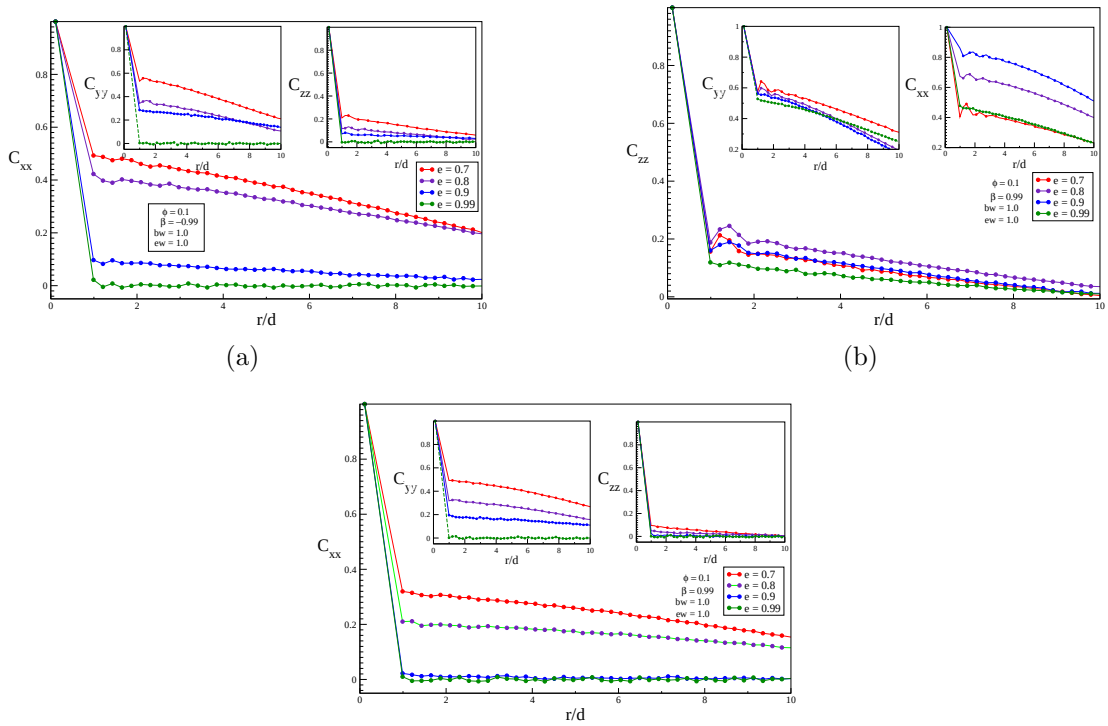

Figure 4.14: Effect of dissipation on velocity correlation functions: (a) $\beta = -0.99$, (b) $\beta = 0$ and (c) $\beta = 0.99$. Other parameters as in Fig. 4.1.

4.2 Dense Flows

In this section we discuss about the dense flows, with a particle volume fraction $\phi = 0.5$. The number of particles used in this simulation work are $N = 19600$ within a domain with L/d=20, W/d=50, H/d=20. These values have been chosen in order to compare our results qualitatively with the experimental work of Orpe *et al* (2007). The various restitution coefficients used in this work are $e = 0.9$, $\beta = 0.9$, $e_w = 1.0$ and $\beta_w = 1.0$.

Fig. 4.15(a) shows a particular snapshot in the steady state at a time marked in energy vs time plot in Fig. 4.15(b). The flow has reached a statistical steady state.

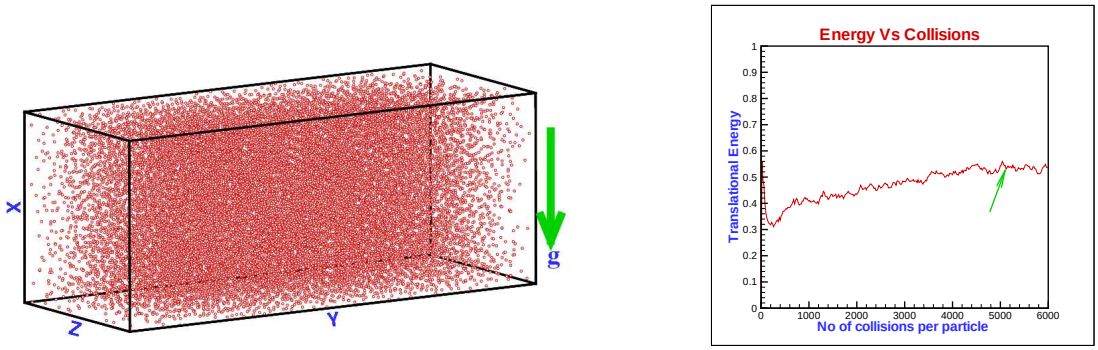

(a) (b)

Figure 4.15: (a) Typical snapshot of the particles and (b) energy vs time (no of collisions per particle) for N=19600, L/d=20, W/d=50, H/d=20, ϕ=0.5, e_w=1.0, β_w=1.0, e=0.9 and β=0.9

4.2.1 Mean field quantities

To present the *binwise* profiles of the macroscopic quantities, the y-direction has been divided into 25 bins. It is observed from Fig. 4.16 that the flow is in the form of a *plug* across the width of the channel. Looking at the density profile , Fig. 4.16(a), we can divide the flow into two regions: two shear layers near the walls and a uniform dense shear-free flow at the center of the channel. In the following subsections, we will present macroscopic results in $bin = 1$ (near the wall), $bin = 3$ (in the shear region) and $bin = 13$ (along the centerline).

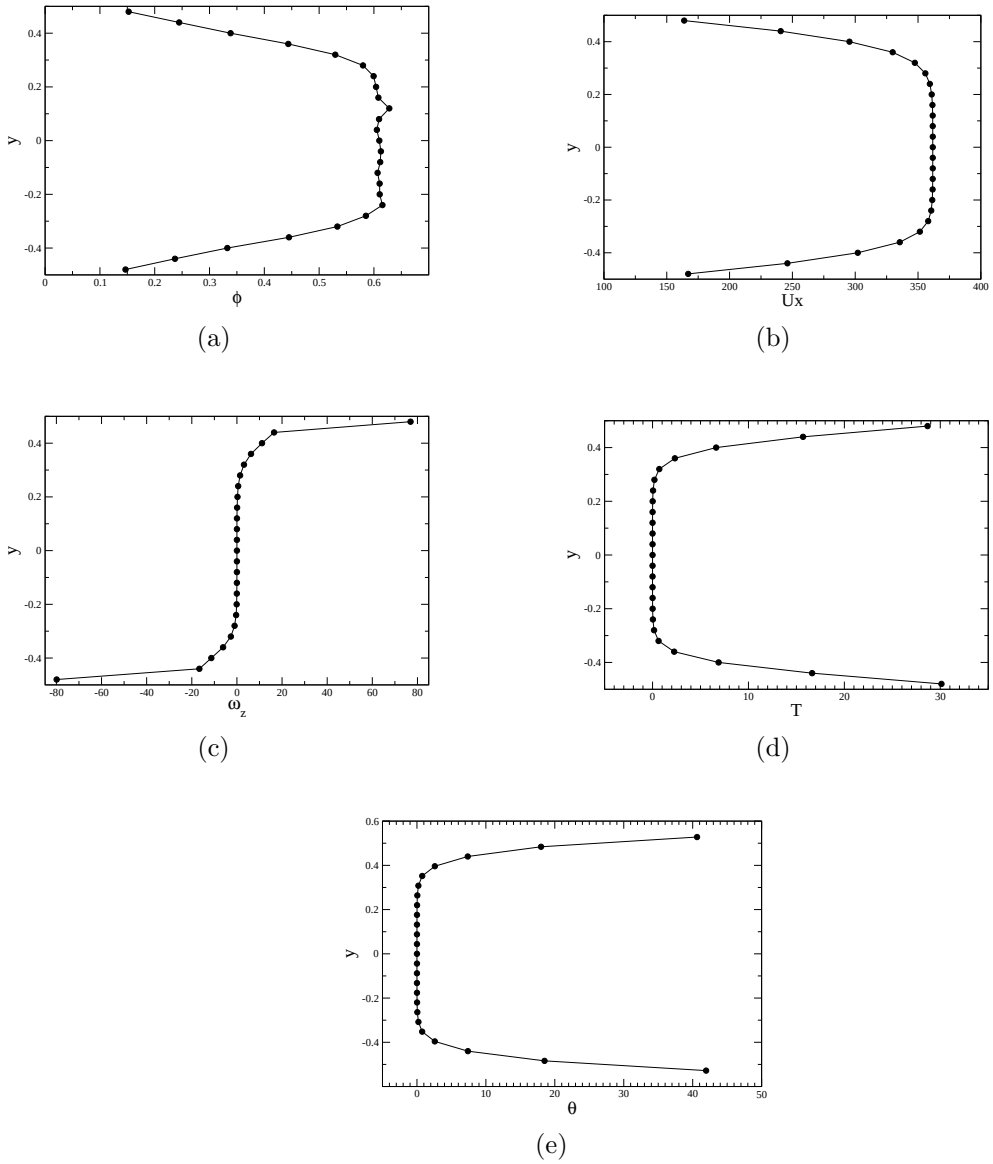

Figure 4.16: Binwise mean field quantities. (a) Density, (b) U_x, (c) ω_z, (d) Translational temperature and (e) Rotational temperature. Other parameters as in Fig. 4.15

4.2.2 Pair Correlation Function

Fig. 4.17 shows the pair correlation function for different regions in the domain. Near the wall ($bin = 1$) and in the shear region ($bin = 3$) there is insignificant correlation, an indication of the absence of any ordering of particles since mostly particles are in the dense *plug* region along the channel centerline. However, in the

middle region ($bin = 13$) there are visible dominant peaks at integral values of r/d upto $r/d = 8$ indicating a liquid-like structure around the channel centerline.

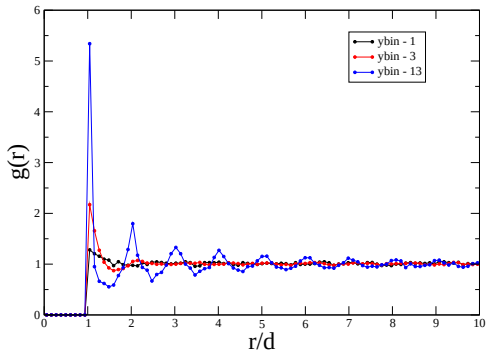

Figure 4.17: Pair correlation function. Other parameters as in Fig. 4.15

4.2.3 Velocity Distribution Function

Fig. 4.18(a) shows the VDFs for streamwise velocity (C_x) in three bins. We see that near the wall ($bin = 1$), there is deviation from Gaussian in the low-velocity range. The shear region ($bin = 3$) too have significant deviations with asymmetry. However, in the dense region ($bin = 13$), the tails are stretched out of Gaussian but symmetry still exists. Similar deviations are observed for $P(C_y)$, see Fig. 4.18(b). There is considerable deviation from Gaussian in the low-velocity region. The VDF in the shear region is strongly asymmetric, but towards the positive side, and we see stretched tails in the dense middle region. However, $P(C_z)$ is following Gaussian in the low velocity region for all bins but there is some deviation in their tails in $bin = 3$ and $bin = 13$. Similar behaviour is seen for $P(\Omega_x)$ and $P(\Omega_y)$, but $P(\Omega_z)$ has asymmetry in the low velocity region with stretched tails for the middle bin. The tails of $P(\Omega_y)$ differ siginificantly from a Gaussian in all three bins.

4.2.4 Velocity Correlation Function

The translational velocity correlation functions for the dense flow at $\phi = 0.5$ are shown in Fig. 4.19. The streamwise velocity correlation C_{xx} is close to zero in

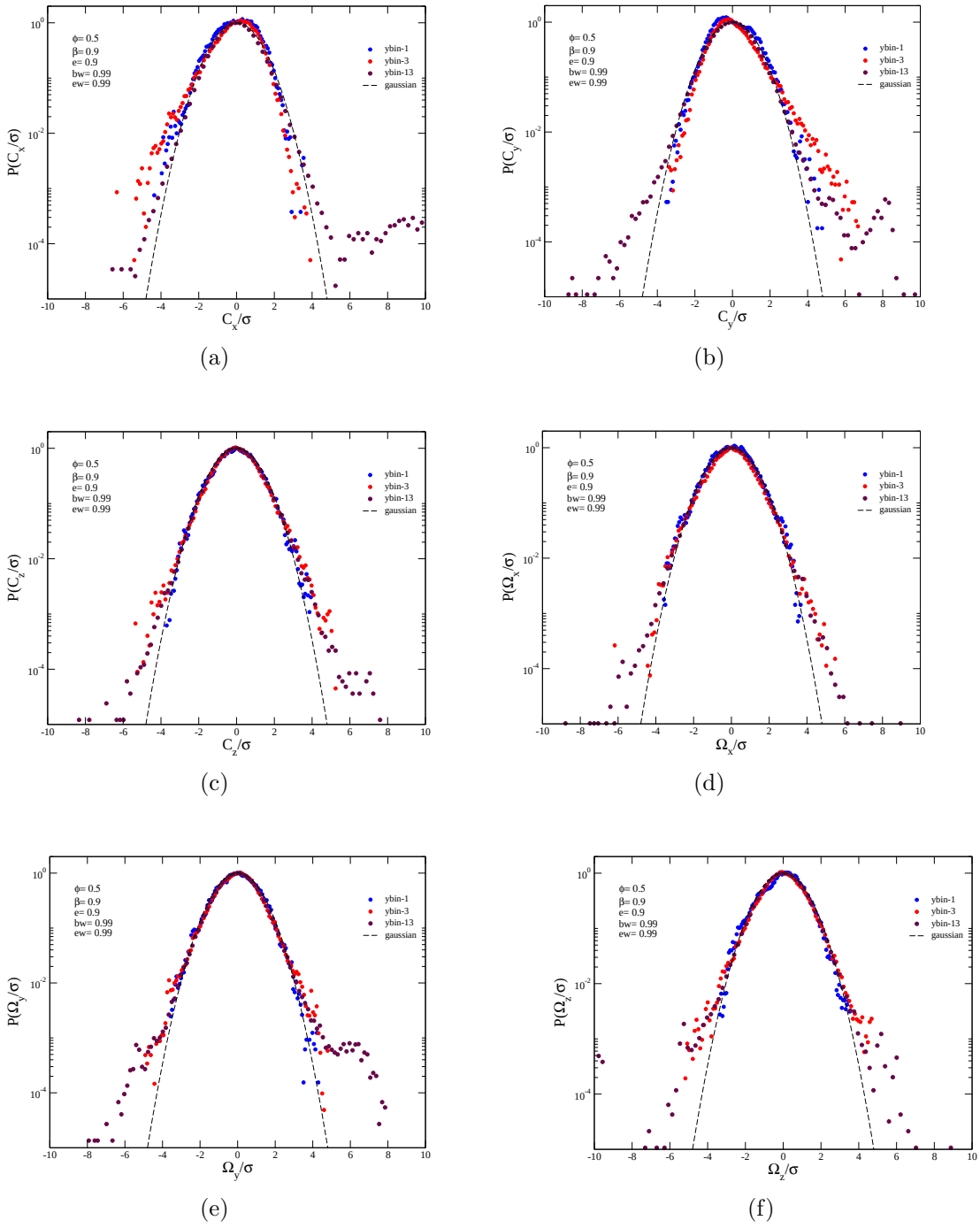

Figure 4.18: Velocity distribution functionss: (a) C_x, (b) C_y, (c) C_z, (d) Ω_x, (e) Ω_y and (f) Ω_z. Other parameters as in Fig. 4.15

all bins, see Fig. 4.19(a). However, looking at the spanwise velocity correlation C_{yy} in Fig. 4.19(b), we find significant amount of correlation in the dense region

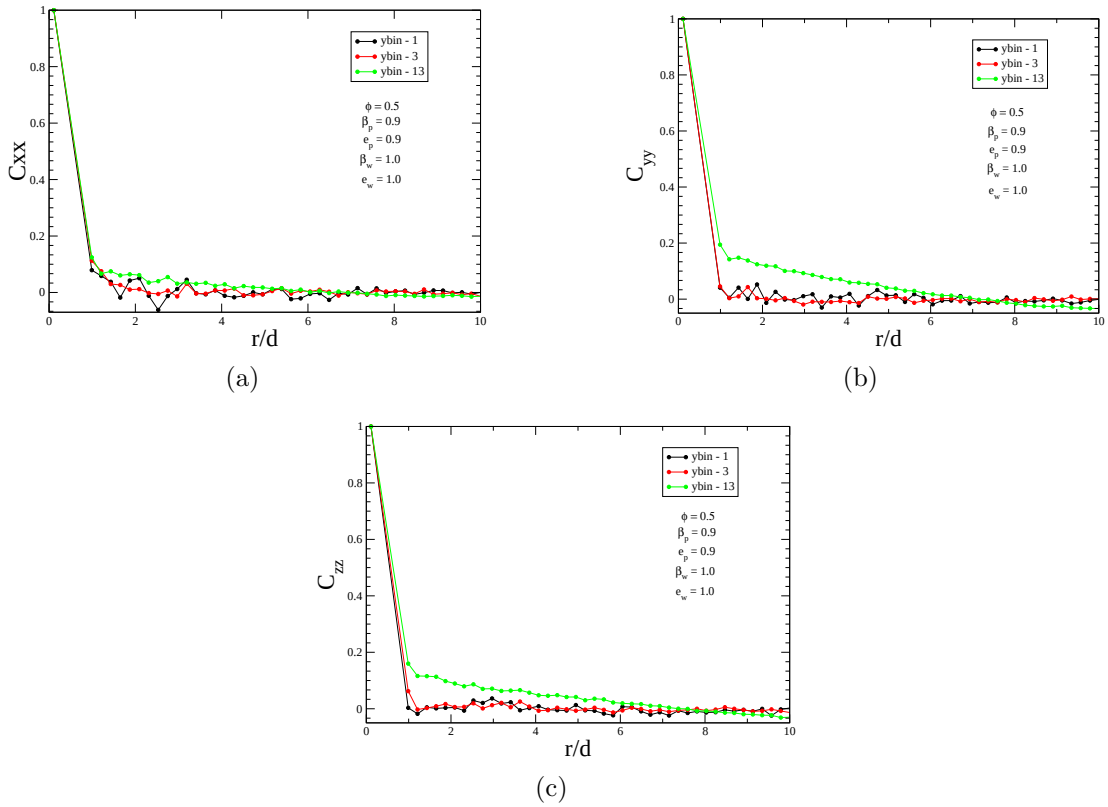

Figure 4.19: Velocity correlation functions: (a) C_{xx}, (b) C_{yy} and (c) C_{zz}. Other parameters as in Fig. 4.15

($bin = 13$) but in the regions near the wall and the shear zone, the velocity correlations are stil negligible and close to zero. Similar behaviour is observed for C_{zz} in Fig. 4.19(c). The cross correlations were found to be significantly osscilatory and hence not shown here. These observations help us to conclude that there are enhanced velocity correlations around the channel centreline which could be responsible (along with dissipation) for deviations of the velocity distribution functions from Gaussian distributions. Fig. 4.20 shows the binwise variation of average orientational correlation. It is averaged over the simulation run for time $t = 80000$ collisions per particle.

4.2.5 Summary

From the present set of results it is observed that the spatial velocity correlations near the walls are different from those in the bulk and the strength of these velocity

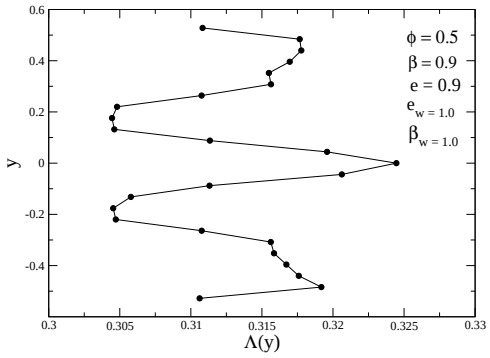

Figure 4.20: Orientational correlation function. Other parameters as in Fig. 4.15

correlations is greater in the dense region along the channel centreline. These findings are contrary to what Orpe & Kudrolli (2007) have observed.

The experimental results of Moka & Nott (2005) suggest that the translational velocity distribution functions are same in the dense "plug" region around the channel centerline and in the "shear-layer" near the wall. Our results indicate that even though the rotational VDFs in the *plug* region and shear-layer appears to be similar, there are noticeable differences in translational VDFs in these two regions. These differences could possibly be related to the fact that the bottom-plate in these experiments is "partially" open and hence there are dead-zones at the bottom of the experimental set-up which would lead to "back-flows". In future, we plan to exactly mimic the experimental set-up in our simulation.

CHAPTER 5

LARGE SCALE STRUCTURES

The present chapter discusses about the formation of density waves and large scale structures in the simulation of three-dimensional gravity-driven granular Poiseuille flow.

There has recently been a significant amount of interest in understanding the formation of density waves and their effect in rapid granular flows (Alam & Nott (1998); Wang *et al.* (1997); Liss *et al.* (2002); Goldhirsch (2003); Alam *et al.* (2008)). Density waves may affect the flow properties, heat transfer and reaction rates of a process involving granular materials (Jackson (2000); Chen (1996)). The density waves in bounded granular flows has been studied by various authors. A two-dimensional molecular dynamic simulation of flow through a narrow vertical pipe concluded that density waves become apparent even if the flow is initially uniform (Poschel (1994)). A lattice-gas automata simulation was used to examine the density waves (Peng & Herrmann (1994)) and it was found that inelastic collisions between the particles (dissipation) and rough walls were necessary for the formation of these waves and were observed only when the average density of the system was in a certain range. In an experimental measurement of granular material flowing down a tube (Raafat *et al.* (1996)), it was observed that density waves formed only at intermediate flow rates between low density free fall regime and a high compactness slower flow. Density waves in gravity-driven granular flows in a vertical channel have been modelled using a variety of techniques including modeling the system as interacting kinetic waves (Lee & Leibig (1994)), using the Langevin equation (Reithmuller *et al.* (1997)) and using kinetic theory of dissipative gases. A linear stability analysis of the equations of motion for granular materials for two dimensional flow between parallel walls (Wang *et al.* (1997)) showed that the base state was unstable to perturbations in the form of density waves. Three diferent types of unstable modes were identified from the linear stability analysis.

Event-driven particle simulations were performed to study the gravity-driven flow of granular materials in a vertical channel (Liss *et al.* (2002); Vijaykumar (2007)). Three distinct types of density variations were identified: a plug, an

$S-shaped$ wave (with one or more humps) and a clump (also called as slug). The dynamics of large systems were found to be qualitatively different from those of small systems due to the fact that the density inhomogeneities that form in small systems can be different from those that form in large systems.

The above-mentioned simulation studies (Liss *et al.* (2002); Vijaykumar (2007)) are restricted to two-dimensions with "smooth" particles. The present work probes density waves in "3D" granular Poiseuille flow with "rough" particles. The density waves are probed in detail over a range of parameters and aspect ratios of the simulation domain.

5.1 Fourier Analysis

The denisty waves have been explored in detail by performing a Fourier analysis of the density field by using the two-dimensional FFT subroutine available in MATLAB to quantify the modes of instability and analyze the temporal structures in the flow. Fourier analysis is used to examine the development of the wavy and slug flow regimes in the spatial domain by monitoring dominant waves in wave-number space.

The density fields were generated by dividing the simulation domain into $N_1 \times N_2$ cells (in a 2D plane at a time) to obtain the even distribution of $N_1 \times N_2$ data points (in the from of a matrix) in space domain. The FFT alogorithm generates complex Fourier expansion coefficients, $\mathbf{X}$. The complex Fourier coefficients were used to compute the power spectra, $\mathbf{P}$, given by the following expression:

$$\mathbf{P} = \frac{2.\mathbf{X}.conj(\mathbf{X})}{(N_1 N_2)^2}.$$

The power spectra is normalised by the size of matrix to remove its dependence on the mesh size. The power spectra, $\mathbf{P}$, for the Fourier transforms of the density fields are represented as cone plots in the wave-number plane where the amplitudes of the various peaks corresponds to the coefficient $|a_{x,y}|$ (focussing on waves in the xy-plane) in the general Fourier series expansion, $a_{x,y}\ exp\big[2\pi\ i\ ((k_x x/L) + (k_y y/W))\big]$, where $a_{x,y}$ is complex and the coordinates of a peak correspond to particular harmonic values k_x and k_y. Thus each peak depicts the significance of a particular wave number mode for the granular flow. Further details about the

steps involved in computing the power spectrum can be obtained from the work of Liss *et al.* (2002).

5.1.1 Cellwise averaging

The density field and the velocity vector plots presented here are based on cellwise averaging. The simulation domain is divided into $N_1 \times N_2 \times N_3$ cells. The average of the desired quantity is taken based on the number of particles present in each cell. In the following, we have extensively used "TecPlot" (a commercial software) for the visualisation of particle positions in a snapshot, the density field and the velocity vectors.

5.2 Results and Discussion

The present work deals with the formation of density waves and large-scale structures in a **moderately dense flow** ($\phi = 0.15$). Various parameters used for this simulation work are:

$$\begin{aligned} \text{Particle volume fraction} \quad & \phi = 0.15 \\ \text{Particle-particle normal coefficient of restitution} \quad & \mathrm{e} = 0.7 \\ \text{Particle-wall normal coefficient of restitution} \quad & \mathrm{e}_w = 0.99 \\ \text{Particle-particle tangential coefficient of restitution} \quad & \beta = 0.1 \\ \text{Particle-wall tangential coefficient of restitution} \quad & \beta_w = 0.99. \end{aligned}$$

The system starts from a homogeneous initial condition of a low granular temperature. The energy increases as the particles speed up due to the gravitaional force. As the particle velocities increase, the dissipation of the energy increases due to inelastic particle-particle and particle-wall collisions. Hence we can see a plateau in the translational energy vs time plots (such as in Fig. 5.1(b)). This plateau corresponds to the *fully developed* state with an associated flow structure.

5.2.1 Effects of Channel-width (W/d) and Aspect ratio (L/W)

Aspect Ratio $L/W = 0.6$

The analysis begins with a less number of particles in a domain having small length in the flow direction in comparison to the width and height, 600 particles in a domain with $L/W = 0.6$, $W/d = 15$, $H/d = 15$. The particles are distributed

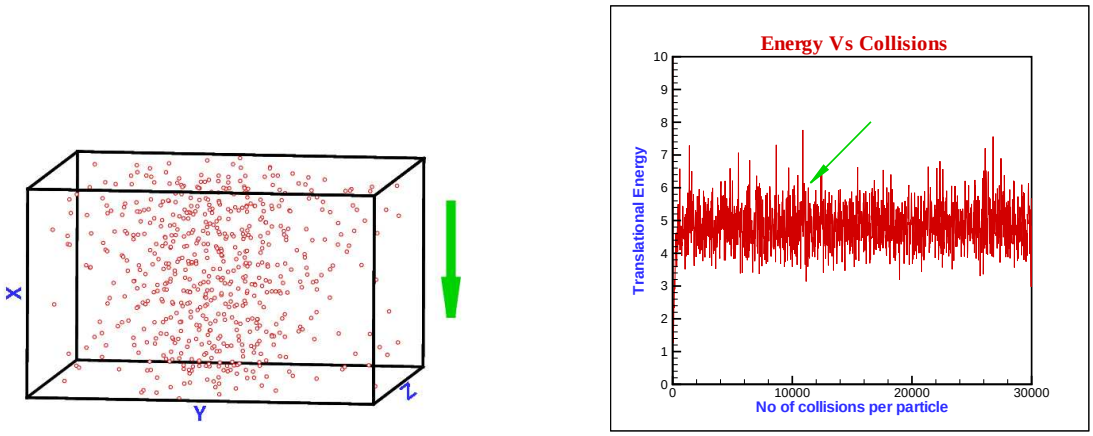

(a) Particle positions (b) Time trace of average kinetic energy

Figure 5.1: (a) Particle positions; (b) Time trace of average kinetic energy; N=600, L/W=0.6, W/d=15, H/d=15, ϕ=0.15, e=0.7, e_w=0.99, β=0.1, β_w=0.99

throughout the system, as can be seen in Fig. 5.1(a). The thick green arrow shows the direction of granular flow due to the gravity acting on particles. The snapshot of the system shown here was taken at the time depicted by the thin green arrow on the energy vs time (number of collisions per particle) plot, in Fig. 5.1(b). The particles have shifted towards the center of the channel but there is no visible structure.

Fixing this aspect ratio at $L/W = 0.6$, we increase the number of particles to 4800 in a domain with larger channel width and height $W/d = 30$, $H/d = 30$. Although the system was started from a homogeneous initial condition, as the simulation proceeds the particles moved away from the walls and start to form a dense region in the center of the domain. This dense region consolidates to form a *plug flow* around the center of the domain, Fig. 5.2(a), with the corresponding energy plot, Fig. 5.2(e), showing the point at which this snapshot was taken. This *plug*, being a three-dimensional structure, can be better seen via slices of the density contour plots in different planes: Fig. 5.2(b) in xy-plane with velocity vectors

superimposed over it, Fig. 5.2(c) in xz-plane and Fig. 5.2(d) in yz-plane. The power spectrum, Fig. 5.2(f) of the plug flow in xy-plane has a dominant peak at $(k_x, k_y) = (0, 1)$ verifying that the plug spans across y-direction. There is no apparent structure in x- or z-directions. The corresponding power spectra in xz- & yz-planes are not shown here.

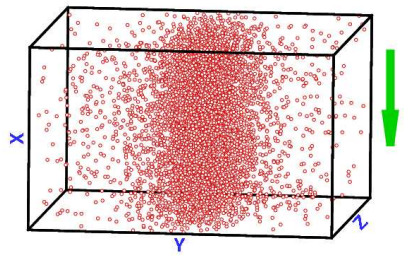

(a) Particle positions

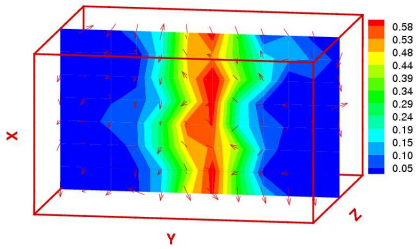

(b) Density contour - xy-plane

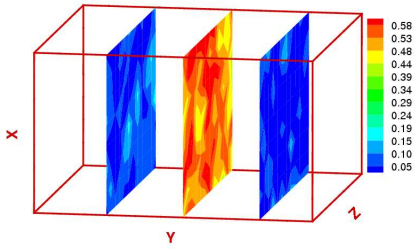

(c) Density contour - xz-plane

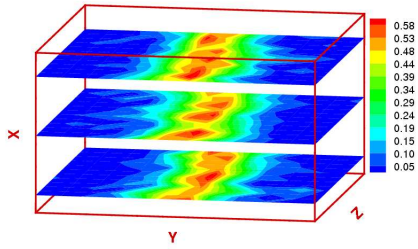

(d) Density contour - yz-plane

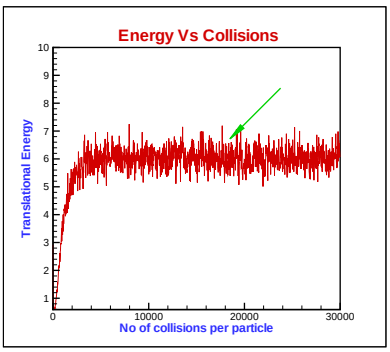

(e) Time trace of average kinetic energy

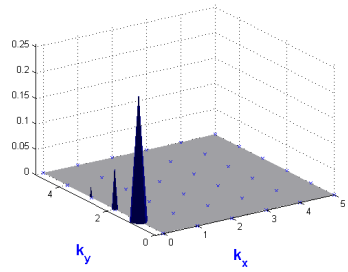

(f) Power spectrum of density field

Figure 5.2: (a) Particle positions; (b) Density contour (xy-plane); (c) Density contour (xz-plane); (d) Density contour (yz-plane); (e) Time trace of average kinetic energy; (f) Power spectrum of density field (xy-plane); N=4800, L/W=0.6, W/d=30, H/d=30; Other parameters as in Fig. 5.1. The colour coding for the density field (particle volume fraction) is shown in respective colour-bar.

The *plug flow* can be considered as a flow where there is a density variation in the wall-normal direction (perpendicular to the direction of flow) but there is no structure in the vertical direction (along the direction of flow). In the entire domain, density is maximum inside this *plug*. The degree of densification at the center of the channel flow is observed to be dependent on the system parameters L/W, W/d, ϕ, etc. Depending on these system parameters, the gradients in the volume fraction across the channel can be more or less pronounced.

At this aspect ratio ($L/W = 0.6$), the number of particles was further increased to 22000 particles in a domain with even larger channel width and height $W/d = 50$, $H/d = 50$. In this situation the *plug* just gets more dense without any considerable changes, Fig. 5.3(a). The density contours, Fig. 5.3(b) to Fig. 5.3(d), and the power spectrum, Fig. 5.3(f), clearly varifies this dense *plug*.

Aspect Ratio $L/W = 1.4$

It is of interest to examine the structure of the plug as the system size is changed. The system size is a siginificant parameter because many research experiments and simulations of granular materials are done for small scales whereas industrial processes are conducted on larger scales. Experimental systems or small-scale simulations may not capture all structures in the flow.

Keeping the physical parameters same but changing the aspect ratio (L/W) of the simulation domain by increasing the length (L) using the same width and height, different types of structures were observed.

Starting with less number of particles (N=1400), in a domain with $L/W = 1.4$, $W/d = 15$, $H/d = 15$, there was no apparent structure, although the particles have shifted towards the center of the channel as shown in Fig. 5.4(a) with the energy vs time plot, Fig. 5.4(b), depicting the point at which this snapshot is taken. Fig. 5.4 should be compared with Fig. 5.1 that corresponds to a lower aspect ratio ($L/W = 0.6$).

With this aspect ratio of $L/W = 1.4$, increasing the number of particles to 10800 in a domain with $W/d = 30$, $H/d = 30$, results in the formation of dense *clumps* or *slugs*. Fig. 5.5(a) shows a snapshot of the fully developed flow. The system started with uniformly distributed particles, but as the time proceeds the *plug flow* (not shown here) was found to be unstable and vertical density variations started to develop and resulted in the *slug* formation. Fig. 5.5(a) should be compared with

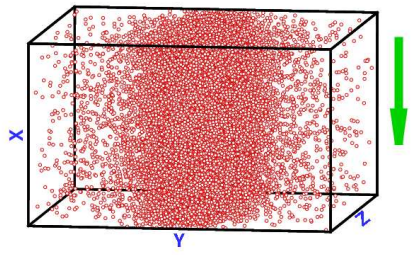

(a) Particle positions

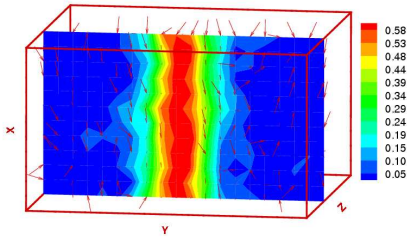

(b) Density contour - xy-plane

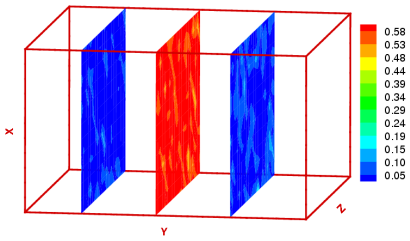

(c) Density contour - xz-plane

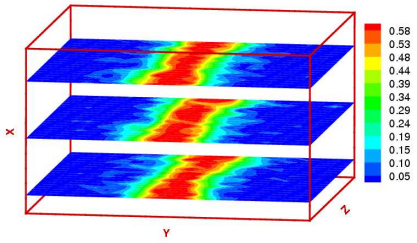

(d) Density contour - yz-plane

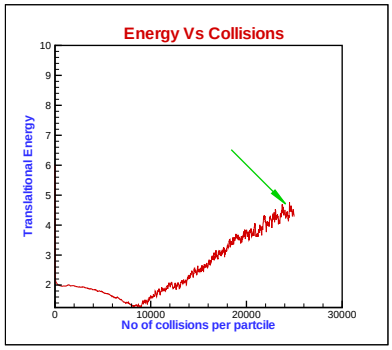

(e) Time trace of average kinetic energy

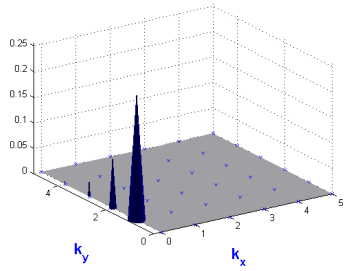

(f) Power spectrum of density field

Figure 5.3: (a) Particle positions; (b) Density contour (xy-plane); (c) Density contour (xz-plane); (d) Density contour (yz-plane); (e) Time trace of average kinetic energy; (f) Power spectrum of density field (xy-plane); N=22000, L/W=0.6, W/d=50, H/d=50; Other parameters as in Fig. 5.1. The colour coding for the density field (particle volume fraction) is shown in respective colour-bar.

its lower aspect-ratio ($L/W = 0.6$) analog in Fig. 5.2(a)

These *slugs* are two dimensional structures *i.e.* there is density variation in x- and y-directions but not much variation in z-direction as can be seen in the corresponding density contours in Fig. 5.5(b) to Fig. 5.5(d). The power spectrum has two dominant peaks at $(k_x, k_y) = (0, 1)$ and $(k_x, k_y) = (1, 0)$ in xy-plane,

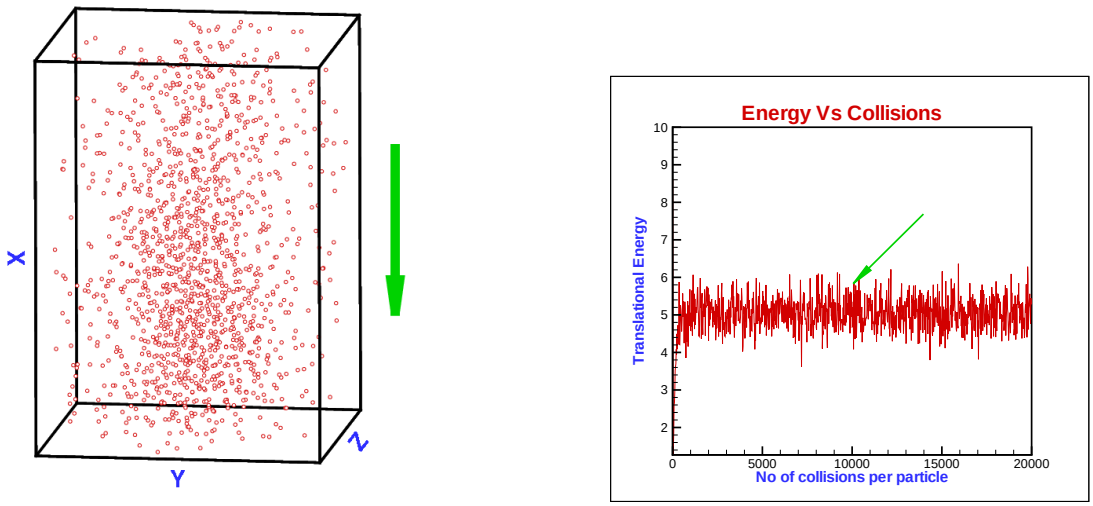

(a) Particle positions (b) Time trace of average kinetic energy

Figure 5.4: (a) Particle positions; (b) Time trace of average kinetic energy; N=1400, L/W=1.4, W/d=15, H/d=15; Other parameters as in Fig. 5.1

Fig. 5.5(e), varifying density variations across x- and y-directions. Since there is no visible density variation across z-direction, the power spectrum in xz-plane is not shown here.

Temporal Evolution of Waves ($L/W = 1.4$)

Increasing the number of particles further to 50094 in domain with $W/d = 50$, $H/d = 50$ (but with the same aspect-ratio $L/W = 1.4$) results in the formation of waves which changes with time. Hence in this case it is interesting to examine the temporal development of these wave structures. At these values of L/W and W/d, the waves do not achieve a single identifiable structure but rather change significantly at different points in time as a dense plug, one-humped wave, two-humped wave and the clumps. The snapshots taken at different times during the simulation are marked on the time trace of average energy by thin green arrows in Fig. 5.6. The corresponding snapshots at four different times are shown in Fig. 5.7(a) to Fig. 5.10(a). Considering the situation from plug flow (at $t = 8000$ collisions per particle), the total energy of the system gradually increases, and does not immediately reach a steady state but continues to increase with time, crossing the one-humped wavy flow (at $t = 10000$ collisions per particle) till getting the two-humped wavy flow (at $t = 11000$ collisions per particle). This is due to the

fact that the structure formation in the system is not yet complete and it takes longer to reach a fully developed state in the form of slug formation (at $t = 14000$ collisions per particle). The slug then consolidates and remain stable over longer periods of time.

At $t \approx 8000$ there is a dense *plug* as seen in Fig. 5.7(a) to Fig. 5.7(d). The power spectra (Fig. 5.7(e)) in the xy-plane and (Fig. 5.7(f)) in yz-plane have dominant peaks at $(k_x, k_y) = (0, 1)$ and $(k_z, k_y) = (0, 1)$, respectively, verifying the location of the plug across y-direction but no apparent density variations in x- or z-direction.

As the system evolves in time, this *plug flow* becomes unstable and vertical density variations start to develop. An one-humped *S-shaped wave* appears at $t \approx 10000$ as shown in Fig. 5.8(a) to Fig. 5.8(d). The observed instability takes the form of an antisymetric mode, *i.e.* a region with an increased density has a corresponding region with a decreased density across the system centerline. This leads to an *S-shaped wave* which moves through the channel. The dominant peak at $(k_x, k_y) = (0, 1)$ in Fig. 5.8(e) refers to variations across y-direction. The transition from a *plug* to an *one-humped wave* is marked by the birth of a second peak at $(k_x, k_y) = (1, 1)$ in Fig. 5.8(e).

At a later time, at $t \approx 11000$, the amplitude of these waves increases significantly, Fig. 5.9(a) to Fig. 5.9(d). The one-humped wave develops into a two-humped *S-shaped* wave. The variations are no longer limited to a particular plane but we can see them across all directions. There are two dominant peaks at $(k_x, k_y) = (0, 1)$ and $(k_x, k_y) = (1, 1)$ in the xy-plane indicating strong density variations across x- and y-directions. There are similar peaks in the yz-plane at $(k_z, k_y) = (0, 1)$ and $(k_z, k_y) = (1, 1)$. The peak at $k_x = 2$ in the xy- and xz-planes quanitifies the two-humped nature of this wave.

Even though the energy of the system appears to reach a plateau after $t \approx 11000$ in Fig. 5.6, it has not reached a steady state. Eventually the two-humped wave leads to the formation of a localized region of high density. This dense region becomes more pronounced, forming a dense *slug* as shown in Fig. 5.10. This *slug* remains stable over a long period of time. The dominant peaks at $(k_x, k_y) = (0, 1)$ and $(k_x, k_y) = (1, 0)$ in the xy-plane, at $(k_x, k_z) = (1, 0)$ in the xz-plane and $(k_y, k_z) = (1, 0)$ in the yz-plane verify that the *slug* is more dominated in the xy-plane.

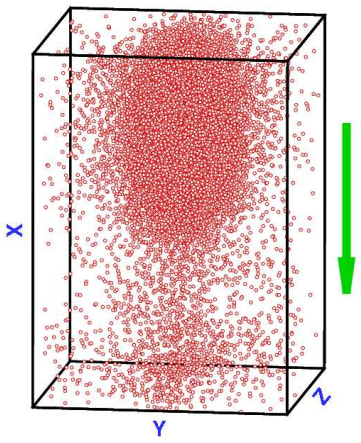

(a) Particle positions

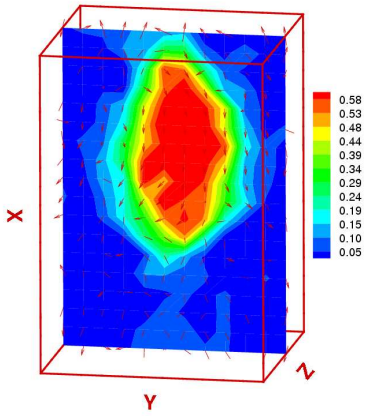

(b) Density contour - xy-plane

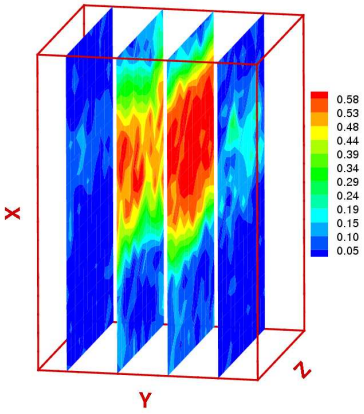

(c) Density contour - xz-plane

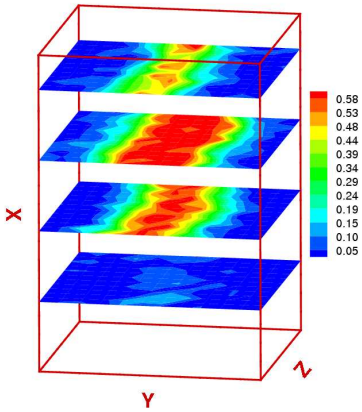

(d) Density contour - yz-plane

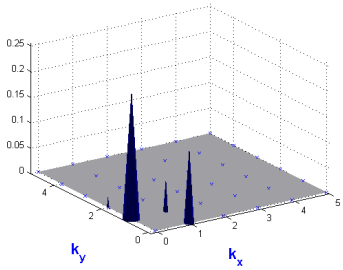

(e) Power spectrum of density field

Figure 5.5: (a) Particle positions; (b) Density contour (xy-plane); (c) Density contour (xz-plane); (d) Density contour (yz-plane); (e) Power spectrum of density field (xy-plane); N=10800, L/W=1.4, W/d=30, H/d=30; Other parameters as in Fig. 5.1. The colour coding for the density field (particle volume fraction) is shown in respective colour-bar.

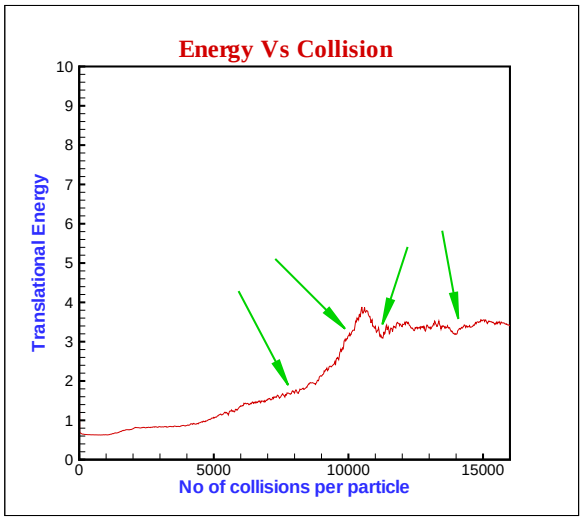

Figure 5.6: Time trace of average kinetic energy; N=50094, L/W=1.4, W/d=50, H/d=50; Other parameters as in Fig. 5.1

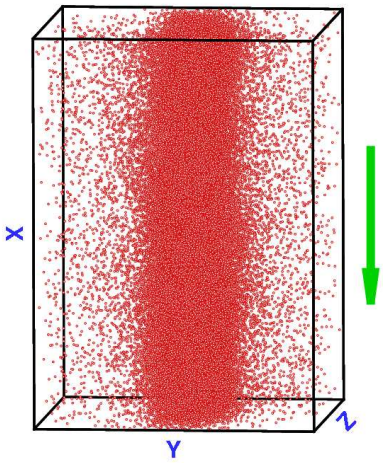

(a) Particle positions

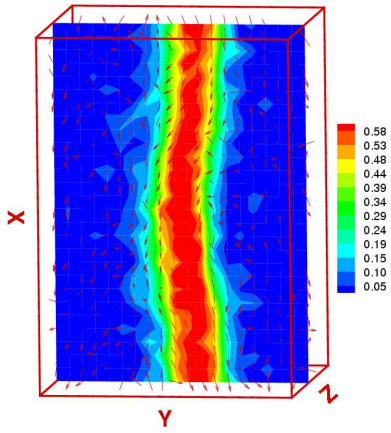

(b) Density contour in xy-plane

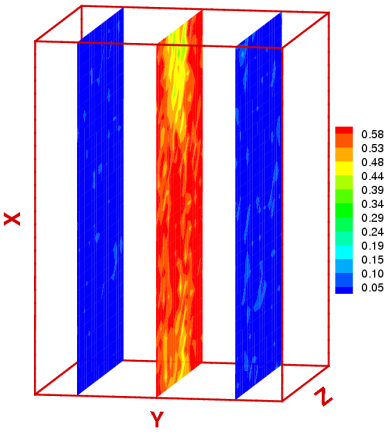

(c) Density contour in xz-plane

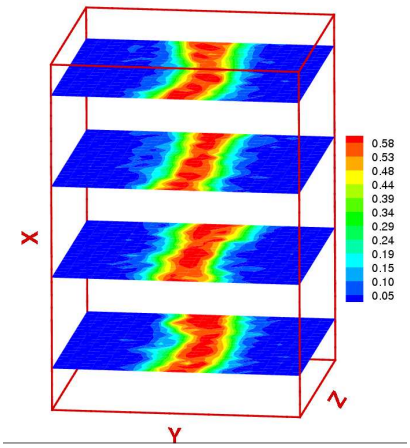

(d) Density contour in yz-plane

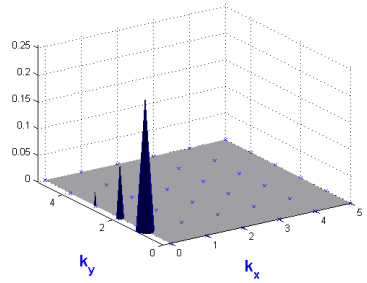

(e) Power spectrum in xy-plane

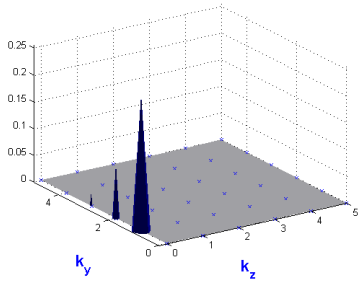

(f) Power spectrum in yz-pane

Figure 5.7: Density structures at $t = 8000$ collisions per particle; Other parameters as in Fig. 5.6. The colour coding for the density field (particle volume fraction) is shown in respective colour-bar.

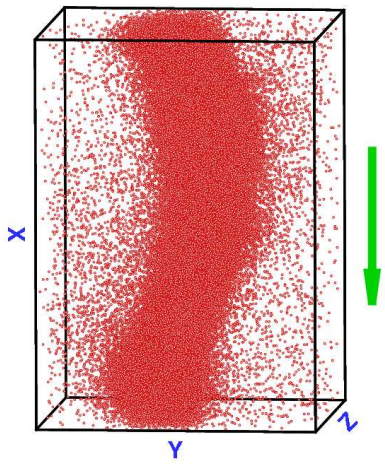

(a) Particle positions

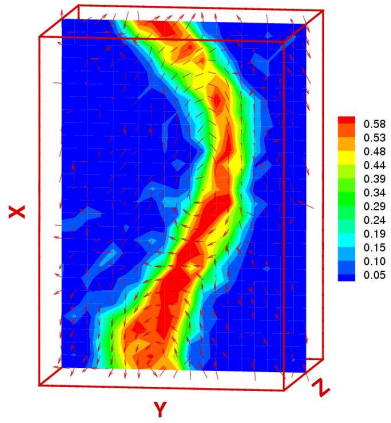

(b) Density contour in xy-plane

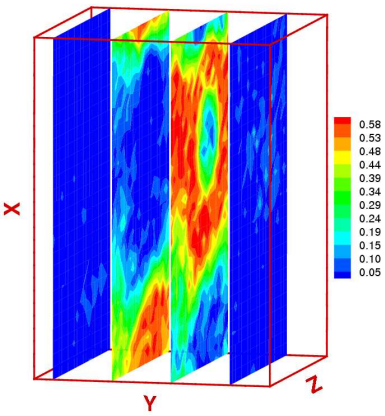

(c) Density contour in xz-plane

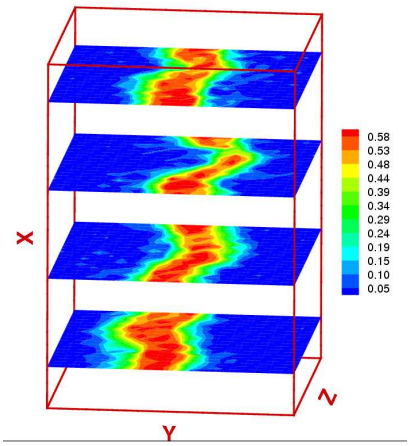

(d) Density contour in yz-plane

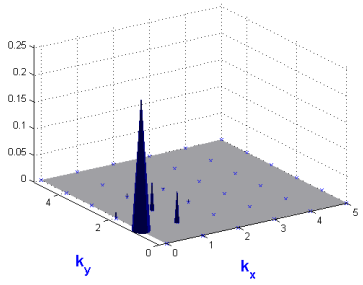

(e) Power spectrum in xy-plane

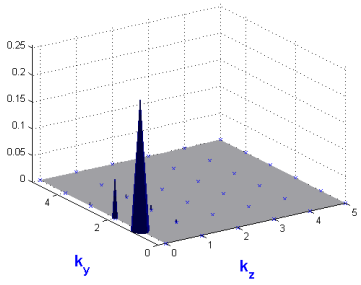

(f) Power spectrum in yz-pane

Figure 5.8: Density structures at $t = 10000$ collisions per particle; Other parameters as in Fig. 5.6. The colour coding for the density field (particle volume fraction) is shown in respective colour-bar.

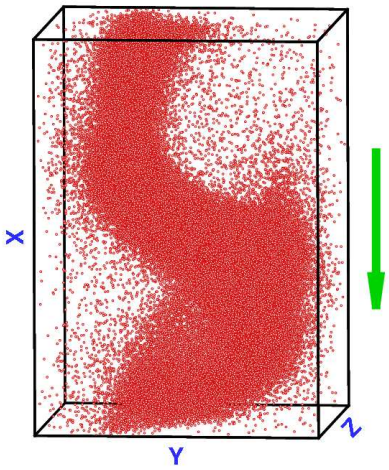

(a) Particle positions

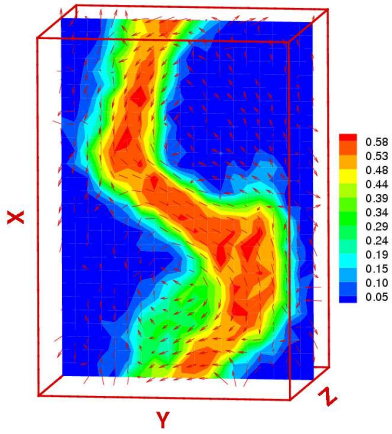

(b) Density contour in xy-plane

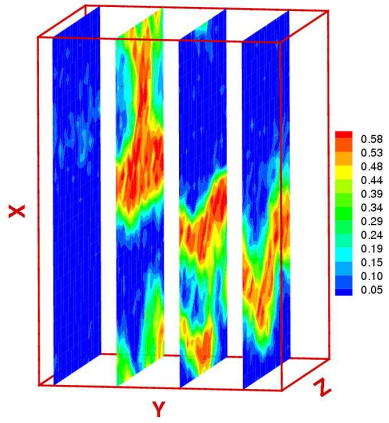

(c) Density contour in xz-plane

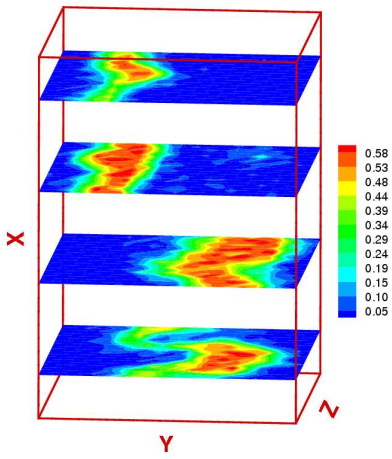

(d) Density contour in yz-plane

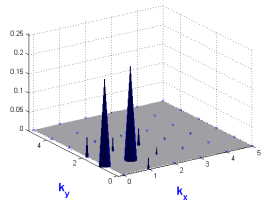

(e) Power spectrum in xy-plane

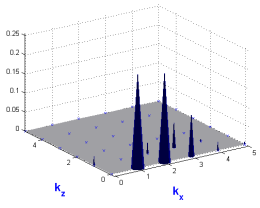

(f) Power spectrum in xz-plane

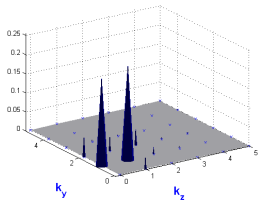

(g) Power spectrum in yz-pane

Figure 5.9: Density structures at $t = 11000$ collisions per particle; Other parameters as in Fig. 5.6. The colour coding for the density field (particle volume fraction) is shown in respective colour-bar.

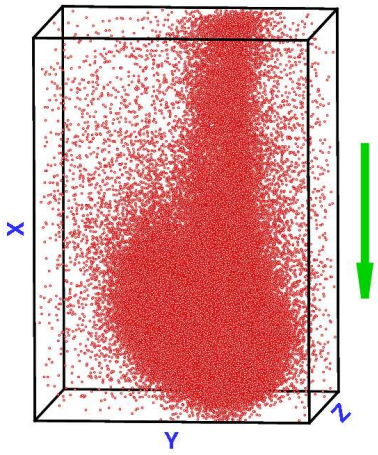

(a) Particle positions

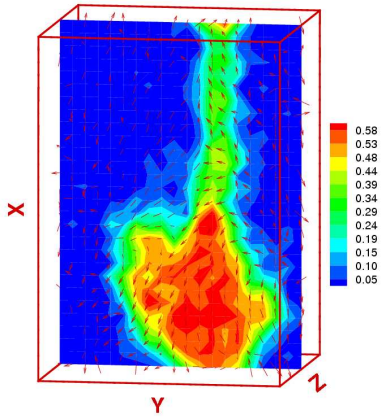

(b) Density contour in xy-plane

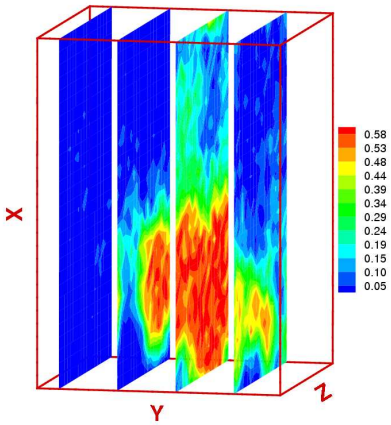

(c) Density contour in xz-plane

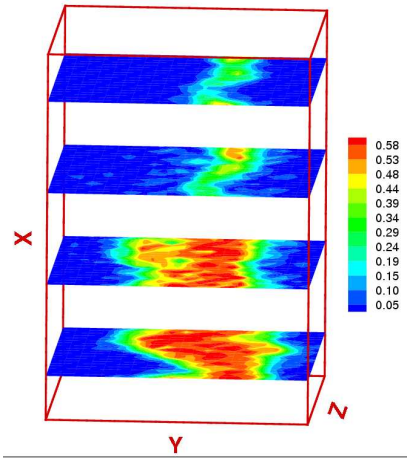

(d) Density contour in yz-plane

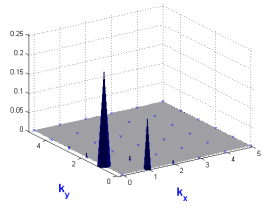

(e) Power spectrum in xy-plane

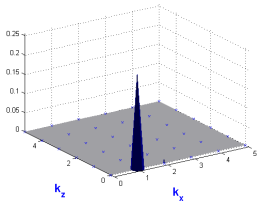

(f) Power spectrum in xz-plane

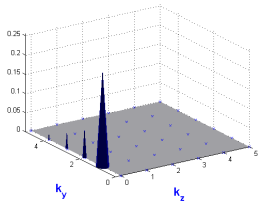

(g) Power spectrum in yz-pane

Figure 5.10: Density structures at $t = 14000$ collisions per particle; Other parameters as in Fig. 5.6. The colour coding for the density field (particle volume fraction) is shown in respective colour-bar.

Aspect Ratio $L/W = 3$

Let us change the simulation domain aspect ratio (L/W) further by increasing the length(L) but keeping the width and height constant with physical parameters as mentioned earlier. Once again, we start the simulation with less number of particles, N=3000, such that $L/W = 3$, $W/d = 15$, $H/d = 15$. As soon as the system reaches a fully developed state, Fig. 5.11(h), we can see the formation of a *slug*, in Fig. 5.11(a). This *slug* does not change its structure with time. The density contour plot slices show the presence of density variations across different planes. The dominant peaks at $(k_x, k_y) = (1, 0)$ and $(k_x, k_y) = (0, 1)$ in the power spectrum of xy-plane verify the *slug* shape in the xy-plane. In contrast we see only single peaks in xz- and yz-planes because there is negligible density variation along the z-direction.

Increasing the number of particles to N=24000 with $L/W = 3$ and $W/d = 30$, $H/d = 30$ results in a more dense *slug*, clearly visible in Fig. 5.12 (a)-(d), which remains stable over time. In this case also we see negligible density variations across z-direction in comparison to x- and y-directions.

As we have seen earlier, increasing the number of particles intensifies the *slug*, in terms of density as well as its size. But if we increase the number of particles too much, the *slug* is no longer stable as shown in Fig. 5.13. For this case, the number of particles are N=107811 with $L/W = 3$, $W/d = 50$, $H/d = 50$. When the flow reaches a steady state, Fig. 5.13(h), an identifiable structure in the form of an *S-shaped* two-humped wave is visible as shown in Fig. 5.13(a). The density contour slices show the three dimensional structure of this *S-shaped wave*. Since the wave has two humps across the x-direction, the power spectrum in the xy-plane, Fig. 5.13(e), shows two dominant peaks at $(k_x, k_y) = (2, 1)$ and $(k_x, k_y) = (0, 1)$. The dominant peaks at $(k_x, k_z) = (1, 0)$ and $(k_x, k_z) = (3, 0)$ in xz-plane indicate the presence of modulated humps along x-direction.

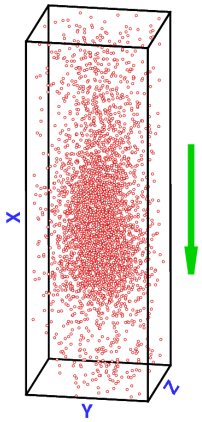

(a) Particle positions

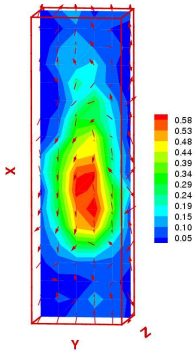

(b) Density contour in xy-plane

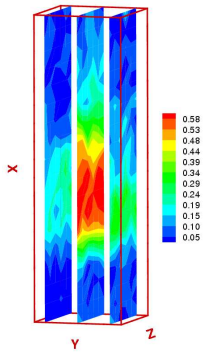

(c) Density contour in xz-plane

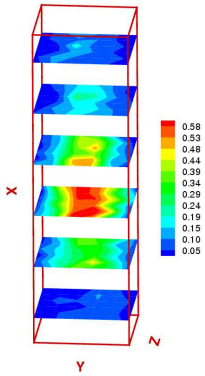

(d) Density contour in yz-plane

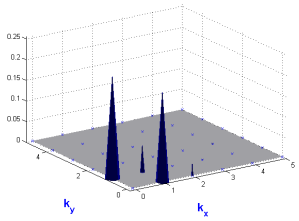

(e) Power spectrum in xy-plane

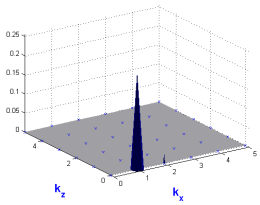

(f) Power spectrum in xz-plane

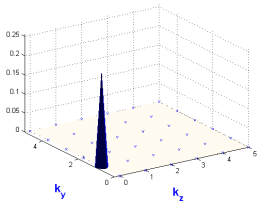

(g) Power spectrum in yz-pane

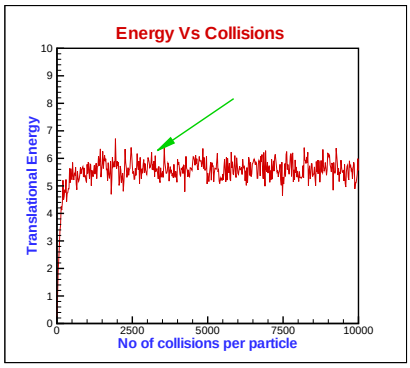

(h) Time trace of averge kinetic energy

Figure 5.11: N=3000, L/W=3, W/d=15, H/d=15; Other parameters as in Fig. 5.1. The colour coding for the density field (particle volume fraction) is shown in respective colour-bar.

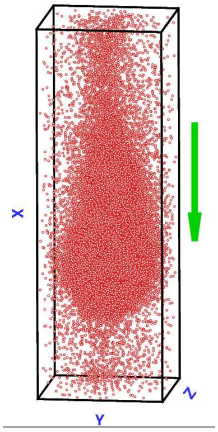

(a) Particle positions

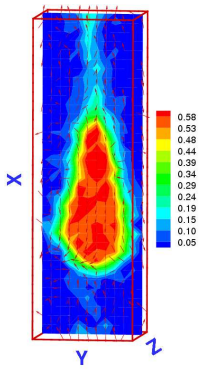

(b) Density contour in xy-plane

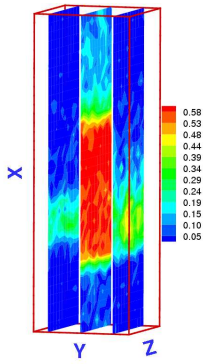

(c) Density contour in xz-plane

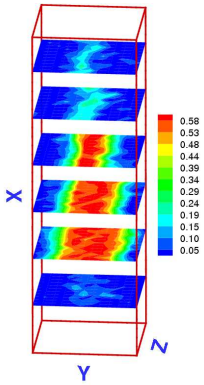

(d) Density contour in yz-plane

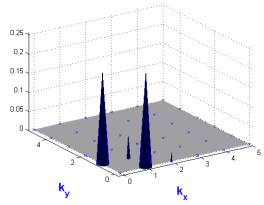

(e) Power spectrum in xy-plane

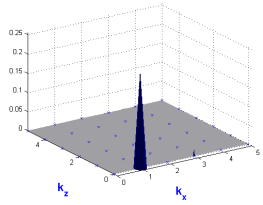

(f) Power spectrum in xz-plane

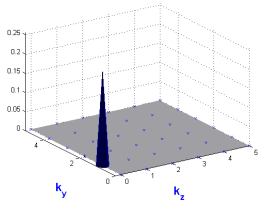

(g) Power spectrum in yz-pane

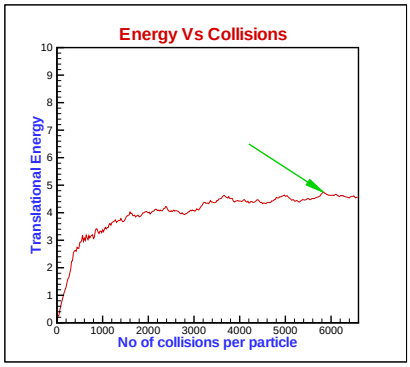

(h) Time trace of averge kinetic energy

Figure 5.12: N=24000, L/W=3, W/d=30, H/d=30; Other parameters as in Fig. 5.1. The colour coding for the density field (particle volume fraction) is shown in respective colour-bar.

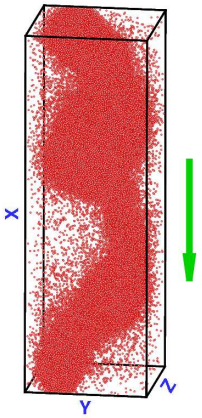

(a) Particle positions

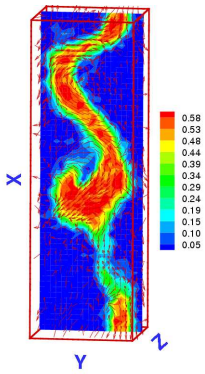

(b) Density contour in xy-plane

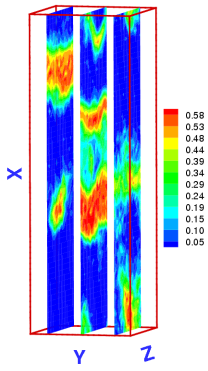

(c) Density contour in xz-plane

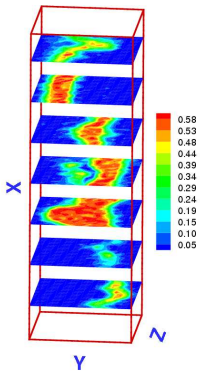

(d) Density contour in yz-plane

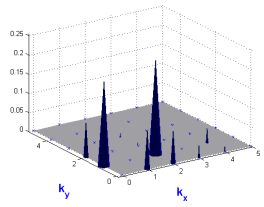

(e) Power spectrum in xy-plane

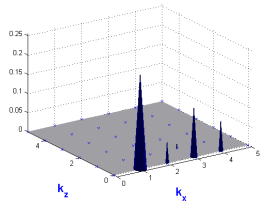

(f) Power spectrum in xz-plane

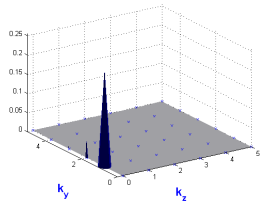

(g) Power spectrum in yz-pane

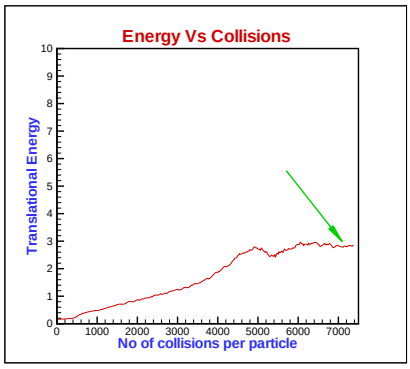

(h) Time trace of averge kinetic energy

Figure 5.13: N=107811, L/W=3, W/d=50, H/d=50; Other parameters as in Fig. 5.1. The colour coding for the density field (particle volume fraction) is shown in respective colour-bar.

Aspect Ratio $L/W = 5$

Lastly, we change the aspect ratio of the simulation domain to $L/W = 5$, with the same width and height and keeping the physical parameters same as before.

The simulation is started with 4800 particles so that $L/W = 5$, $W/d = 15$, $H/d = 15$. Once the system is fully developed, there is a formation of a *slug* as shown in Fig. 5.14. This slug has a fixed structure which persists with time. The power spectrum has dominant peaks at $(k_x, k_y) = (1, 0)$ and $(k_x, k_y) = (0, 1)$, supporting the density variation across x- and y-directions. The presence of only one dominant peak in the xz-plane at $(k_x, k_z) = (1, 0)$ and in the yz-plane at $(k_y, k_z) = (1, 0)$ indicates the absence of the density variations across z-direction.

Increasing the number of particle to 40000 without changing the aspect ratio and other physical parameters such that $L/W = 5$, $W/d = 30$, $H/d = 30$. Once the energy reaches a plateau (not shown) indicating a fully developed flow, the essential steady state structure that emerges is in the form of an *S-shaped wave* along with *slugs*, i.e. a "sandwitch" between an *S-shaped wave* and a *slug*, Fig. 5.15. These waves have a fixed structure that do not change with time and moves through the channel at some constant speed. In a continuum framework, a travelling wave would appear as a steady state when viewed from a frame of reference moving at the speed of the wave. Considering the power spectrum in the xy-plane there are two dominant peaks: one at $(k_x, k_y) = (0, 1)$ for the density variation across y-direction and another at $(k_x, k_y) = (2, 0)$ corresponding to the two-humped structure across x-direction. There is only one dominant peak in the xz- as well as in the yz-plane.

Temporal Evolution of Waves ($L/W = 5$)

With $N = 180000$, and $L/W = 5$, $W/d = 50$, $H/d = 50$, the density waves change with time. At time $t = 4000$ collisions per particle, Fig. 5.16, we get the formation of *S-shaped wave* structures, clearly visible in Fig. 5.17. A closer look at Fig. 5.17 shows that there are two *S-shaped* structures and a $one - humped$ structure. The power spectrum in the xy-plane has peaks at $(k_x, k_y) = (0, 1)$ and $(k_x, k_y) = (0, 2)$ showing the development of two-humps across the y-direction whereas the peak at $(k_x, k_y) = (3, 0)$ corresponds to a three-humped wave in the x-direction.

As time proceeds, the amplitudes of these waves decrease and these three-humped waves reduce to a structure which is a combination of a two-humped wave

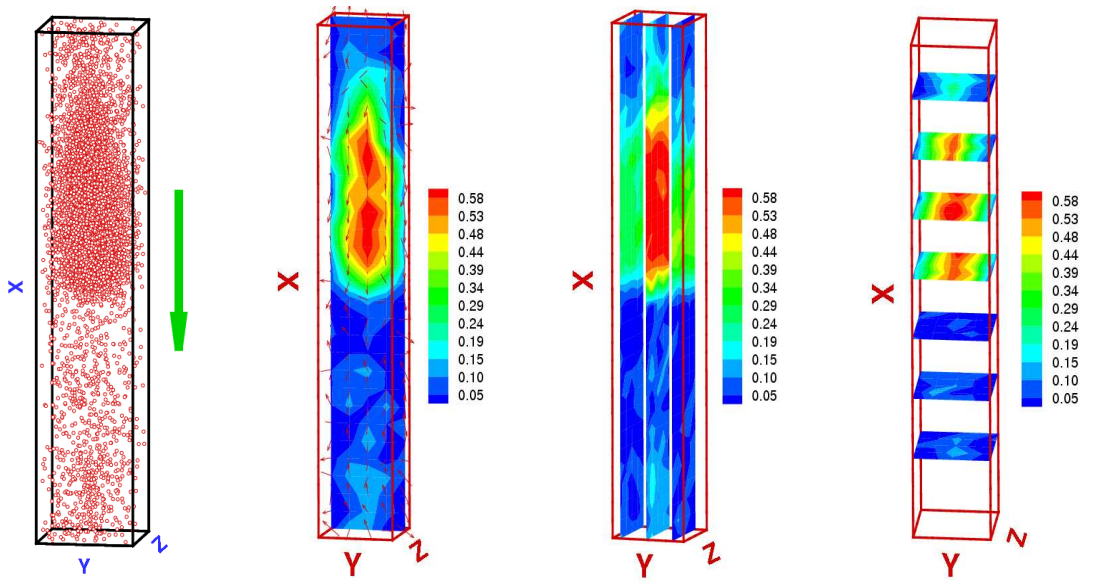

(a) Particle positions (b) Density contour in xy-plane (c) Density contour in xz-plane (d) Density contour in yz-plane

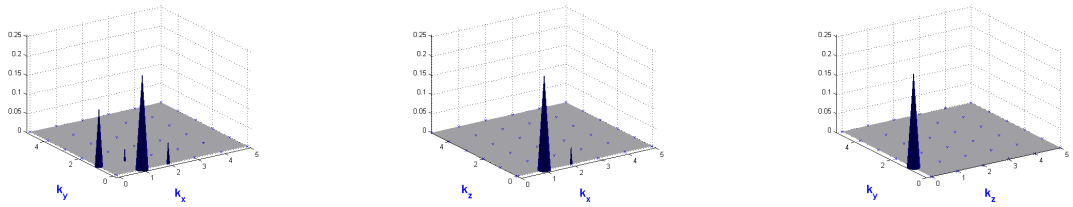

(e) Power spectrum in xy-plane (f) Power spectrum in xz-plane (g) Power spectrum in yz-plane

Figure 5.14: N=4800, L/W=5, W/d=15, H/d=15; Other parameters as in Fig. 5.1. The colour coding for the density field (particle volume fraction) is shown in respective colour-bar.

and a dense *slug*, at time $t = 8000$ collisions per particle as shown in Fig. 5.18. The power spectrum explains this structure clearly. There are two peaks in xy-plane, at $(k_x, k_y) = (2, 1)$ and $(k_x, k_y) = (0, 1)$ quantifying the two-humped wave in x-direction along with the dense plug across y-direction. There is a dominant peak in the xz-plane, at $(k_x, k_z) = (2, 0)$, and at $(k_y, k_z) = (1, 0)$ explaining the observed structure.

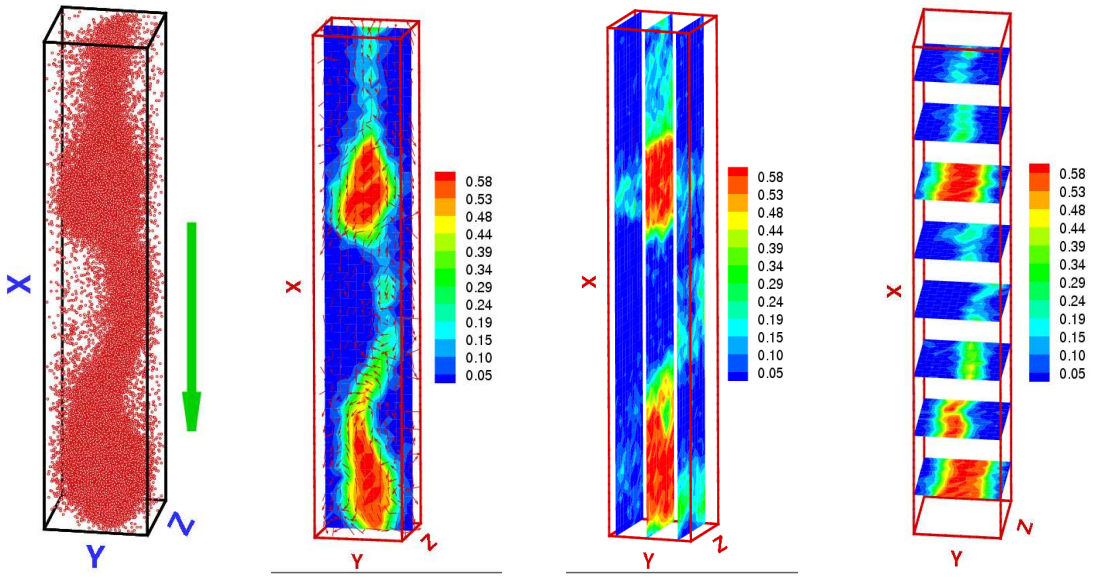

(a) Particle positions

(b) Density contour in xy-plane

(c) Density contour in xz-plane

(d) Density contour in yz-plane

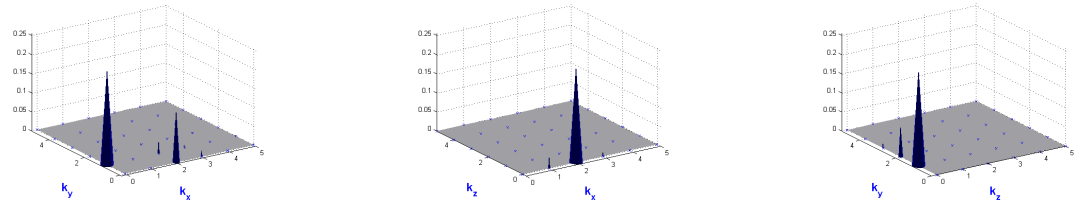

(e) Power spectrum in xy-plane

(f) Power spectrum in xz-plane

(g) Power spectrum in yz-plane

Figure 5.15: N=40000, L/W=5, W/d=30, H/d=30; Other parameters as in Fig. 5.1. The colour coding for the density field (particle volume fraction) is shown in respective colour-bar.

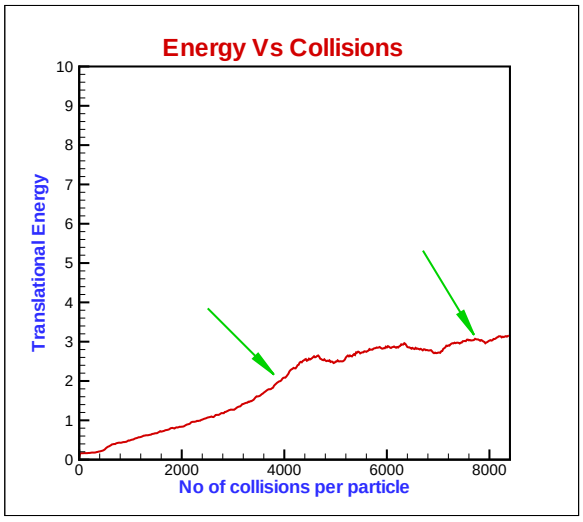

Figure 5.16: Time trace of average kinetic energy; N=180000, L/W=5, W/d=50, H/d=50; Other parameters as in Fig. 5.1

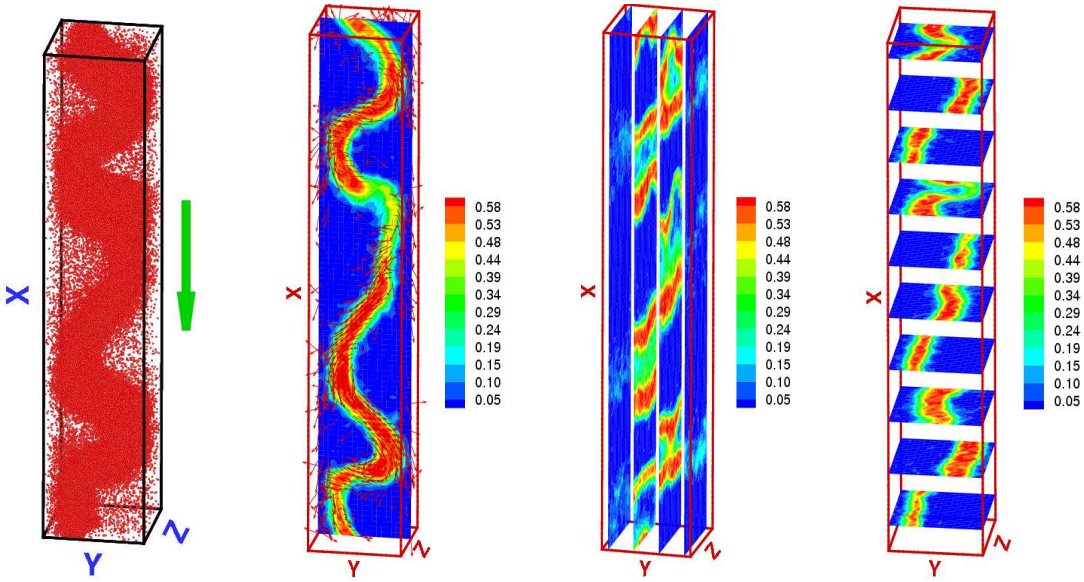

(a) Particle positions (b) Density contour in xy-plane (c) Density contour in xz-plane (d) Density contour in yz-plane

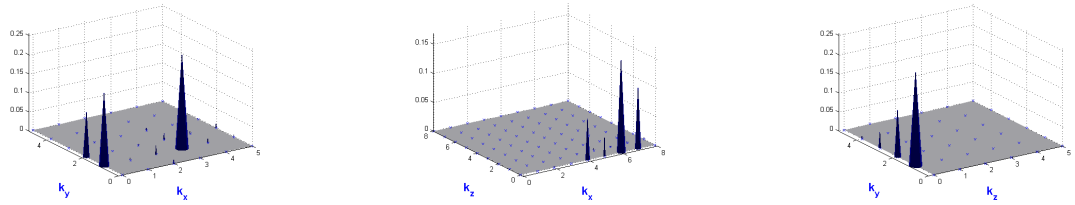

(e) Power spectrum in xy-plane (f) Power spectrum in xz-plane (g) Power spectrum in yz-plane

Figure 5.17: Density structures at $t = 4000$; Other parameters as in Fig. 5.16. The colour coding for the density field (particle volume fraction) is shown in respective colour-bar.

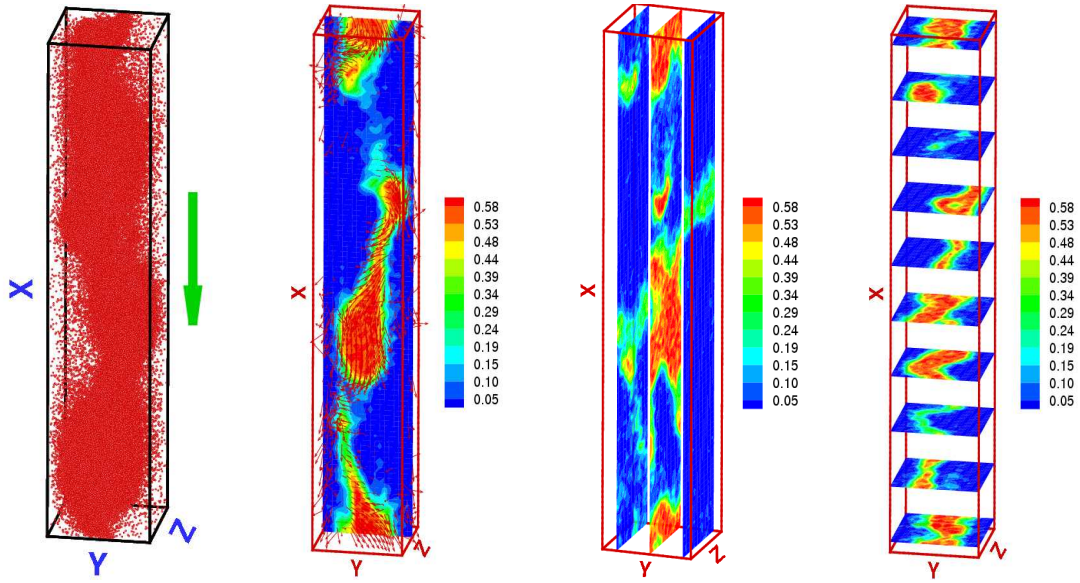

(a) Particle positions (b) Density contour in xy-plane (c) Density contour in xz-plane (d) Density contour in yz-plane

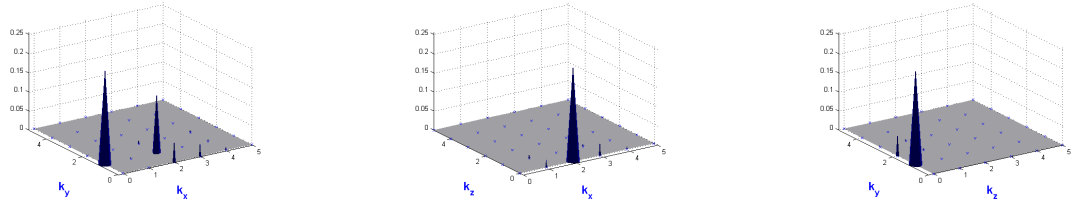

(e) Power spectrum in xy-plane (f) Power spectrum in xz-plane (g) Power spectrum in yz-plane

Figure 5.18: Density structures at $t = 8000$; Other parameters as in Fig. 5.16. The colour coding for the density field (particle volume fraction) is shown in respective colour-bar.

5.2.2 Effect of three dimensionality

We have seen in the previous subsection that there are significant effects of varying the domain aspect ratio (L/W) and the channel width (W/d) on the formation of density waves. For all results in section 5.2.1 we have fixed the height (H) of the channel along the z-direction equal to the channel width (i.e. $H/W = 1$). In the present section we see the effect of three dimensionality on these structures by varying the height (H) of the channel.

The analysis begins with a nearly two-dimensional domain, the z-direction being very small ($H/W = 0.2$), with the number of particles N=21952 in a domain with $L/W = 3$ and $W/d = 50$. Since in the present situation there is very less space for the particles to move in the z-direction and hence they loose less energy in collision with particles in z-direction. In other words the structure formation has to take place mainly in the xy-plane. The density variation in the form of a *wavy slug* in the xy-plane is visible in Fig. 5.19(a). The density contour slices verify the absence of any density variation across z-direction. The peaks at $(k_x, k_y) = (1, 0)$ and $(k_x, k_y) = (0, 1)$ indicates the presence of one-humped wavy slug.

Comparing these observations with the case $L/W = 3$, $W/d = 50$, $H/W = 1$ in Fig. 5.13, we see that the slug in the present situation is nearly similar to the structure in Fig. 5.13 but the waviness is more evident in Fig. 5.13. Note that the present system reaches the steady state in the same way as the system in Fig. 5.13 although the number of particles is much less here.

Now let us increase the height in the z-direction so that the system has $H/W = 3$ with N=323433, $L/W = 3$ and $W/d = 50$. This is the largest number of particles that we used in our simulations. In this case there is more space for the particles to move in the z-direction and hence considerable possibilty of structure formation. Fig. 5.20(a) clearly shows the presence of a three dimensional *wave*. There is density variation across all directions. A notable evidence of structure formation along z-direction is shown in Fig. 5.20(d) which has been magnified to show the velocity vectors in Fig. 5.21(b). The magnified views of density structures along with velocity vectors in the xz-plane (Fig. 5.20(a)) are shown in Fig. 5.22. The vortical-type motions are clearly visible from these plots.

From the above observations we find that there are considerable effects of three-dimensionality on the density variations and structure formation. The density variation in any particular direction depend on the availabilty of space for the

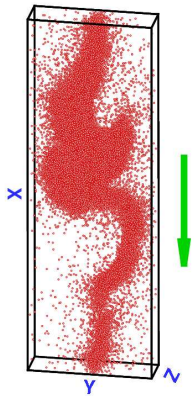

(a) Particle positions

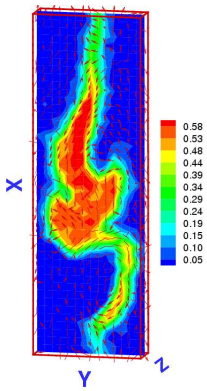

(b) Density contour in xy-plane

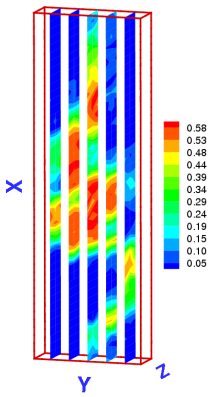

(c) Density contour in xz-plane

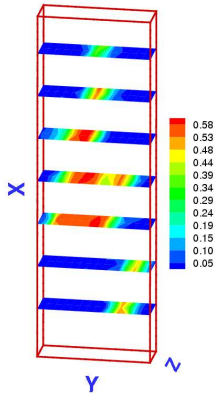

(d) Density contour in yz-plane

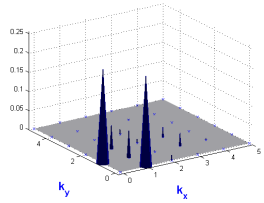

(e) Power spectrum in xy-plane

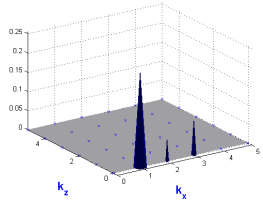

(f) Power spectrum in xz-plane

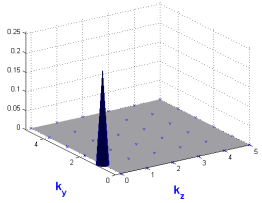

(g) Power spectrum in yz-plane

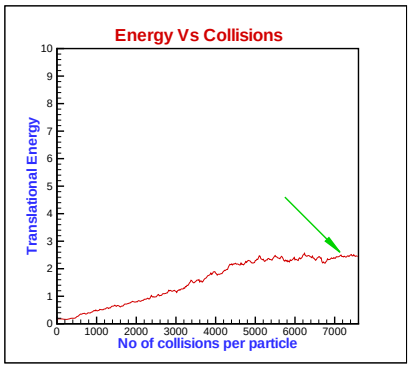

(h) Time trace of averge kinetic energy

Figure 5.19: N=21952, L/W=3, W/d=50, H/d=10; Other parameters as in Fig. 5.1. The colour coding for the density field (particle volume fraction) is shown in respective colour-bar.

particles to collide and loose energy which results in clustering and other structures. This issue need to be investigated further.

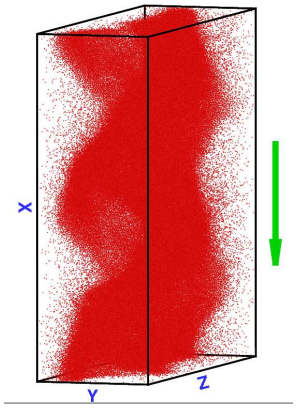

(a) Particle positions

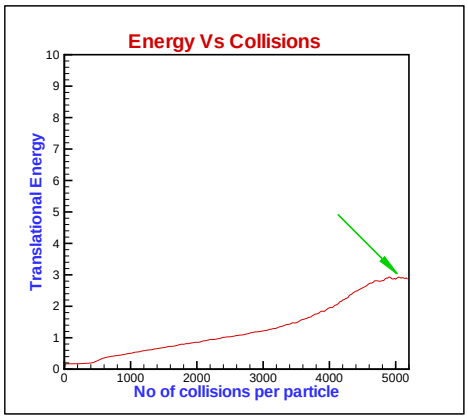

(b) Time trace of averge kinetic energy

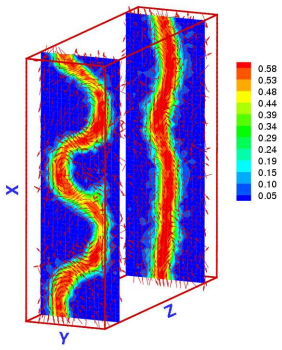

(c) Density contour in xy-plane

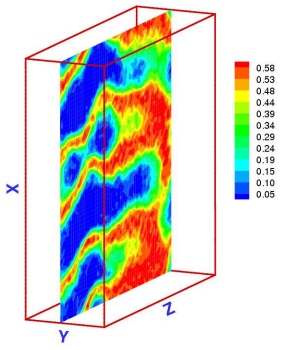

(d) Density contour in xz-plane

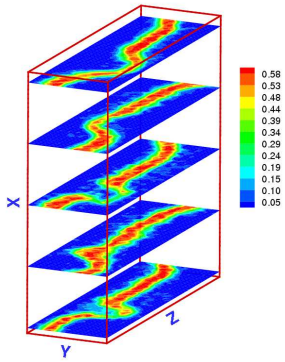

(e) Density contour in yz-plane

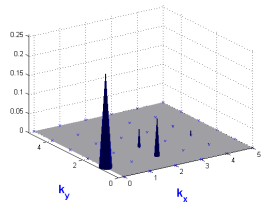

(f) Power spectrum in xy-plane

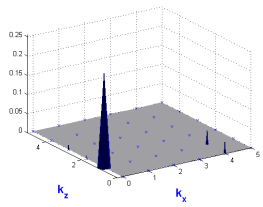

(g) Power spectrum in xz-plane

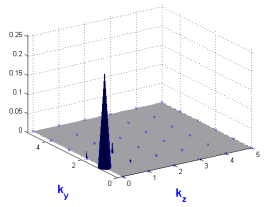

(h) Power spectrum in yz-plane

Figure 5.20: N=323433, L/W=3, W/d=50, H/d=150; Other parameters as in Fig. 5.1. The colour coding for the density field (particle volume fraction) is shown in respective colour-bar.

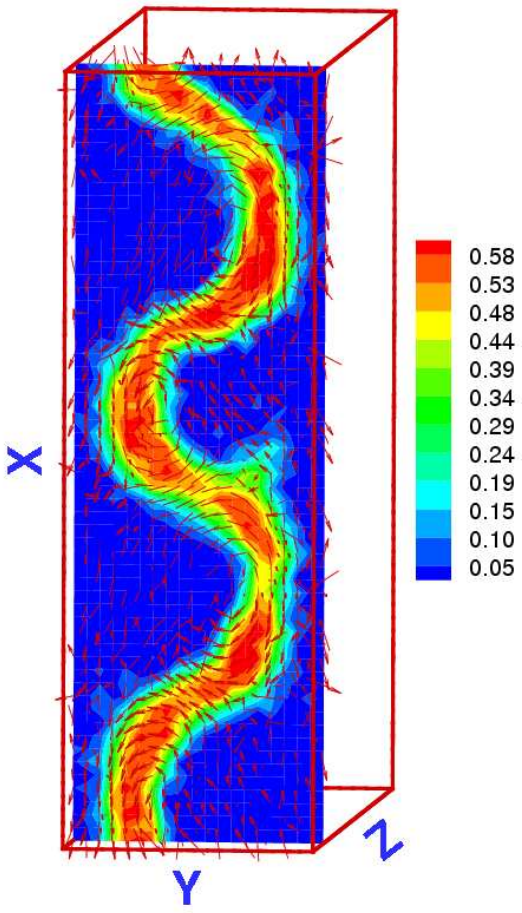

(a) Density contour slice (xy-plane)

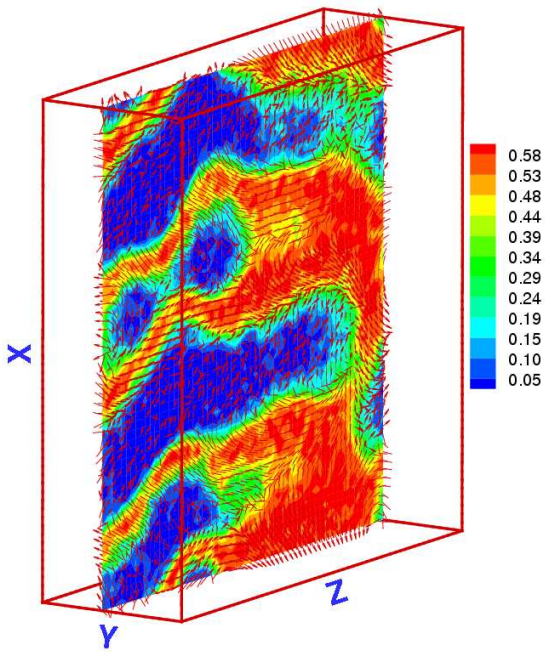

(b) Density contour slice (xz-plane)

Figure 5.21: Magnified view of density contour slices along with velocity vectors: (a) Fig. 5.20(c) (b) Fig. 5.20(d)

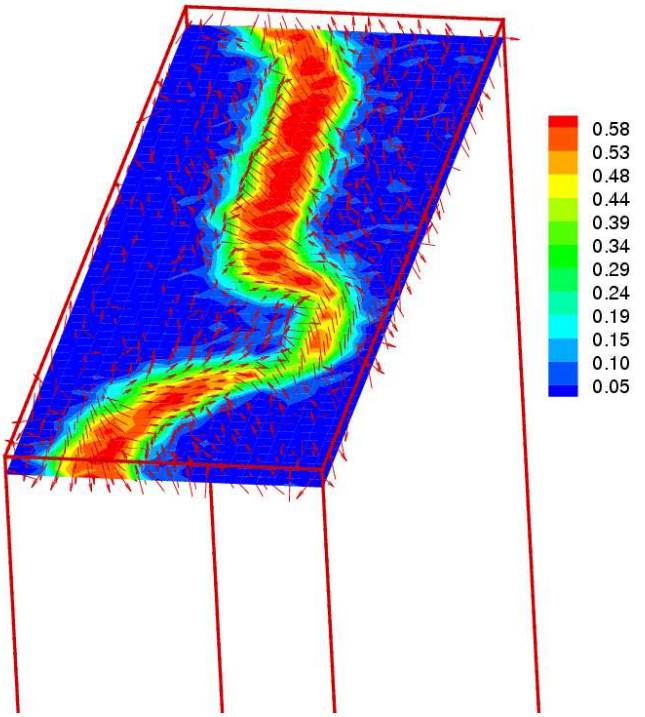

(a) Density contour top-slice (yz-plane)

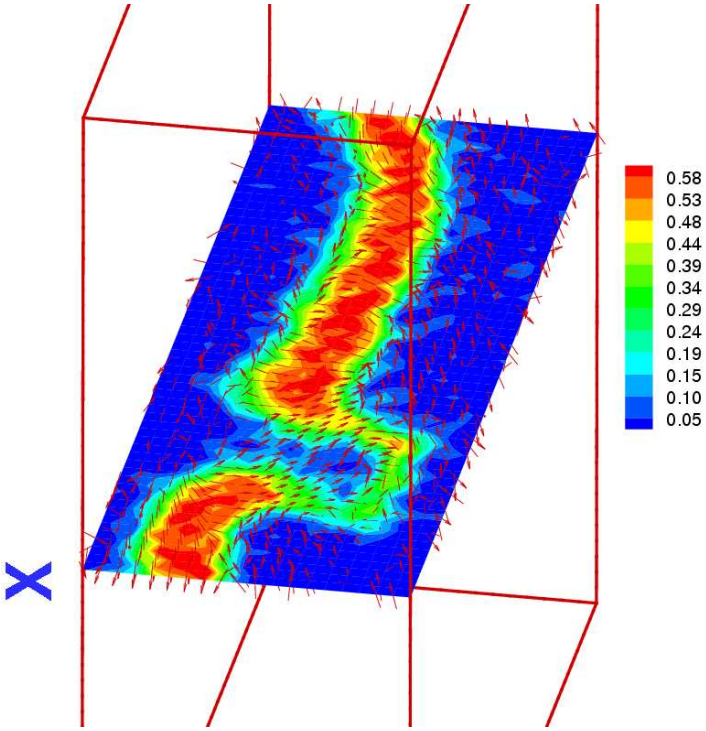

(b) Density contour middle-slice (yz-plane)

Figure 5.22: Magnified view of density contour slices along with velocity vectors for Fig. 5.20(e): (a) Top slice (b) Middle slice

5.2.3 Effect of the inelasticity

So far we have found that the density inhomogeneities are not only dependent on the system size and the aspect ratio but also on whether the system is two-dimensional or three-dimensional. This subsection deals with the effect of inelasticty on such inhomogeneities.

The system used here has N=107811 number of particles in a domain of $L/W = 3$, $W/d = 50$, $H/d = 50$. The analysis is started with e=0.7 which is the case for Fig. 5.13. The density variation in the form of a two-humped *wave* has already been discussed in the earlier subsection.

When we increase e=0.9, there is less dissipation in the system and hence at higher values of e the system has more kinetic energy. This is evident from the trace of average kinetic energy in Fig. 5.23(h) in comparison to Fig. 5.13(h). The density structures in Fig. 5.23 (a)-(d) suggest the presence of a *wavy-slug*. Other features look similar to those for its more dissipative counterpart ($e = 0.7$) in Fig. 5.13

Further decrease in dissipation, to e=0.99, results in a dense *slug* (with no waviness), Fig. 5.24(a). The average kinetic energy of the present system is higher than the system with e=0.9, as expected, Fig. 5.24(h). The various density contour slices and the power spectra peaks explain the observed density variations.

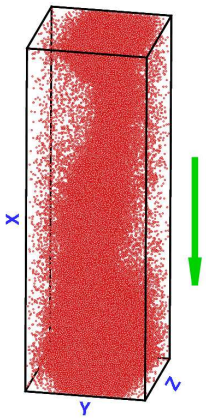

(a) Particle positions

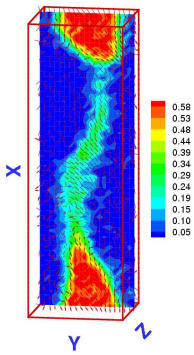

(b) Density contour in xy-plane

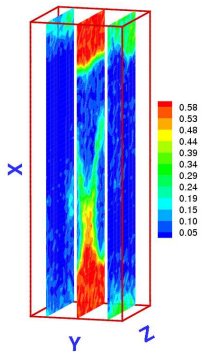

(c) Density contour in xz-plane

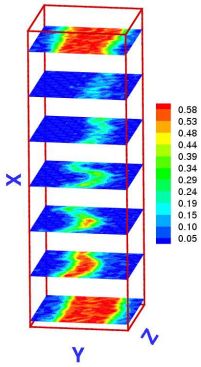

(d) Density contour in yz-plane

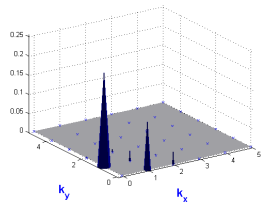

(e) Power spectrum in xy-plane

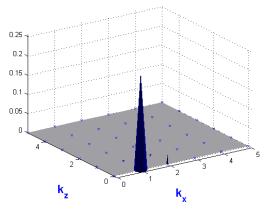

(f) Power spectrum in xz-plane

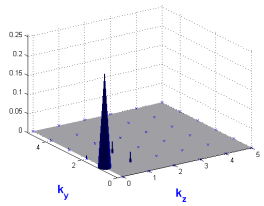

(g) Power spectrum in yz-plane

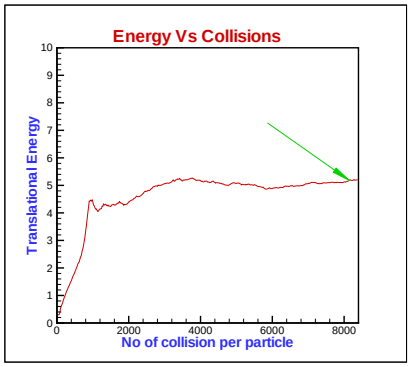

(h) Time trace of averge kinetic energy

Figure 5.23: Density structures at $e = 0.9$; Other parameters as in Fig. 5.13

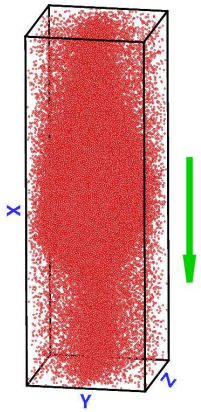

(a) Particle positions

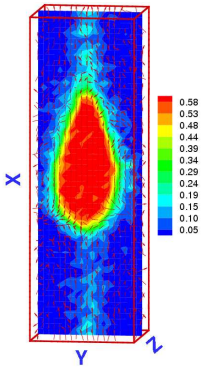

(b) Density contour in xy-plane

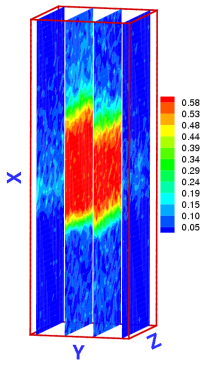

(c) Density contour in xz-plane

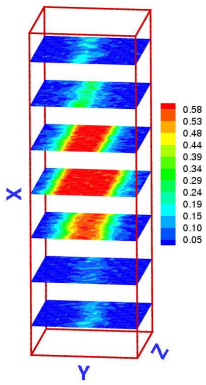

(d) Density contour in yz-plane

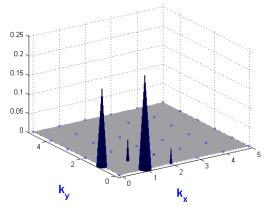

(e) Power spectrum in xy-plane

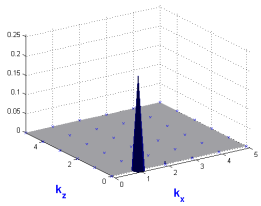

(f) Power spectrum in xz-plane

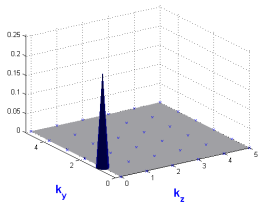

(g) Power spectrum in yz-plane

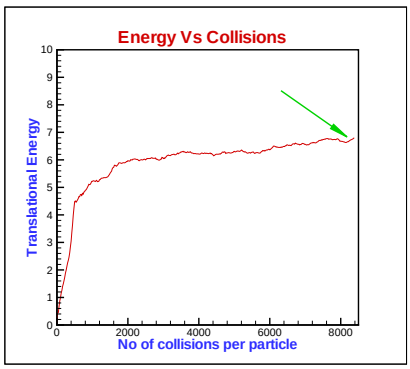

(h) Time trace of averge kinetic energy

Figure 5.24: Density structures at $e = 0.99$; Other parameters as in Fig. 5.13

5.3 Phase-Diagram of Density Waves

Fig. 5.25 shows the phase diagram of the steady state structures in the $(L/W, W/d)$ plane for the material and wall parameters as mentioned in section 5.2. Generally, at low values of W/d and L/W, for the volume fraction considered here, the system develops a *plug flow*. The system develops an *S-shaped wavy flow* at intermediate values of W/d. With further increase in W/d, there is formation of *slugs* and combination of these structures

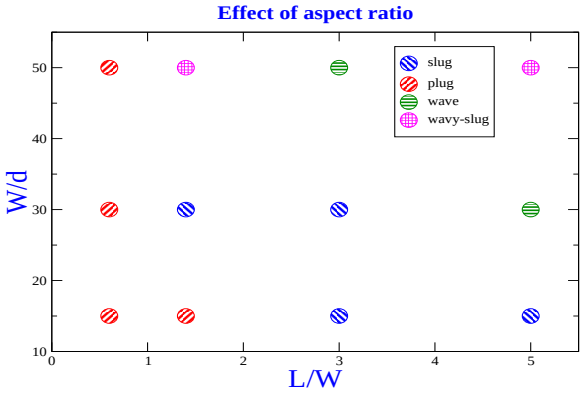

Figure 5.25: Phase diagram of steady state structures with ϕ=0.15, e=0.7, e_w=0.99, β=0.1, β_w=0.99 and W/H=1.

The effect of three dimensionality is summarised in Fig. 5.26. The availability of the third dimension influences the formation of the density variations and structures.

Fig. 5.27 summarises the effect of inelasticty on the formation of density inhomogeneities and structures in the form of a phase diagram. With the increase of e (i.e. decrease of dissipation), the steady wave structure no longer persists but results in the formation of slugs.

The velocity vectors superimposed on the density contours (Fig. 5.21 and Fig. 5.22) indicate that the particles in the dense regions move primarily in the vertical direction (the direction of gravity), while in the dilute regions the particles have significant radial motion. Hence most of the material transfer takes place in the high-density regions. The particle motion within the three-dimensional structures indicates the presence of vorticity, an important consideration for granular flows, which would enhance mixing.

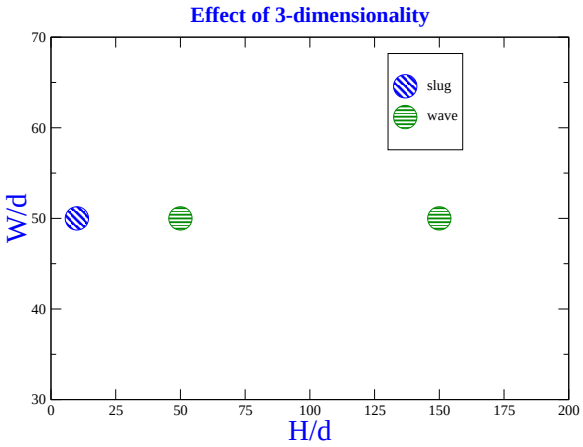

Figure 5.26: Phase diagram of steady state structures with N=107811, L/W=3 and W/d=50; Other parameters as in Fig. 5.25

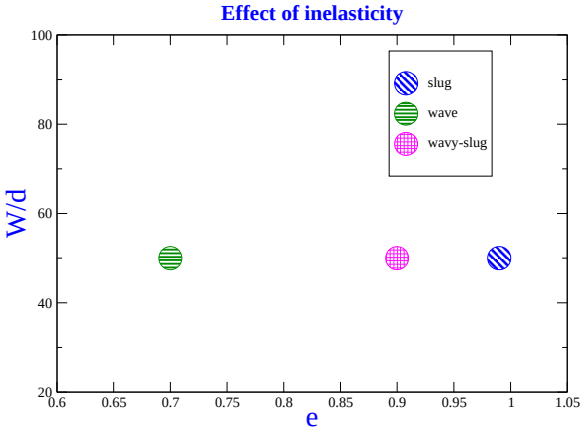

Figure 5.27: Phase diagram of steady state structures with N=107811, L/W=3, W/d=50, H/d=50; Other parameters as in Fig. 5.1

CHAPTER 6

SUMMARY AND OUTLOOK

In the present work, the gravity driven granular Poiseuille flow has been simulated in three dimensions between two infinite parallel plates. Various micro-structural features (velocity distribution functions, correlations, etc.) and macro-structural features (density waves, velocity, density and temperature profiles, etc.) have been probed in the rapid flow regime using an event-driven algorithm (Lubachevsky (1991)). A monodisperse system of "rough" inelastic hard spheres interacting via hard core potential has been used. The collisions are assumed to be binary and instantaneous in which only momentum is conserved but the energy is a non-conserved quantity. The normal coefficient of restitution (e) and the tangential coefficient of restitution (β) are the two basic governing parameters of the collision process. The collisions with walls are treated as the collisions with a particle of infinite mass.

In chapter 2, various aspects of the granular Poiseuille flow at a very low density ($\phi = 0.01$), also known as Boltzmann limit, has been probed. In the Boltzmann limit, the granular fluid behaves like a gas. It is found that when the dissipation in the system is less ($e \to 1$), the particles flow uniformly through the channel. However, as the dissipation is increased, the particles shift towards the centre of the channel and form a *plug*. The effect of dissipation on the mean field quantities was studied from the smooth limit ($\beta \to -1$) towards perfectly rough particles ($\beta \to 1$). By probing local velocity distribution functions (VDFs) for a range of dissipation and roughness, we conclude that the surface roughness of the particles plays an important role in the deviation of VDFs from the Gaussian distribution. In the Boltzmann limit, the density correlation was found to be negligible for any values of β and e. However, we found significant "directional" correlations between translational and rotational velocities for three limiting values of β ($\beta = -0.99$, $\beta = 0$ and $\beta = 0.99$) in the Boltzmann limit. The present work indicates that such orientational correlations should be incorporated in the theoretical models of granular flows.

In chapter 4, we probed the effects of density via the simulations of moderately

dense ($\phi = 0.1$) and dense ($\phi = 0.5$) granular flows. In the moderately dense flow, we observed dense *plugs* and density waves. As in the case of Boltzmann limit, the VDFs are found to be significantly affected by the particle roughness as well as by inelastic dissipation. Even in the elastic limit ($e \to 1$), the VDFs of all velocity components deviate considerably from Gaussian. The pair correlation function shows that the system has a liquid-like structure around the channel centerline where the particles are flowing in the form of density waves. By studying the orientational correlation function, we found that there are strong directional correlations over the whole channel width which increases with increasing dissipation. For any value of particle roughness, the spatial velocity correlations are found to be the largest for the streamwise velocity, and inelasticty enhances the magnitudes of velocity correlations.

Lastly, in chapter 5, the formation of density waves in the gravity driven flow of granular materials in a three-dimensional channel has been examined and different steady state forms of density variations have been observed. The nature of such density waves was analysed using a Fourier analysis of the coarse-grained density field. All results have been presented for a single density of $\phi = 0.15$. The effects of system size, three-dimensionality and inelasticity have been probed. It is found that the density variations and structure formations can be controlled by varying the system size. Once the system is large enough, a larger system does not alter the basic flow behaviour of the material considerably. The density-wave appears to persist in larger computational domains and increasing L/W or H/W simply permits additional wave numbers to be realized. Generally, at small values of W/d and L/W, for a particular volume fraction, the system develops a *plug flow*. The system develops an *S-shaped wavy flow* at intermediate values of W/d and further there is a formation of *slugs* and a combination of these structures. The effect of three dimensionality was also studied and it was found that the availability of the third dimension significantly influences the formation of the density waves. With increasing e (i.e. decrease of dissipation), the steady wave structure no longer persists but results in the formation of slugs. The velocity vectors superimposed on the density contours indicate that the particles in dense regions move primarily in the vertical direction (the direction of gravity), while in the dilute regions the particles have significantly more radial motion. Hence most of the material transfer takes place in the high-density regions. The particle motion in the observed

three-dimensional structures indicates the presence of vorticity, an important consideration for granular flows, which would enhance mixing.

A limited set of results on VDFs and correlations have been presented for dense flows ($\phi = 0.5$) at the end of chapter 4. However, our results differ from the experiments of Orpe & Kudrolli (2007) and Moka & Nott (2005). These differences could possibly be related to the fact that the bottom-plate in these experiments is "partially" open and hence there are dead-zones at the bottom of the experimental set-up which would lead to "back-flows". In future, we plan to exactly mimic the experimental set-up in our simulation. For dense flows, the collision model should be modified to include Coulomb friction that helps to distinguish between sliding and sticking contacts.

APPENDIX I

ADDITIONAL RESULTS ON VELOCITY DISTRIBUTION FUNCTIONS FOR $\phi = 0.5$

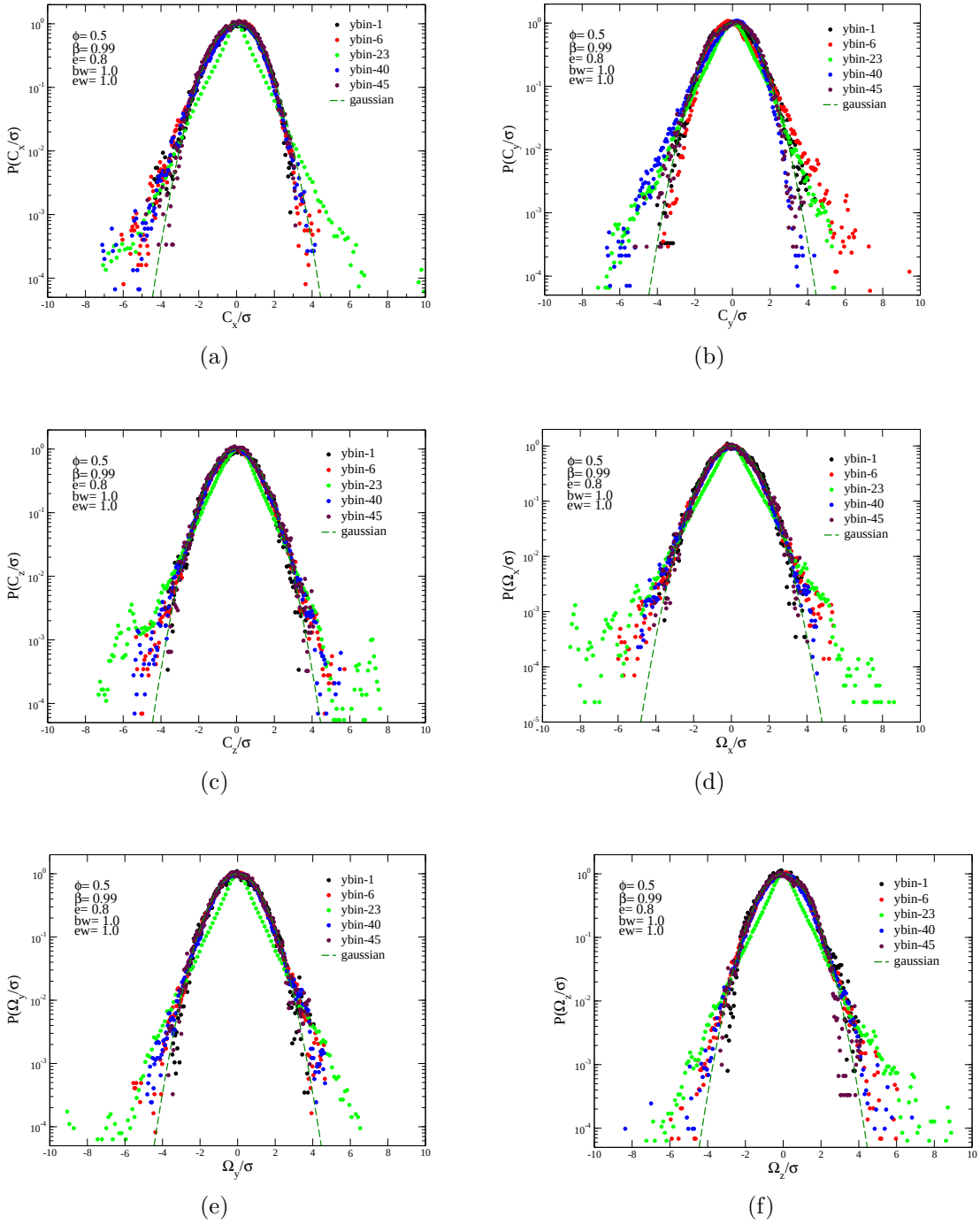

Figure I.1: $\beta = 0.99$ and $e = 0.8$: (a) C_x, (b) C_y, (c) C_z, (d) Ω_x, (e) Ω_y and (f) Ω_z.

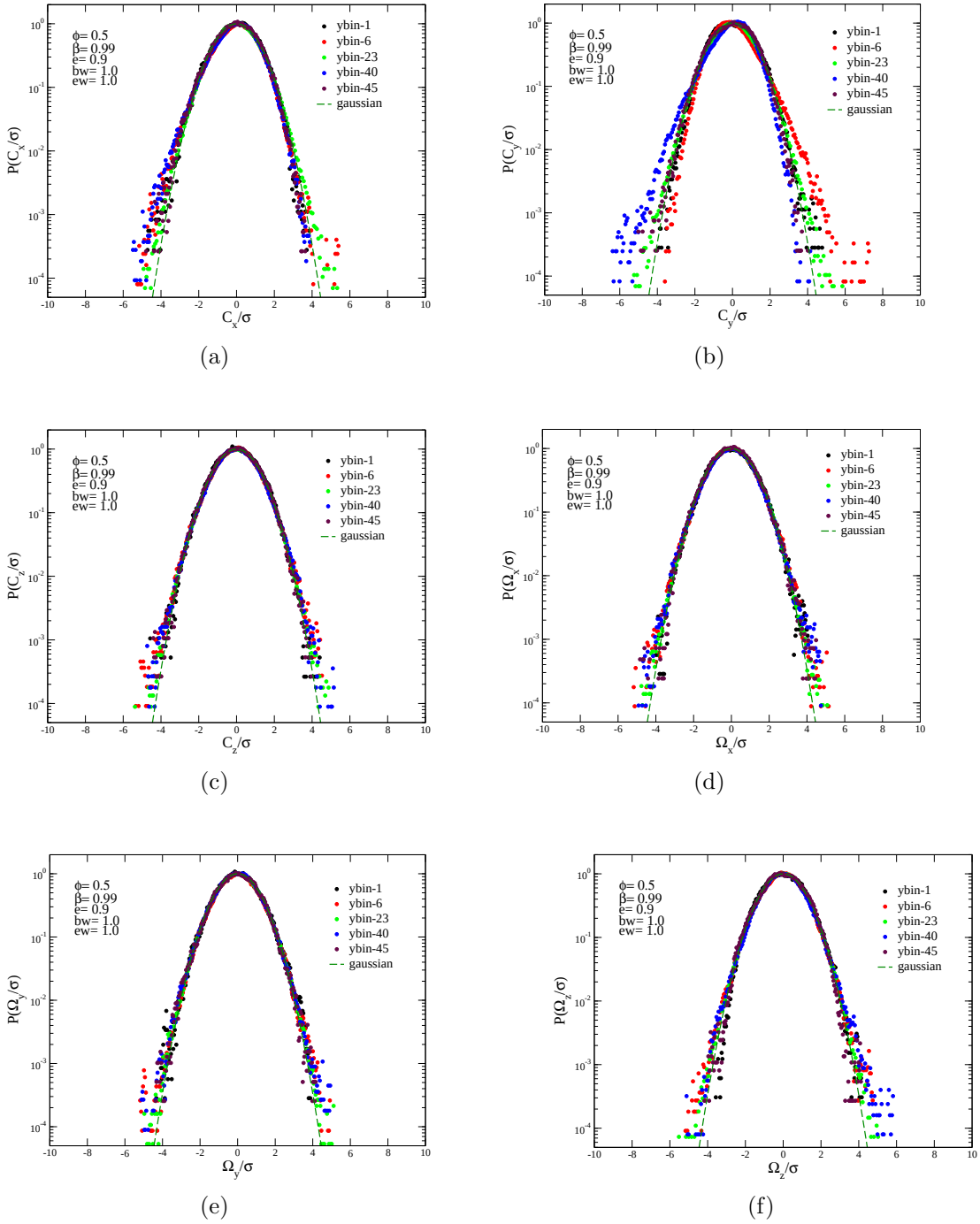

Figure I.2: $\beta = 0.99$ and $e = 0.9$: (a) C_x, (b) C_y, (c) C_z, (d) Ω_x, (e) Ω_y and (f) Ω_z.

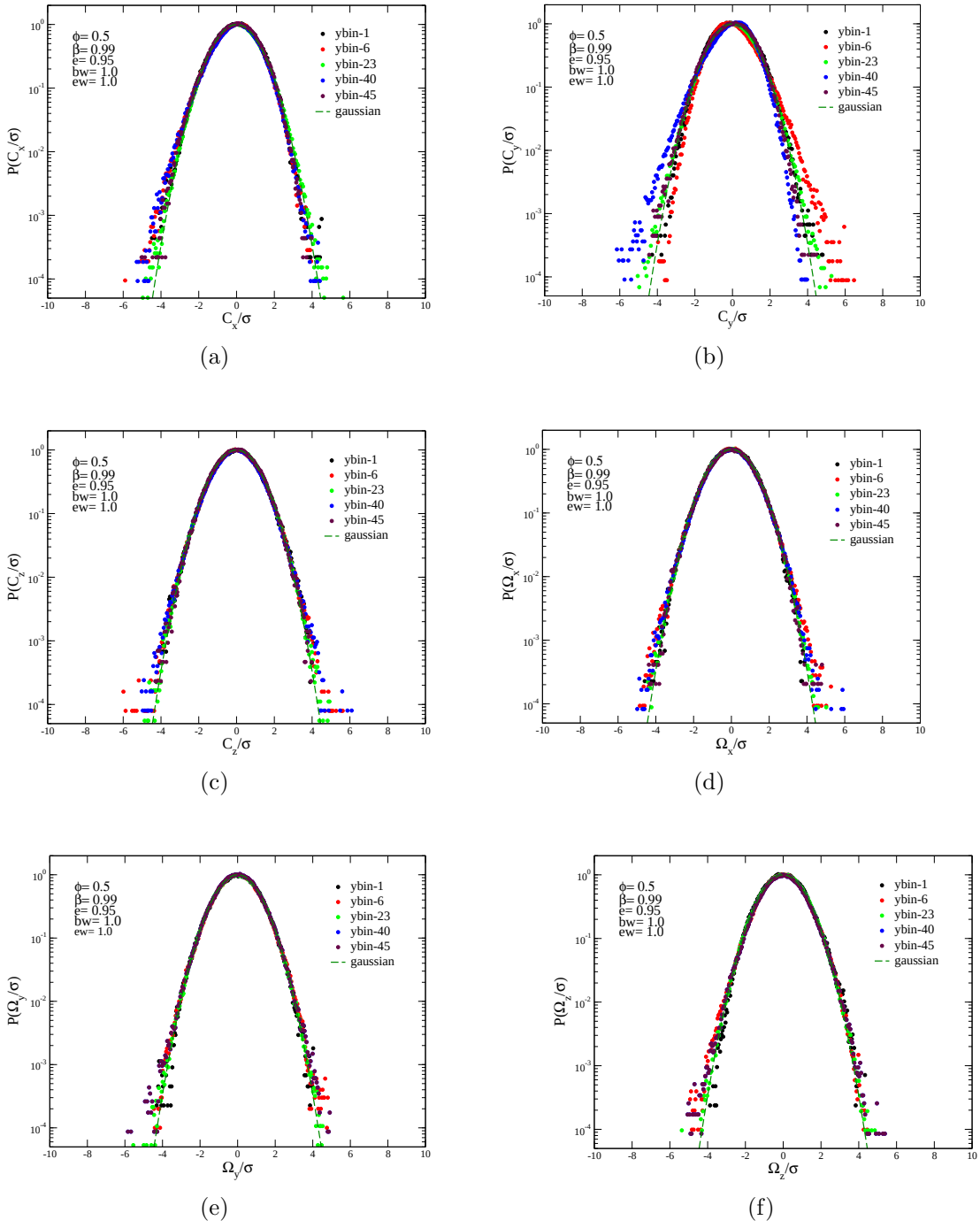

Figure I.3: $\beta = 0.99$ and $e = 0.95$: (a) C_x, (b) C_y, (c) C_z, (d) Ω_x, (e) Ω_y and (f) Ω_z.

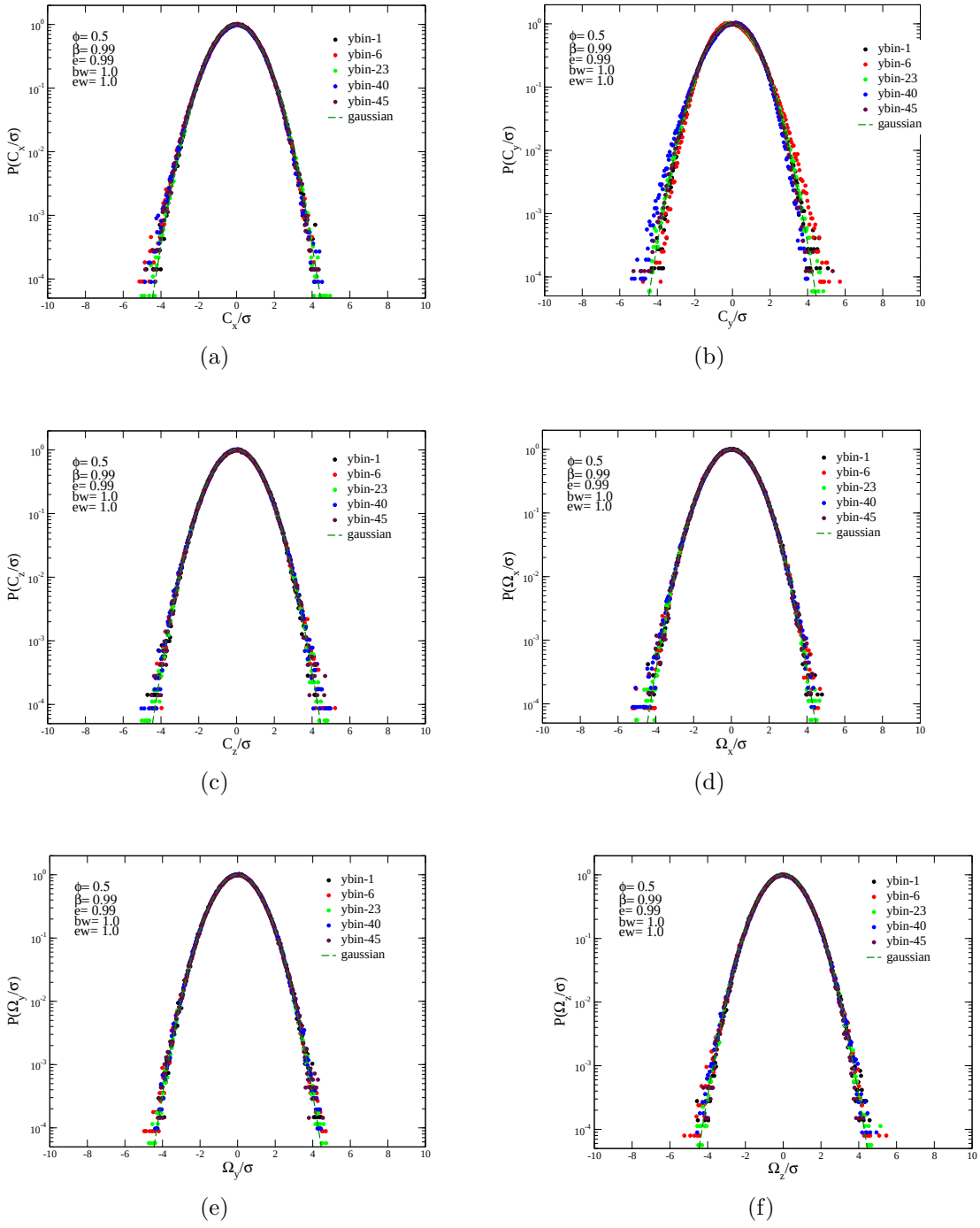

Figure I.4: $\beta = 0.99$ and $e = 0.99$: (a) C_x, (b) C_y, (c) C_z, (d) Ω_x, (e) Ω_y and (f) Ω_z.

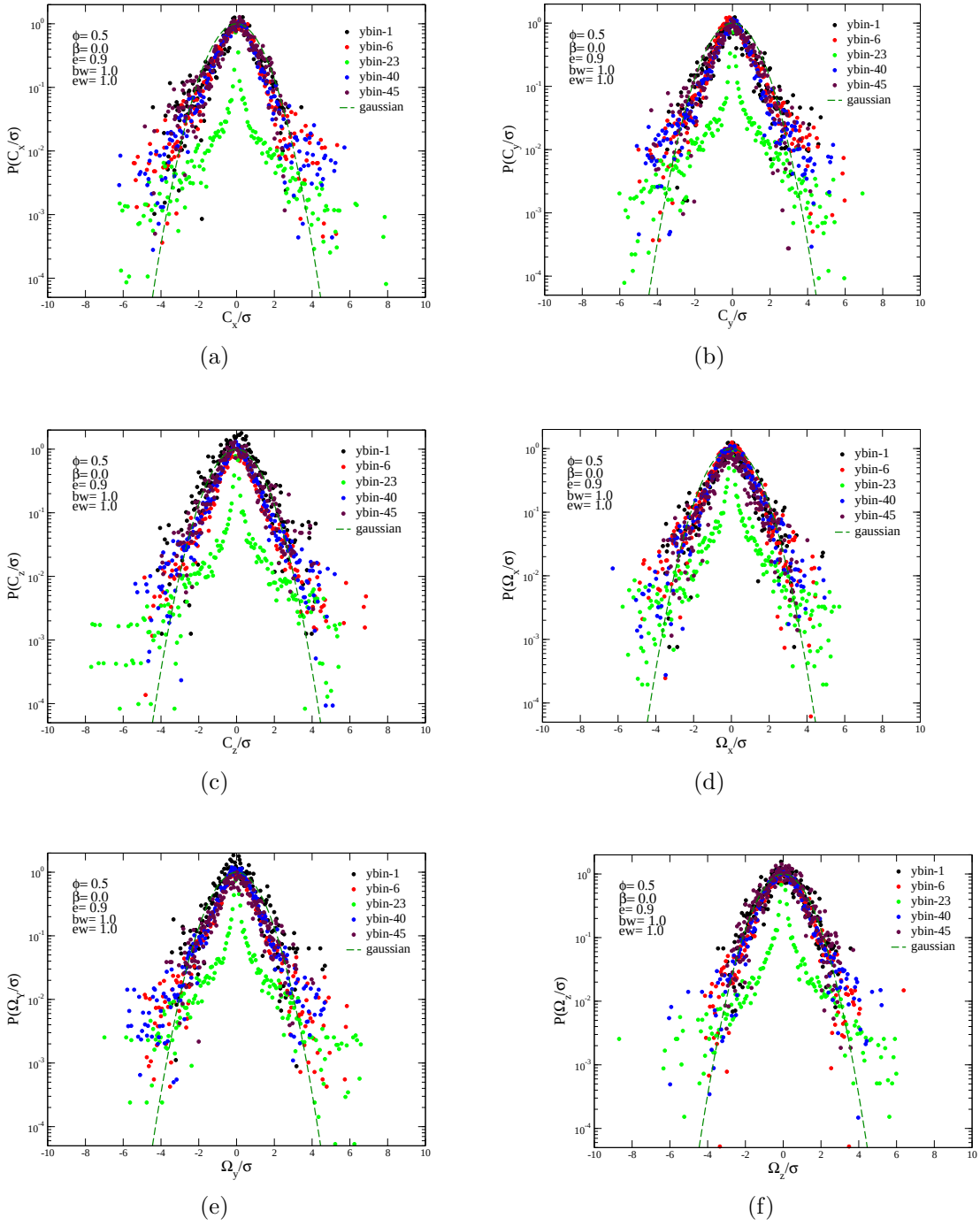

Figure I.5: $\beta = 0$ and $e = 0.9$: (a) C_x, (b) C_y, (c) C_z, (d) Ω_x, (e) Ω_y and (f) Ω_z.

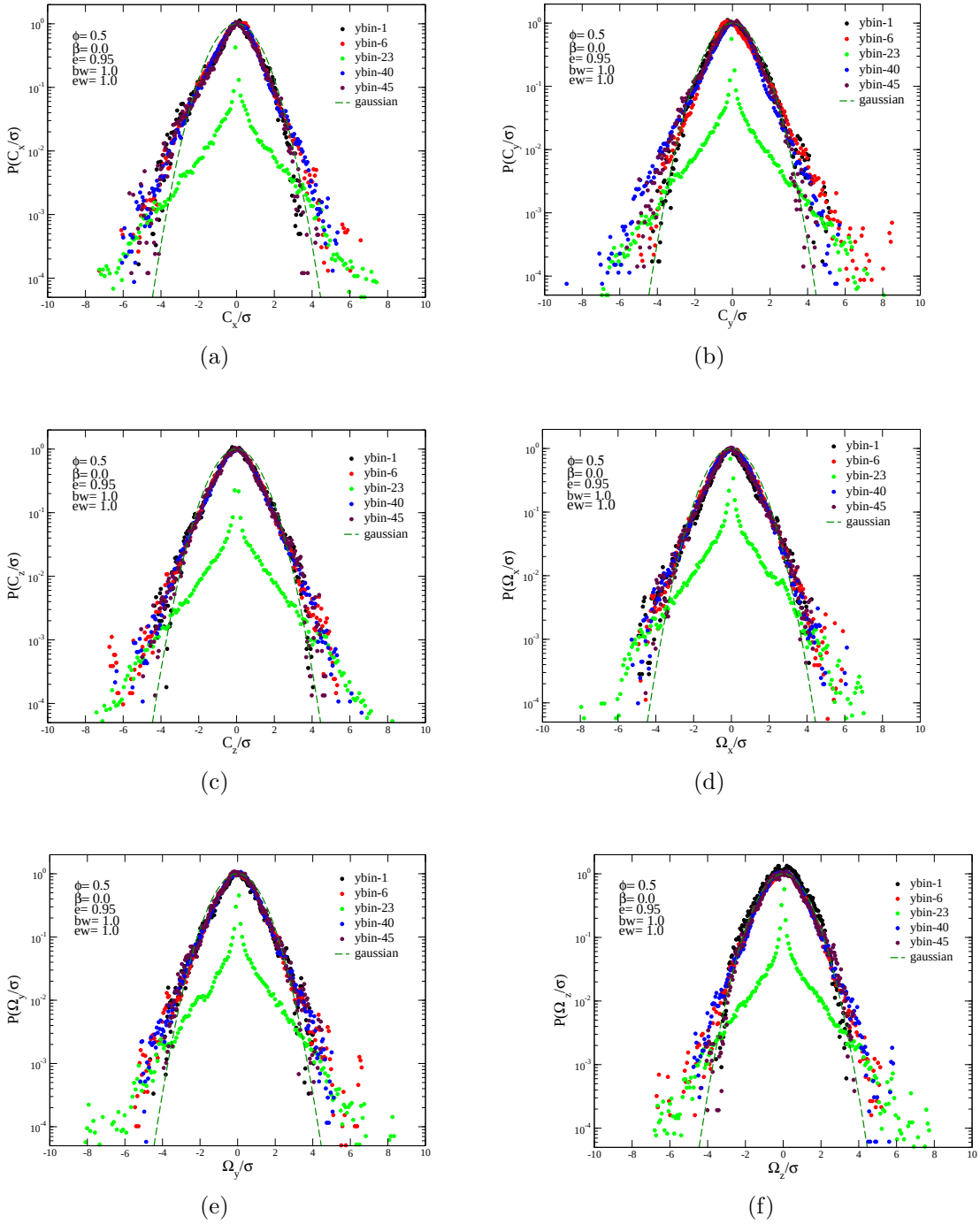

Figure I.6: $\beta = 0$ and $e = 0.95$: (a) C_x, (b) C_y, (c) C_z, (d) Ω_x, (e) Ω_y and (f) Ω_z.

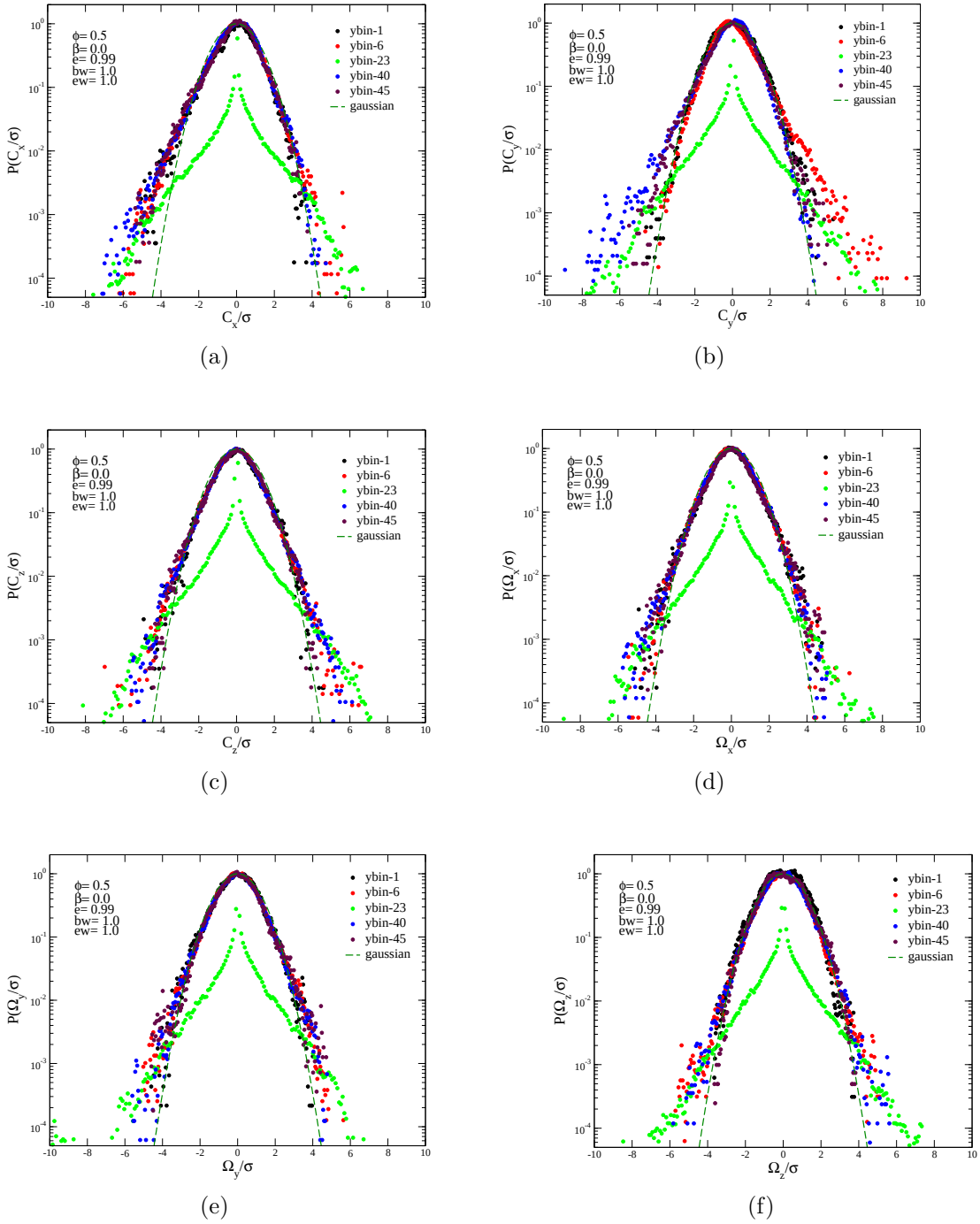

Figure I.7: $\beta = 0$ and $e = 0.99$: (a) C_x, (b) C_y, (c) C_z, (d) Ω_x, (e) Ω_y and (f) Ω_z.

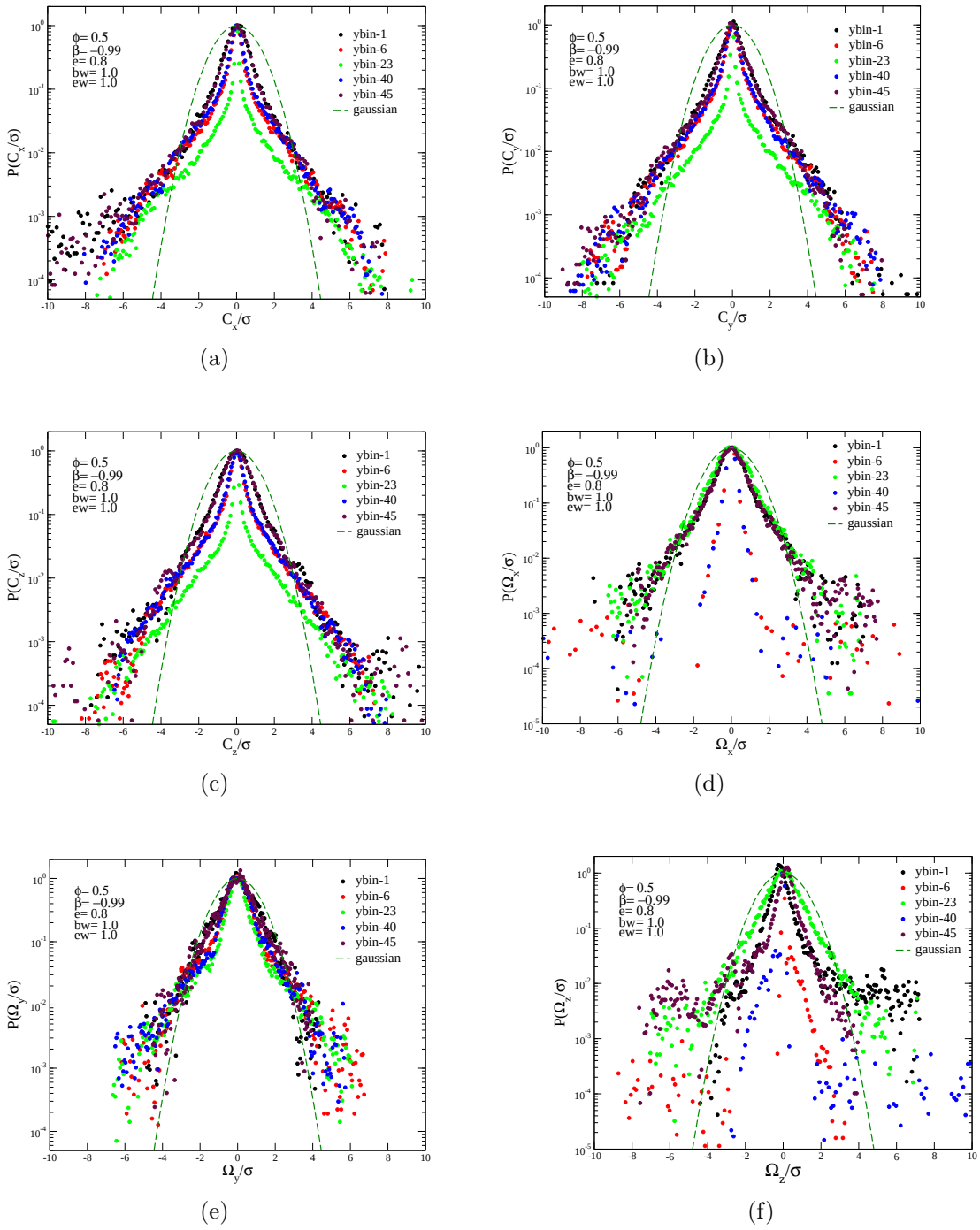

Figure I.8: $\beta = -0.99$ and $e = 0.8$: (a) C_x, (b) C_y, (c) C_z, (d) Ω_x, (e) Ω_y and (f) Ω_z.

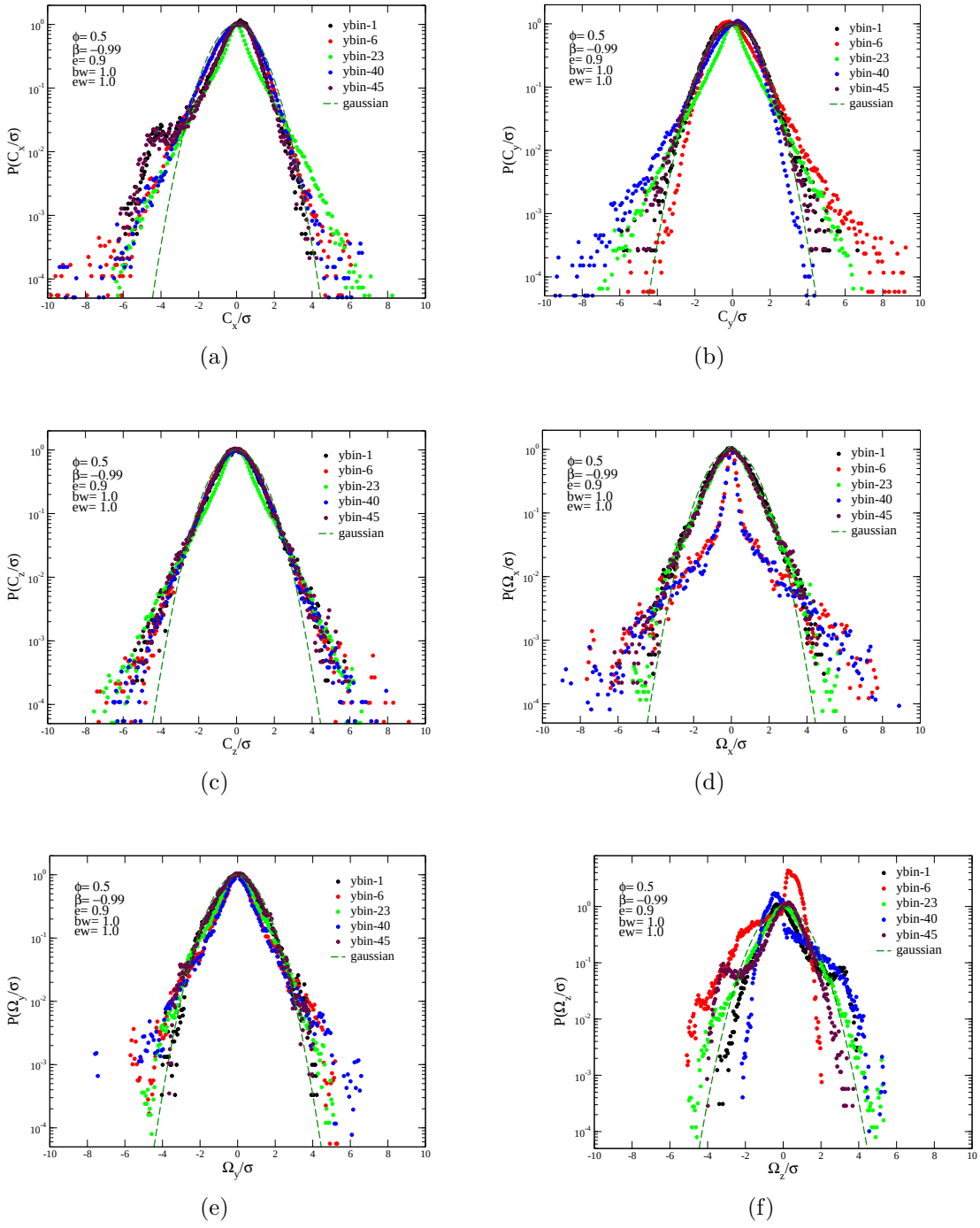

Figure I.9: $\beta = -0.99$ and $e = 0.9$: (a) C_x, (b) C_y, (c) C_z, (d) Ω_x, (e) Ω_y and (f) Ω_z.

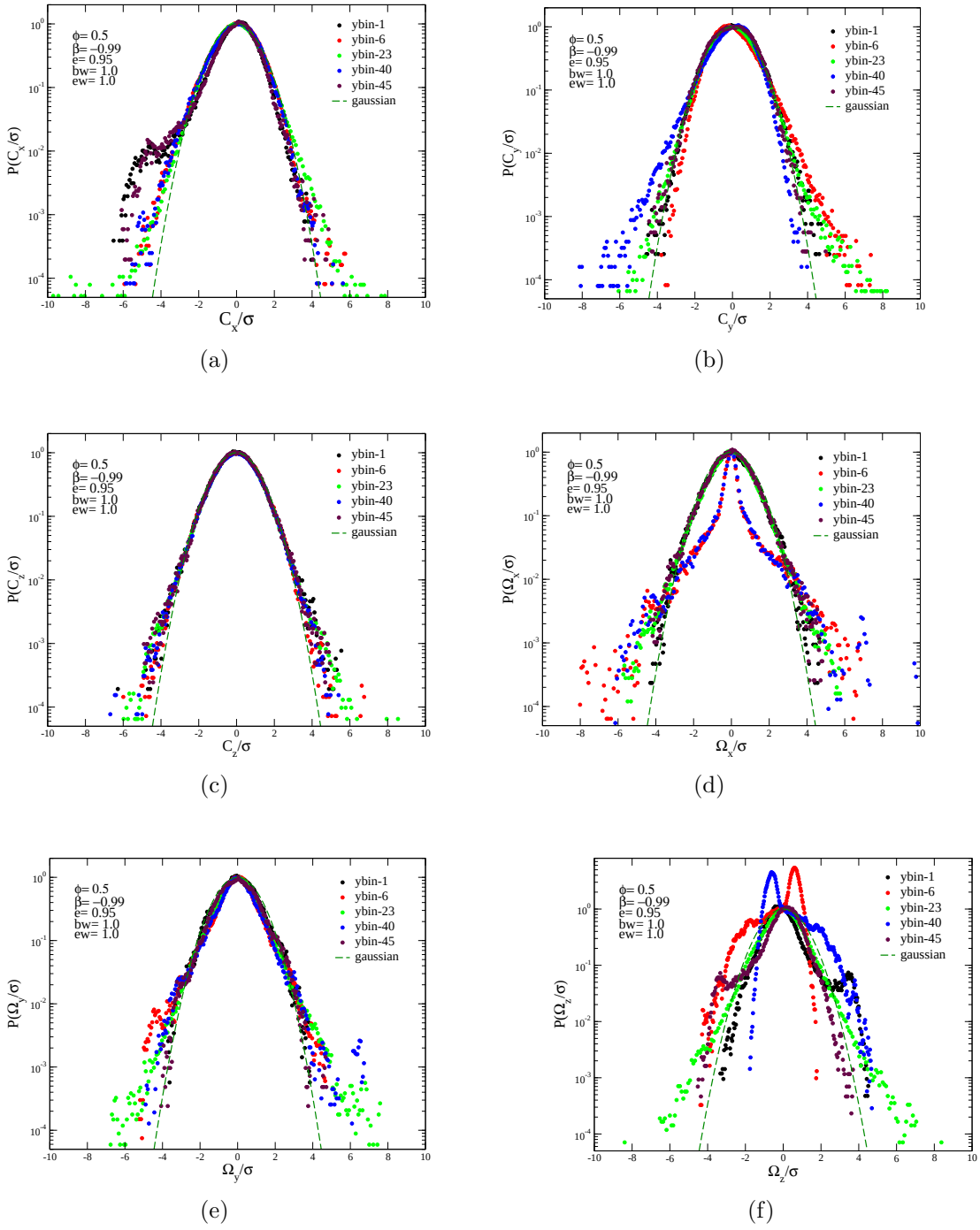

Figure I.10: $\beta = -0.99$ and $e = 0.95$: (a) C_x, (b) C_y, (c) C_z, (d) Ω_x, (e) Ω_y and (f) Ω_z.

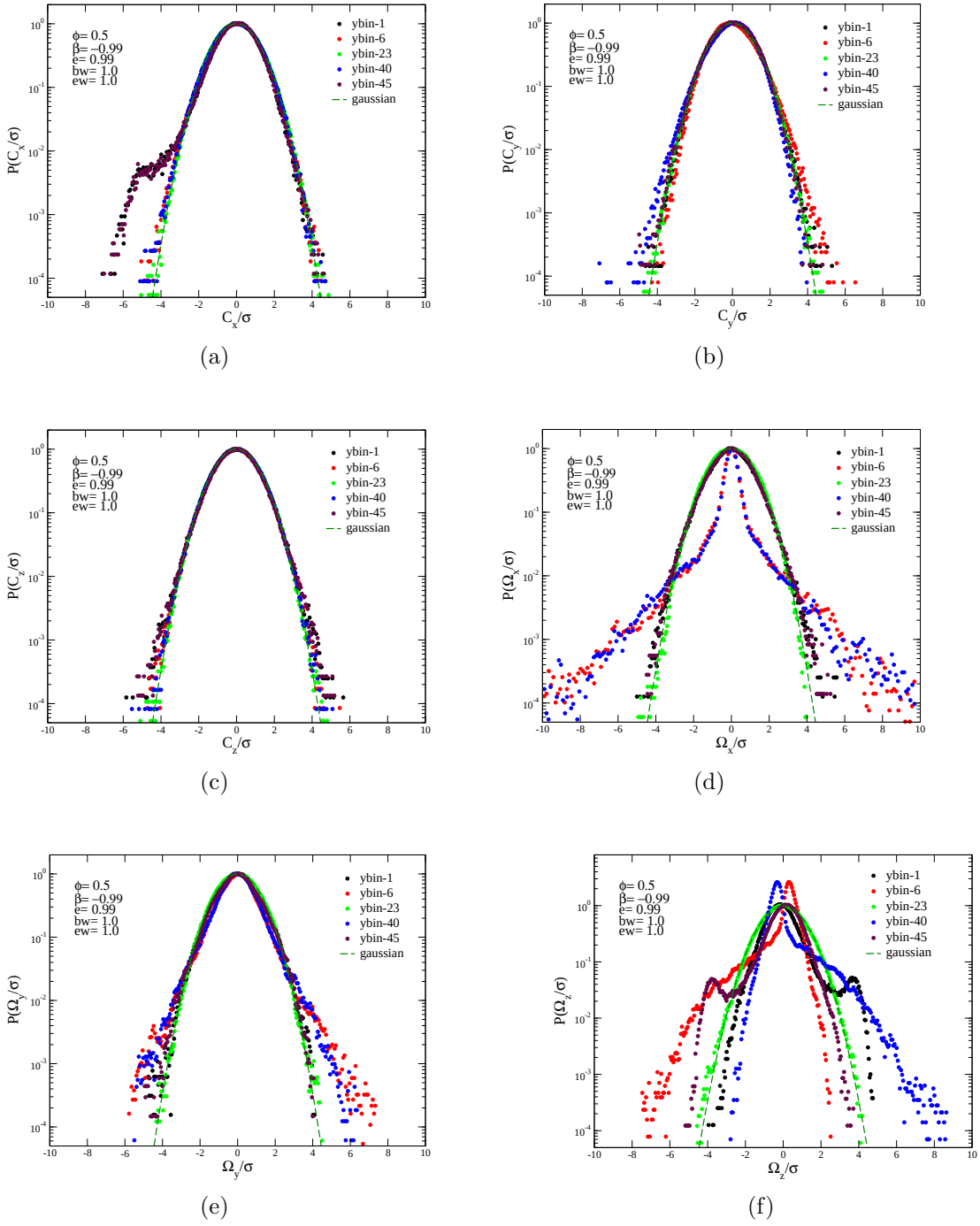

Figure I.11: $\beta = 0$ and $e = 0.99$: (a) C_x, (b) C_y, (c) C_z, (d) Ω_x, (e) Ω_y and (f) Ω_z.

References

Alam, M. & Luding, S. 2003 First normal stress difference and crystallization in a dense sheared granular fluid. *Phys of Fluids* **15**, 22982312.

Alam, M. & Nott, P. R. 1998 Stability of plane couette flow of a granular material. *J. Fluid Mech* **377**, 99–136.

Alam, M., Shukla, P. & Luding, S. 2008 Universality of shear-banding instability and crystallization in sheared granular fluid. *J. Fluid Mech* **In Press.**

Alam, M., Trujillo, L. & Herrmann, H. J. 2006 Hydrodynamic theory for reverse brazil nut segregation and the non-monotonic ascension dynamics. *Journal of Statistical Physics.* **124**, 587–623.

Allen, M. P. & Tildesley, D. J. 1987 *Computer Simulation of Liquids*. Oxford: Oxford University Press.

Bagnold, R. A. 1954 Experiments on a gravity-free dispersion of large solid spheres in a Newtonian fluid under shear. *Proc. Royal Soc. London* **225**, 49–63.

Baran, O., Ertas, D., , Halsey, T. C., Grest, G. S. & Lechman, J. B. 2006 Velocity correlations in dense gravity-driven granular chute flow. *Phys. Rev. E* **74**, 051302.

Brilliantov, N., Pöschel, T., Kranz, W. & Zippelius, A. 2007 Translations and rotations are correlated in granular gases. *Phy. Rev. Letter* **98**, 128001.

Campbell, C. S. 1990 Rapid granular flow. *Ann. Rev. Fluid Mechanics* **22**, 57.

Chen, J. 1996 Clusters. In *Progress in fluidized and fluid particle systems* (ed. D. King). American Institute of Chemical Engineers, New York.

Choi, J., Kudrolli, A., Rosales, R. R. & Bazant, M. Z. 2004 Diffusion and mixing in gravity-driven dense granular flows. *Phys. Rev. Lett.* **92**, 174301.

Denniston, C. & Li, H. 1999 Dynamics and stress in gravity-driven granular flow. *Phys. Rev. E* **59**, 3289.

Eringen, A. C. 1964 Simple microfluidics. *Int. J. Engng. Sci.* **2**, 205–217.

Ferguson, A. & Chakraborty, B. 2006 Stress and large-scale spatial structures in dense, driven granular flows. *Phys. Rev. E* **73**, 011303.

Gayen, B. 2007 Velocity fluctuation, correlation and rheology in frictional granular shear flow. *MS Engg. Thesis, JNCASR, Bangalore* .

Gayen, B. & Alam, M. 2006 Algebraic and exponential instabilities in a sheared micropolar granular fluid. *J. Fluid Mech.* **567**, 195–233.

Gayen, B. & Alam, M. 2008 Orientational correlation and velocity distributions in a sheared rough dilute granular gas. *Phys. Rev. Lett* **100**, 068002.

Goldhirsch, I. 2003 Rapid granular flows. *Annu. Rev. Fluid Mech.* **35**, 267.

Goldhirsch, I., Noskowicz, S. H. & Bar-Lev, O. 2005 Nearly smooth granular gases. *Phys. Rev. Lett* **95**, 068002.

Haff, P. K. 1983 Grain flow as a fluid-mechanical phenomenon. *J. Fluid Mech.* **134**, 401–430.

Herrmann, H. J., Hovi, J. P. & Luding, S. 1998 Physics of dry granular media. *Kluwer* .

Jackson, R. 2000 *The Dynamics of Fluidized Particles*. Cambridge: Cambridge University Press.

Jaeger, H. M., Nagel, S. R. & Behringer, R. 1996 Granular solids, liquids and gases. *Rev. Mod. Phys.* **68**, 1259.

Jenkins, J. T. & Richman, M. W. 1985 Kinetic theory for plane flows of a dense gas of identical, rough, inelastic disks. *Phys Fluids* **28**, 3485.

Kadanoff, L. 1999 Built upon sand: theoretical ideas inspired by granular flows. *Rev. Mod. Phys* **71**, 435.

Lee, J. & Leibig, M. 1994 Density waves in granular flow: A kinetic wave approach. *J. Physics* **4**, 507.

Liss, E. D., Conway, S. L. & Glasser, B. J. 2002 Density waves in gravity-driven granular flow through a channel. *Phys. Fluids* **14** (9), 3309–3326.

Lubachevsky, B. D. 1991 How to simulate billards and similar systems. *J. Comp. Phys.* **94** (2), 255.

Luding, S., Huthmann, M., McNamara & Zippelius, A. 1998 Homogeneous cooing of rough dissipative particles: theory and simulations. *Phys. Rev. E* **58**, 3416.

Lun, C. K. K. 1991 Kinetic theory for granular flow of dense, slightly inelastic, slightly rough spheres. *J. Fluid Mech.* **233**, 539–559.

Lun, C. K. K. & Savage, S. B. 1987 A simple kinetic theory for granular flow of rough, inelastic, spherical particles. *J. Appl. Mech.* **54**, 47.

Mitarai, N., Hayakawa, H. & Nakanishi, H. 2002 Collisional granular flow as a micropolar fluid. *Phys. Rev. lett.* **88**, 174301.

Mohan, L. S., Rao, K. K. & Nott, P. R. 2002 A frictional cosserat model for the slow shearing of granular materials. *J. Fluid Mech.* **457**, 377–409.

Moka, S. & Nott, P. R. 2005 Statistics of particle velocities in dense granular flows. *Phys. Rev. Lett.* **95**, 068003.

Natarajan, V. V. R., Hunt, M. L. & Taylor, E. D. 1995 Local measurements of velocity fluctuations and diffusion coefficients for a granular material flow. *J. Fluid Mech.* **304**, 1–25.

Orpe, A. V. & Kudrolli, A. 2007 Velocity correlations in dense granular flows observed with internal imaging. *Phys. Rev. Lett.* **98**, 238001.

Ottino, J. M. & Khakhar, D. V. 2000 Mixing and segregation of granular materials. *Annu. Rev. Fluid Mech.* **32**, 55–91.

Peng, G. & Herrmann, H. J. 1994 Density waves of granular flow in a pipe using lattice-gas automata. *Phys. Rev. E* **49** (3), 1796.

Poschel, T. 1994 Recurrent clogging and density waves in granular material flowing through a narrow pipe. *J. Physics* **4**, 499.

Raafat, T., Hulin, J. P. & Herrmann, H. J. 1996 Density waves in dry granular media falling through a vertical pipe. *Phys. Rev. E* **53**, 4345–4355.

Rapaport, D. C. 1995 *The Art of Molecular Dynamics Simulation*. Cambridge: Cambridge University Press.

Reithmuller, T., Shimansky, L., Rosenkranz, D. & .Poschel, T. 1997 Langevian equation approach to a granular flow in a narrow pipe. *J. Stat. Phys.* **86**, 421.

Savage, S. B. 1982 Granular flows down rough inclines - review and extension. In *Proc. US-Japan seminar on New Models and Constitutive Relations in Mechanics of Granular Materials* (ed. J. T. Jenkins & M. Satake). Elsevier.

Tsai, J. C., Losert, W., Voth, G. A. & Gollub, J. P. 2001 Two-dimensional granular poiseuille flow on an incline: Multiple dynamical regimes. *Phys. Rev. E* **65**, 011306.

Vijaykumar, K. C. 2007 Particle dynamics simulation of gravity driven granular poiseuille flow. *MS Engg. Thesis, JNCASR, Bangalore* .

Wang, C.-H., Jackson, R. & Sundaresan, S. 1997 Instabilities of fully developed rapid flow of a granular material in a channel. *J. Fluid Mech.* **342**, 179.